BIOMASS-DERIVED ACTIVATED CARBON THROUGH SELF-ACTIVATION PROCESS

Changlei Xia, B.S., M.S.

Dissertation Prepared for the Degree of

DOCTOR OF PHILOSOPHY

UNIVERSITY OF NORTH TEXAS

May 2016

APPROVED:

Sheldon Q. Shi, Major Professor
Nandika A. D'Souza, Committee Member
Zhenhai Xia, Committee Member
Oliver M.R. Chyan, Committee Member
Seifollah Nasrazadani, Committee Member
Tae-Youl Choi, Committee Member
Yong X. Tao, Chair of the Department of Mechanical and Energy Engineering
Costas Tsatsoulis, Dean of the College of Engineering
Costas Tsatsoulis, Dean of the Toulouse Graduate School

Xia, Changlei. *Biomass-Derived Activated Carbon through Self-Activation Process*. Doctor of Philosophy (Mechanical and Energy Engineering), May 2016, 128 pp., 15 tables, 45 figures, chapter references, 103 titles.

Self-activation is a process that takes advantage of the gases emitted from the pyrolysis process of biomass to activate the converted carbon. The pyrolytic gases from the biomass contain CO_2 and H_2O, which can be used as activating agents. As two common methods, both of physical activation using CO_2 and chemical activation using $ZnCl_2$ introduce additional gas (CO_2) or chemical ($ZnCl_2$), in which the CO_2 emission from the activation process or the zinc compound removal by acid from the follow-up process will cause environmental concerns. In comparison with these conventional activation processes, the self-activation process could avoid the cost of activating agents and is more environmentally friendly, since the exhaust gases (CO and H_2) can be used as fuel or feedstock for the further synthesis in methanol production. In this research, many types of biomass were successfully converted into activated carbon through the self-activation process. An activation model was developed to describe the changes of specific surface area and pore volume during the activation. The relationships between the activating temperature, dwelling time, yield, specific surface area, and specific pore volume were detailed investigated. The highest specific surface area and pore volume of the biomass-derived activated carbon through the self-activation process were up to 2738 $m^2\ g^{-1}$ and 2.209 $cm^3\ g^{-1}$, respectively. Moreover, the applications of the activated carbons from the self-activation process have been studied, including lithium-ion battery (LIB) manufacturing, water cleaning, oil absorption, and electromagnetic interference (EMI) shielding.

ACKNOWLEDGEMENTS

I'd like to thank my graduate research advisor, Dr. Sheldon Q. Shi, for his mentorship. It has been my honor to be his student. My special thanks to Drs. Liping Cai and Shifeng Zhang for helping me on the research. My gratitude to my PhD committee members, Drs. Nandika A. D'Souza, Zhenhai Xia, Oliver M.R. Chyan, Seifollah Nasrazadani and Tae-Youl Choi, and department chair Dr. Yong X. Tao.

Many thanks to our collaborators, including Drs. Jianzhang Li and his students (Youming Dong, Kaili Wang, La Wang, and Yutao Yan), Wonbong Choi and his group members (Dr. Chiwon Kang, and Mumukshu Patel), Hualiang Zhang and his student (Han Ren), Xu Nie and his student (Ying Qiu), and Jiangtao Cheng.

I'd like to acknowledge the members in Drs. Shi and D'Souza's lab, including Drs. Kaiwen Liang, Jie Lu, Haitao Cheng, Zhenzhong Gao, Baoliang Liu, Desheng Liu, Cheng Liu, Mickey C. Richardson and Mangesh Nar, Andres Garcia, Hussain S. Rizvi, Nathaniel Warner, Jinglei Wu, Zhiguang Ding, Wen Che, Jonathan Huang, Kathleen Chen, Hwa-Shen Tan, Yu Fu, Lee Smith, Kayode Oluwabunmi, Zachary Hoyt, Shunli Zhao, Bing Yang, Amaal Al-Shenawa, et al. Also thanks to other friends who helped me, including Drs. Richard F. Reidy, Guido F. Verbeck, Jianbing Niu, Quan Xu, Anchal Sondhi, Xiaohua Li and Reinaldo Santos-Ortiz, Zhenghang Zhao, Hao Yu, Jae-Young Jeong, Oseoghaghare Okobiah, Md Salah Uddin, Chuangwei Liu, Michael Mendoza, Jonova Thomas, Daniel Lin, Wei Sun, Lu Deng, Phillip M. Mach, Angela Nelson, et al.

Finally, I would like to thank my family, especially my wife Yingji Wu, for their support and encouragement.

TABLE OF CONTENTS

Page

LIST OF TABLES

Page

LIST OF FIGURES

Page

CHAPTER 1

INTRODUCTION

1.1 Activated Carbon

Activated carbon is defined as a crude form of graphite with a random or amorphous structure, which is highly porous with large internal surface area and exhibits a broad range of pore sizes from visible cracks, crevices and slits of molecular dimensions (Hamerlinck et al., 1994; Mohan and Pittman Jr, 2006). Generally, the activated carbon has a surface area of over 500 m^2 g^{-1}, which is usually determined by the gas adsorption testing. In the absorption analysis, non-polar gases, e.g. N_2, CO_2, Ar, CH_4, etc., are used, where the N_2 adsorption at 77 K is commonly utilized (Mohan and Pittman Jr, 2006).

1.1.1 History

In accordance with historical reports, the starting of carbon utilization can be dated back to ancient times. The Egyptians and Sumerians are deemed to first use of carbon in the form of wood chars (charcoal) in 3750 BC (Inglezakis and Poulopoulos, 2006). However, the use of activated carbon in its current form has only a short history. Activated carbon was firstly produced on an industrial scale was in the early twentieth century. . In the early stage of development of the activated carbon in Europe, it was only available in the form of powdered activated carbon. Recently, numerous types of activated carbon, e.g. granular activated carbon, pelletized activated carbon, etc., have been developed. In 1900–1901, activated carbon was firstly used in the sugar refining

process to replace bone char (Bansal et al., 1988). Only powder activated carbon was produced using wood as a raw material in the early 20th century. With the development of technology, the traditional powder activated carbon has been converted into different types, such as granular activated carbon and pelletized activated carbon, for easily recycling and waste minimization. Currently, a wide range of feed-stocks are being used for activated carbons manufacturing, including coconut shells, wood char, sugar, lignin, lignite, bone char, petroleum coke, peat, peach pits, fertilizer waste, sawdust, carbon black, rice hulls, fish, waste rubber tire, etc. (Mohan and Pittman Jr, 2006).

1.1.2 Classification

There are abundant of complex products made from activated carbon. Also the classification of activated carbon is complex. In general, the activated carbon can be classified on the basis of particle size, preparation method, and industrial application, surface characteristics, behavior, and other fundamental criteria, e.g. powdered activated carbon (PAC), granular activated carbon (GAC), bead activated carbon (BAC), extruded activated carbon (EAC), impregnated carbon, polymer coated carbon, etc. (Wikipedia, 2016). Among them, the classification made based on their size is widely accepted and standardized, e.g. PAC, and GAC.

1.1.2.1 Powdered Activated Carbon

As a kind of powdered material, PAC is made up of crushed or ground activated carbon particles. PAC is not common to be used in a dedicated vessel because of the high head loss. Thus, PAC is directly added to other target raw materials, e.g. rapid mix

basins, raw water intakes, gravity filters, and clarifiers (Durkee, 2014). The PAC size is standardized in the American National Standards Institute/American Water Works Association (ANSI/AWWA) B600-10 standard. Table 1.1 shows the particle-size requirement of PAC based on the ANSI/AWWA B600-10 standard. In general, the particle-size distribution of PAC was: not less than 99% of the activated carbon shall pass a No. 100 sieve, not less than 95% shall pass a No. 200 sieve, and not less than 90% shall pass a No. 325 sieve.

Table 1.1 Particle-size requirement of PAC.

Particle size		Minimum pass
US standard sieve number	Sieve opening (μm)	
100	149	≥99%
200	74	≥95%
325	44	≥90%

1.1.2.2 Granular Activated Carbon

Compared to powdered activated carbon, GAC has a relatively larger particle size, which is suitable for absorption of gases and vapors because of its rapid diffusion. Generally, GAC is used for water treatment, deodorization and separation of components of flow system (Wikipedia, 2016). The sharps of GAC are divided into two types, i.e. granular form and extruded form. GAC with different size is classified by the ANSI/AWWA B604-12 standard. Table 1.2 shows the sizes of GAC identified in the ANSI/AWWA B604-12 standard, in which the maximum and minimum sizes of GAC are 6 and 50 mesh, respectively. GAC is designated by two sizes as listed in Table 1.2. For instant, 8 × 20 means that the GAC particle sizes are between 8 to 20 mesh. However,

oversize of 8 mesh and undersize of 30 mesh are allowed but limited to a specific percentage (generally specified as 85 – 95% retained). The most popular GACs are sized as 12 × 40 and 8×30, because these GACs have a good balance of surface area, size, and head loss characteristics (Wikipedia, 2016).

Table 1.2 US standard sieves and opening sizes for GAC from ANSI/AWWA B604 standard.

US standard sieve number	Sieve opening (mm)
6	3.360
8	2.380
10	2.000
12	1.700
14	1.400
16	1.180
18	1.000
20	0.850
25	0.710
30	0.600
35	0.500
40	0.425
45	0.355
50	0.300

1.1.3 Market

In the report of Mozammel et al. (2002), the sales of activated carbon in the world market were estimated as 375,000 tons in 1990, excluding sales in Eastern Europe and China. If Eastern Europe and China are considered, the total sale can be over 450,000 tons. By late 1990s, the world market was estimated at about 700,000 tons/year, with a market growth of about 4 – 6% per year. In a recent report “World Activated Carbon to

2016” (The Freedonia Group, 2012), the activated carbon demand from worldwide is expected to increase more than ten percent per year to 1.9 million metric tons through 2016. Definitely, the large market demand will contribute to the high gross sales. The global activated carbon market was detected to be $1.8 billion in 2011, and is estimated to reach $3.0 billion by 2016.

1.2 Manufacture

A large number of raw materials can be used for producing activated carbon. Some raw materials are carbon based, e.g. lignite, coal, etc. Others may need to go through a carbonization process for being converted into carbon. These carbons are further activated into activated carbon. The activation methods can be divided into two categories, i.e. physical/thermal activation, and chemical activation. Physical/thermal activation employs a mild oxidizing gas, e.g. CO_2, water steam, etc., to eliminate the bulk of the volatile matters, followed by partial gasification, the porosity and more surface area of the materials are developed (Mohan and Pittman Jr, 2006). Chemical activation methods employs chemicals to develop the surface area. These common chemicals used for the activation process are acid, strong base, or salt (Mohan and Pittman Jr, 2006).

1.3 Applications

Due to the high specific surface area and porosity, activated carbon is widely used in various fields, e.g. water purification, gas purification, sewage treatment, decaffeination, gold purification, metal extraction, air filters in gas masks and

respirators, medicine, filters in compressed air, electromagnetic interferences absorption, energy storage, and many other applications (Wikipedia, 2016). These applications are sorted and summarized in Figure 1.1. Among them, water cleaning, Li-ion battery, and electromagnetic interferences shielding of the activated carbon were investigated in this work.

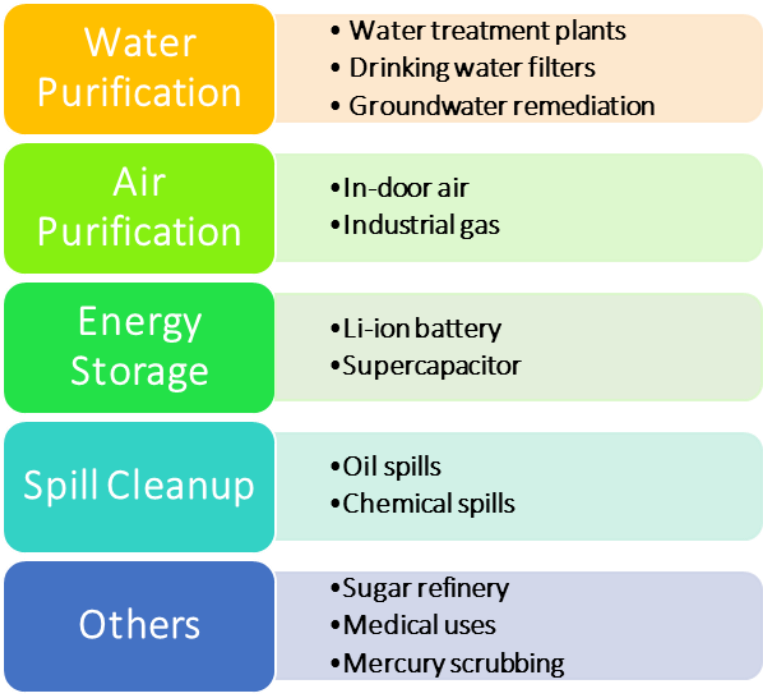

Figure 1.1 Applications of activated carbon.

1.4 Dissertation Overview

As a natural resource, biomass has advantages of renewable, sustainable, low density, low cost, environmentally-friendly, etc. During my PhD's studies, several biomass-derived products have been investigated, including biomass-based activated carbons and their applications (Shi and Xia, 2014; Xia and Shi, 2016a; Xia and Shi, 2015; Xia and Shi, 2016b), natural fiber-reinforced polymer-matrix composites (Xia et

al., 2014; Xia et al., 2015a; Xia et al., 2015b; Xia et al., 2015c; Xia et al., 2016a; Xia et al., 2016b; Xia et al., 2016d; Xia et al., 2016e; Xia et al., 2016f), soy protein-based films (Xia et al., 2015d; Xia et al., 2016c; Zhang et al., 2016), wood modification (Dong et al., 2016a; Dong et al., 2016b; Yan et al., 2015), and others (Kang et al., 2015; Richardson et al., 2015; Shi et al., 2015). In this dissertation, the biomass-based activated carbons and their applications are presented.

The objective of this research is to develop a novel, green self-activation process for high-performance activated carbon using biomass as a raw material. Chapters 2 – 5 are divided into two sections, i.e. Section I (1.4.1): theories and experiments of self-activation, and Section II (1.4.2): applications of the activated carbon from self-activation. In Section I, the self-activation of kenaf core and kenaf fiber were studied and the theory of self-activation process was investigated. In Section II, the applications of activated carbon, including Li-ion battery, water cleaning, and electromagnetic interferences shielding, were studied.

1.4.1 Theories and Experiments of Self-Activation

Self-activation is a process that takes advantage of the gases emitted from the pyrolysis process of biomass to activate the converted carbon, which saves the cost of activating agents and decreases the environmental impact compared with conventional activation processes. An activation model was developed to describe the mechanism of the activation process, and it was examined by the self-activation experiments using kenaf core as a raw material. The relationships among the parameters, yields, specific surface areas, and specific pore volumes were quantified. The results showed that the

ideal temperatures for the self-activation process of kenaf core were between 970 – 1,090°C. The yield of 9.0% for the activated carbon from kenaf core provided a highest surface area per gram of biomass, while the yields of 5.5 – 13.8% could achieve 90% of the highest. The developed activation model can be used to explain the relationship between the yields, specific surface areas, and specific pore volumes, effectively.

Moreover, kenaf fiber was another raw material chose for the study of self-activation. The Brunauer–Emmett–Teller (BET) specific surface area (SA_{BET}) of non-activation and self-activation pyrolyzed at 1100°C for 2 hours were analyzed and obtained as 252 m^2/g and 1,280 m^2/g, respectively, with 408% difference. The results showed that the highest SA_{BET} (1,742 m^2/g) was achieved when the kenaf fiber was pyrolyzed at 1,100°C for 10 hours. A linear relationship was shown between the $\ln(SA_{BET})$ and the yield of kenaf fiber based on the activated carbon through the self-activation process. The study also showed that the produced activated carbon with a 9.0% yield gave the highest surface area per gram kenaf fiber (80 m^2 per gram kenaf fiber), and those with the yields between 7.2 – 13.8% produced 95% of the highest surface area per gram kenaf fiber (76 m^2 per gram kenaf fiber).

1.4.2 Applications of Activated Carbon

The application of activated carbon used as lithium-ion battery anode was investigated. The activated carbon was manufactured through self-activation process from pine wood. The as-obtained activated carbon possesses specific surface area of 2738 $m^2\ g^{-1}$ and specific pore volume of 2.209 $cm^3\ g^{-1}$, which are superior to other reports and offers favorable electrochemical properties. The activated carbon-based

anode for Li-ion battery shows a reversible specific capacity of 384 mAh g^{-1} at 1C, which is close to the theoretical specific capacity of graphite. The finding suggests that the self-activation process is a green, scalable, and efficient process, and has great potential in developing next-generation high-performance electrode materials for electrochemical energy storages.

Water purification of the activated carbon from self-activation process was evaluated. The properties of kenaf core-based activated carbons from self-activation of kenaf core were compared with commercial activated carbon. Specific surface area, specific pore volumes of micropore and meso-macropore of the activated carbons were analyzed. The results of iodine number, tannin value, copper (II) absorption, and rhodamine 6G showed that the absorption capacity of the absorbents are highly related to their pore structures. In another word, the micropore of the carbon prefers to absorb small-molecular impurities, e.g. iodine and copper (II), and the meso-macropore is good at big-molecular absorption, e.g. tannic acid and rhodamine 6G. Moreover, the oil-absorption capacity was also improved, i.e. 1 g kenaf core-based activated carbon can keep 22.4 g oil, which was about 4.6 times higher than the untreated kenaf core.

Activated carbon owns electromagnetic interference (EMI) shielding application. In our study, kenaf fiber/polyester composites incorporated with powdered activated carbon (PAC) were prepared using the vacuum-assisted resin transfer molding (VARTM) process. The product demonstrates the electromagnetic interference (EMI) shielding functions. The kenaf fibers were retted in a pressured reactor to remove the lignin and extractives in the fibers. The PAC was loaded into the freshly retted fibers in water. The PAC loading effectiveness was determined using the Brunauer-Emmett-

Teller (BET) specific surface area analysis. A higher BET value was obtained with a higher PAC loading. The transmission energies of the composites were measured by exposing the samples to the irradiation of electromagnetic waves with a variable frequency from 8 GHz to 12 GHz. As the PAC content increased from 0% to 10.0%, 20.5% and 28.9%, the EMI shielding effectiveness increased from 41.4% to 76.0%, 87.9% and 93.0%, respectively. Additionally, the EMI absorption increased from 21.2% to 31.7%, 44.7% and 64.0%, respectively. The ratio of EMI absorption/shielding of the composite at 28.9% of PAC loading were increased significantly by 37.1% as compared with the control sample. It was indicated that the incorporation of PAC into the composites was very effective for absorbing electromagnetic waves, resulting in a decrease in secondary electromagnetic pollution.

1.5 References

Bansal, R.C., Donnet, J., Stoeckli, F., 1988. Active Carbon. M. Dekker, New York and Basel.

Dong, Y., Yan, Y., Ma, H., Zhang, S., Li, J., Xia, C., Shi, S.Q., Cai, L., 2016a. In-situ chemosynthesis of ZnO nanoparticles to endow wood with antibacterial and UV-resistance properties, *Journal of Materials Science & Technology*, Accepted Manuscript, In Press, Doi: 10.1016/j.jmst.2016.03.018.

Dong, Y., Yan, Y., Wang, K., Li, J., Zhang, S., Xia, C., Shi, S.Q., Cai, L., 2016b. Improvement of water resistance, dimensional stability, and mechanical properties of poplar wood by rosin impregnation, *European Journal of Wood and Wood Products*, 74(2), 177-184.

Durkee, J.B., 2014. Cleaning with Solvents: Methods and Machinery, 1st ed. Elsevier Science & Technology.

Hamerlinck, Y., Mertens, D., Vansant, E., 1994. Activated Carbon Principles in Separation Technology. Elsevier, New York.

Inglezakis, V., Poulopoulos, S., 2006. Adsorption, Ion Exchange and Catalysis: Design of Operations and Environmental Applications. Elsevier, New York.

Kang, C., Patel, M., Rangasamy, B., Jung, K., Xia, C., Shi, S., Choi, W., 2015. Three-dimensional carbon nanotubes for high capacity lithium-ion batteries, *Journal of Power Sources*, 299, 465-471.

Mohan, D., Pittman Jr, C.U., 2006. Activated carbons and low cost adsorbents for remediation of tri-and hexavalent chromium from water, Journal of Hazardous *Materials*, 137(2), 762-811.

Mozammel, H.M., Masahiro, O., Sc, B., 2002. Activated charcoal from coconut shell using $ZnCl_2$ activation, *Biomass and Bioenergy*, 22(5), 397-400.

Richardson, M.C., D'Souza, N.A., Xia, C., Shi, S., Mach, P.M., Verbeck, G.F., 2015. Metal ion and benzene remediation of simulated hydraulic fracturing "Fracking" waste water using natural materials, *Hydraulic Fracturing Journal*, 2(4), 82-86.

Shi, S.Q., Che, W., Liang, K., Xia, C., Zhang, D., 2015. Phase transitions of carbon-encapsulated iron oxide nanoparticles during the carbonization of cellulose at various pyrolysis temperatures, *Journal of Analytical and Applied Pyrolysis*, 115, 1-6.

Shi, S.Q., Xia, C., 2014. Porositization process of carbon or carbonaceous materials, US patent 14/211,357.

The Freedonia Group, 2012. World Activated Carbon to 2016, http://www.freedoniagroup.com/brochure/28xx/2878smwe.pdf, Accessed on 3/8/2106.

Wikipedia, 2016. Activated Carbon, https://en.wikipedia.org/wiki/Activated_carbon, Accessed on 3/8/2016.

Xia, C., Shi, S.Q., Cai, L., 2014. Vacuum assisted resin transfer molding process for kenaf fiber based composites, *Proceedings of the 57th International Convention of Society of Wood Science and Technology (SWST)*, 2014, 459-465.

Xia, C., Shi, S.Q., 2015. Self-activation process for biomass based activated carbon, *Proceedings of 58th International Convention of Society of Wood Science and Technology (SWST)*, 2015, 98-104.

Xia, C., Shi, S.Q., Cai, L., Hua, J., 2015a. Property enhancement of kenaf fiber composites by means of vacuum-assisted resin transfer molding (VARTM), *Holzforschung*, 69(3), 307-312.

Xia, C., Shi, S.Q., Cai, L., Nasrazadani, S., 2015b. Increasing inorganic nanoparticle impregnation efficiency by external pressure for natural fibers, *Industrial Crops and Products*, 69, 395-399.

Xia, C., Shi, S.Q., Cai, L., 2015c. Vacuum-assisted resin infusion (VARI) and hot pressing for $CaCO_3$ nanoparticle treated kenaf fiber reinforced composites, *Composites Part B: Engineering*, 78, 138-143.

Xia, C., Wang, L., Dong, Y., Zhang, S., Shi, S.Q., Cai, L., Li, J., 2015d. Soy protein isolate-based films cross-linked by epoxidized soybean oil, *RSC Advances*, 5(101), 82765-82771.

Xia, C., Shi, S.Q., 2016a. Self-activation for activated carbon from biomass: theory and parameters, *Green Chemistry*, Accepted Manuscript, In Press, doi: 10.1039/C5GC02152A.

Xia, C., Ren, H., Shi, S.Q., Zhang, H., Cheng, J., Cai, L., Chen, K., Tan, H., 2016a. Natural fiber composites with EMI shielding function fabricated using VARTM and Cu film magnetron sputtering, *Applied Surface Science*, 362, 335-340.

Xia, C., Shi, S.Q., 2016b. Self-activation process to fabricate activated carbon from kenaf, *Wood and Fiber Science*, 48, 62-69.

Xia, C., Zhang, S., Ren, H., Shi, S.Q., Zhang, H., Cai, L., Li, J., 2016b. Scalable fabrication of natural-fiber reinforced composites with electromagnetic interference shielding properties by incorporating powdered activated carbon, *Materials*, 9(1), 10.

Xia, C., Zhang, S., Shi, S.Q., Cai, L., Garcia, A.C., Rizvi, H.R., D'Souza, N.A., 2016c. Property enhancement of soy protein isolate-based films by introducing POSS, *International Journal of Biological Macromolecules*, 82, 168-173.

Xia, C., Zhang, S., Shi, S.Q., Cai, L., Huang, J., 2016d. Property enhancement of kenaf fiber reinforced composites by in situ aluminum hydroxide impregnation, *Industrial Crops and Products*, 79, 131-136.

Xia, C., Shi, S.Q., Wu, Y., Cai, L., 2016e. High pressure-assisted magnesium carbonate impregnated natural fiber-reinforced composites, *Industrial Crops and Products*, 86, 16-22.

Xia, C., Wang, K., Dong, Y., Zhang, S., Shi, S.Q., Cai, L., Ren, H., Zhang, H., Li, J., 2016f. Dual-functional natural-fiber reinforced composites by incorporating magnetite, *Composites Part B: Engineering*, Accepted Manuscript, In Press, doi: 10.1016/j.compositesb.2016.03.016.

Yan, Y., Dong, Y., Li, J., Zhang, S., Xia, C., Shi, S.Q., Cai, L., 2015. Enhancement of mechanical and thermal properties of Poplar through the treatment of glyoxal-urea/nano-SiO_2, *RSC Advances*, 5(67), 54148-54155.

Zhang, S., Xia, C., Dong, Y., Yan, Y., Li, J., Shi, S.Q., Cai, L., 2016. Soy protein isolate-based films reinforced by surface modified cellulose nanocrystal, *Industrial Crops and Products*, 80, 207-213.

CHAPTER 2

SELF-ACTIVATION: THEORY AND PARAMETERS [§]

2.1 Introduction

Activated carbon is a crude form of graphite with a random or amorphous structure, which is highly porous with a large internal surface area (*SA*) (Hamerlinck et al., 1994; Mohan and Pittman Jr, 2006). Various uses of activated carbon include purification (Hu et al., 2000), porous-supported catalysts (Blanco et al., 2006; Fabicovicova et al., 2014; Li et al., 2014; Pang et al., 2012), hydrogen storage capacity (Wang et al., 2009; Wang et al., 2014), and battery (Elazari et al., 2011; Manickam et al., 2013). The American Water Works Association (AWWA) B600 standard requires that the activated carbon has a specific surface area (*SSA*) in excess of 500 m^2 g^{-1} determined by N_2 adsorption at 77 K.

The process for activated carbon includes two steps, carbonization for the conversion of carbonaceous substances into carbon, and activation for the *SSA* and specific pore volume (*SPV*) increase of the converted carbon. The carbonaceous materials are usually pyrolyzed at temperatures between 600 – 900°C in an inert atmosphere for the carbonization, followed by the activation process (Mohan and Pittman Jr, 2006). Activation methods can be divided into two categories: (1) physical/thermal activation, and (2) chemical activation (Mohan and Pittman Jr, 2006). Physical/thermal activation uses a mild oxidizing gas, such as CO_2 or water steam

[§] This entire chapter is reproduced from Changlei Xia, Sheldon Q. Shi "Self-activation for activated carbon from biomass: theory and parameters" Green Chemistry, 2016, Accepted Manuscript, In Press, http://dx.doi.org/10.1039/C5GC02152A, with permission from the Royal Society of Chemistry (RSC).

(Mohan and Pittman Jr, 2006), to eliminate the bulk of the volatile matters, followed by partial gasification. The chemical activation method employs chemicals (such as acid, strong base, or salt) to increase the SSA, e.g. zinc chloride ($ZnCl_2$) (Zhang et al., 2010), potassium hydroxide (KOH) (Lua and Yang, 2004), sodium hydroxide (NaOH) (Xu et al., 2010), nitric acid (HNO_3) (Liu et al., 2011), sulfuric acid (H_2SO_4) (Gerçel and Gerçel, 2007), hydrochloric acid (HCl) (Alvarez et al., 2007), hydrogen peroxide (H_2O_2) (Moreno-Castilla et al., 1995), phosphoric acid (H_3PO_4) (Benadjemia et al., 2011), potassium carbonate (K_2CO_3) (Gurten et al., 2012), potassium phosphate dibasic (K_2HPO_4) (Aber et al., 2009), and cobalt acetate ($Co(OAc)_2$) (Gadkaree and Jaroniec, 2000). In the traditional activation process, physical activation using CO_2 and chemical activation using $ZnCl_2$ are two common methods. Both methods introduce additional gas (CO_2) or a chemical ($ZnCl_2$), from which both the CO_2 emission from the activation process and the zinc compound removal by acid from the follow-up process will cause environmental concerns. A comparison of self-activation and conventional activations is shown in Figure 2.1.

Self-activation process of biomass was first disclosed in our patent (Shi and Xia, 2014), which takes advantage of the gases emitted from the biomass during the carbonization process to serve as the activating agent, so that the carbonization and activation are combined into one step. A recent publication bearing the name “self-activation” (Bommier et al., 2015), presented a one-step pyrolysis of cellulose for activated carbon. A flowing argon was employed during the process. In the technology described in this paper, no gas was introduced during the self-activation process. The activated carbon fabricated through self-activation process presented high specific

surface area (up to 2432 m^2 g^{-1}), which is comparable with that manufactured by the conventional activation processes (up to 1926 m^2 g^{-1} for the physical activation, and 1642 m^2 g^{-1} for the chemical activation) (Yahya et al., 2015). Compared to the conventional activated carbon manufacturing, the cost of activating agents is saved using the self-activation technology, since no activating gas or chemical is used. In addition, the self-activation process is more environmentally friendly. The exhaust gases (CO and H_2) can be used as fuel or as feedstock for methanol production with further synthesis. To understand the mechanism of the self-activation process, a novel model is developed. The parameters (i.e. temperature, dwelling time, air, and moisture) affecting the self-activation are evaluated, and the changes of *SSA* and *SPV* on the yield of the self-activation are elucidated.

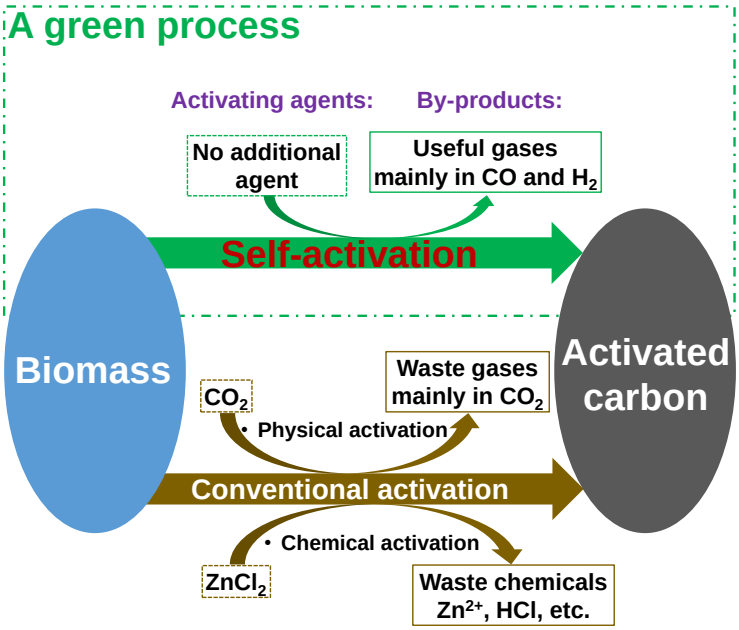

Figure 2.1 A comparison of self-activation and conventional activations.

2.2 Experimental

2.2.1 Self-Activation Process

A high-temperature versatile box furnace (STY-1600C, Sentro Tech Corp., USA) was used to process the PAC. The furnace is equipped with a vacuum system and gas flow with a maximum temperature of 1,600°C. A type-k thermocouple with a data logger (TC101A, MadgeTech, Inc., USA) was used in the furnace to detect the internal temperature. A digital pressure gauge (ADT680W-25-CP15-PSI-N, Additel Corp., USA) was used to measure the pressure of the furnace chamber. The heat chamber of the furnace is made with alumina ceramic with dimensions of 254 × 254 × 305 mm^3. The total volume of furnace was estimated as 350 litres measured using argon at low pressure based on the ideal gas Equation ($PV = nRT$).

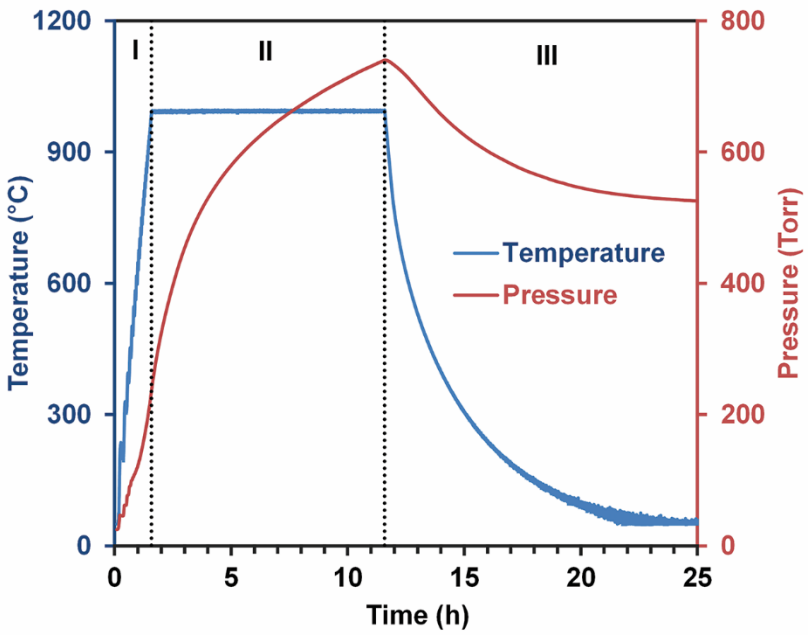

Figure 2.2 The internal pressure and temperature as a function of time in three pyrolysis periods: I) ramping (10°C min^{-1}); II) dwelling (for 10h); and III) controlled cooling (10°C min^{-1} and then self-cooling) to room temperature.

Figure 2.3 Ultra-fine pulverizing machine.

The following procedure was used for the self-activation pyrolysis process: 1) Placed the biomass into the box furnace chamber; 2) Set the vacuum to a pressure of -26 ± 1 Torr (96.6% vacuum). The valves of the furnace were then turned off to create a closed system so that no mass exchanging occurred during the pyrolysis process; and 3) Conducted pyrolysis process following the three steps: a) ramping with a temperature-increasing rate of 10°C min^{-1}; b) dwelling, and c) cooling with a temperature-decreasing rate of no more than 10°C min^{-1} to room temperature (Figure 2.2). The activated carbon products were then taken out from the furnace, and pulverized by an ultra-fine pulverizing machine (RT-UF26, Rong Tsong Precision Technology Co., Taiwan) (Figure 2.3) to match the size requirement of PAC according

with the AWWA B600 standard. The kenaf core based activated carbon sample was labelled as PAC (pyrolysis temperature, dwelling time), e.g. PAC (1,000°C, 10 h).

2.2.2 Non-Activation Process

For the specimens with self-activation, the biomass materials were placed inside the furnace with no cover which allowed the gases generated from the biomass to flow through the converted carbon material. For the specimens with non-activation, the biomass was put in a crucible, and a cap was used to cover the container so that limited gases would access the biomass materials. The biomass in the crucible (volume about 0.5 L) was pyrolyzed to generate gases, which flow out of the crucible to the furnace. When the pressure reached a balance inside and outside of the crucible, the gas exchange would stop. Thus, only a small amount of gases, 1.4% (0.5 L/350 L, crucible volume/furnace volume) remained in the crucible, which provided limited gas activation opportunity for the produced carbon, and was classified as non-activation.

Figure 2.4 3Flex surface area and pore size analyser and VacPrep 061 degasser.

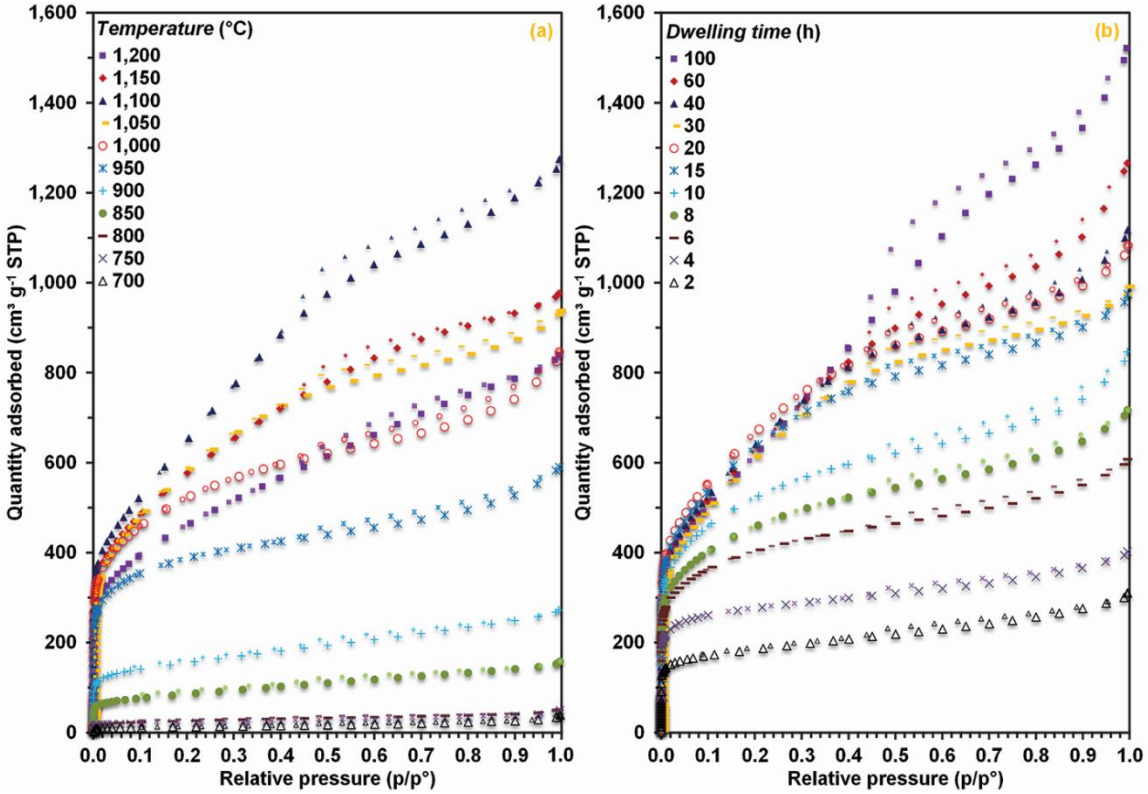

Figure 2.5 Isothermal plots of PACs at a) pyrolysis temperatures from 700°C to 1,200°C (dwelling time: 10 h) and b) dwelling times from 2 h to 100 h (pyrolysis temperature: 1,000°C).

2.2.3 Characterization

The adsorption capabilities of the PACs were determined by nitrogen adsorption at 77 K with a surface area and pore size analyser (3Flex 3500, Micromeritics Instrument Corp., USA) (Figure 2.4). The samples were vacuum degassed at 350°C for 3 – 5 days using a degasser (VacPrep 061, Micromeritics Instrument Corp., USA) (Figure 2.4) and then in-situ degassed at 350°C for 20 h by a turbo molecular drag pump prior to the analyses. Based on the isothermal plots (Figure 2.5), the *SSA* and *SPV* of the PACs were obtained by various models and shown in Table 2.1. The Brunauer–Emmett–Teller (BET) method was used for the overall *SSA* analysis. Density

Functional Theory (DFT) was used to calculate the overall *SPV* (pore sizes of those bigger than 0.393 nm). The *SSA* and *SPV* of meso-macropores were obtained from the BJH theory (pore sizes of 2 – 300 nm). The DFT model was used for determining the *SSA* and *SPV* of micropore (pore sizes of 0.393 – 2.002 nm).

Table 2.1 SSA and SPV of PAC samples processed at different temperatures and dwelling times.

Sample	*Yield* (%)	SSA_{BET} [b] ($m^2\ g^{-1}$)	$SSA_{BJH\ meso\text{-}macropore}$ [c] ($m^2\ g^{-1}$)	$SSA_{DFT\ micropore}$ ($m^2\ g^{-1}$)	SPV_{DFT} [d] ($cm^3\ g^{-1}$)	$SPV_{BJH\ meso\text{-}macropore}$ ($cm^3\ g^{-1}$)	$SPV_{DFT\ micropore}$ ($cm^3\ g^{-1}$)
PAC (700°C, 10 h) [a]	20.73	44	27	12	0.003	0.044	0.010
PAC (750°C, 10 h)	20.20	72	29	31	0.070	0.047	0.022
PAC (800°C, 10 h)	18.59	89	40	62	0.055	0.055	0.024
PAC (850°C, 10 h)	17.54	293	149	212	0.212	0.161	0.079
PAC (900°C, 10 h)	16.03	526	206	363	0.337	0.241	0.119
PAC (950°C, 10 h)	9.04	1,289	291	1121	0.749	0.423	0.498
PAC (1,000°C, 10 h)	5.16	1,932	587	1232	1.099	0.755	0.538
PAC (1,050°C, 10 h)	3.45	2,132	1,003	970	1.194	0.916	0.457
PAC (1,100°C, 10 h)	2.75	2,432	1,688	837	1.740	1.593	0.395
PAC (1,150°C, 10 h)	5.77	2,080	1,095	1019	1.281	1.028	0.445
PAC (1,200°C, 10 h)	6.73	1,634	824	903	1.292	0.894	0.370
PAC (1,000°C, 2 h)	16.13	611	183	615	0.401	0.263	0.195
PAC (1,000°C, 4 h)	12.67	901	180	921	0.502	0.251	0.321
PAC (1,000°C, 6 h)	8.51	1,360	339	1066	0.773	0.424	0.424
PAC (1,000°C, 8 h)	6.37	1,580	483	1052	0.918	0.561	0.445
PAC (1,000°C, 15 h)	4.65	2,266	848	1185	1.253	0.805	0.543
PAC (1,000°C, 20 h)	3.85	2,408	1,038	1149	1.393	0.989	0.530
PAC (1,000°C, 30 h)	3.60	2,252	1,150	980	1.307	1.010	0.458
PAC (1,000°C, 40 h)	3.58	2,342	1,213	1008	1.425	1.161	0.469
PAC (1,000°C, 60 h)	3.13	2,314	1,400	918	1.644	1.505	0.421
PAC (1,000°C, 100 h)	1.97	2,296	1,866	709	1.876	2.100	0.313
Ash	1.74	15	16	0	0.047	0.059	0.000

[a] Powdered activated carbon (pyrolysis temperature, dwelling time);

[b] BET = Brunauer–Emmett–Teller, *SSA* = specific surface area;

[c] BJH = Barrett-Joyner-Halenda;

[d] DFT = Density Functional Theory, *SPV* = specific pore volume.

Mass spectrometry (MS) analysis was performed by Inficon CPM residual gas analyzer (RGA). After the self-activation of kenaf core at 1,000°C for 30 h (cooling down to room temperature), the gas sample was collected in a bag from the furnace by a 1-liter Tedlar bag (Zefon International Inc., USA) for analysis.

Fourier transform infrared spectroscopy (FT-IR) was carried out by a Thermo-Fisher Nicolet 6700 FTIR analyzer, employing a 20-mL Pike flow cell. Two gas samples were collected by 1-liter Tedlar bags, including the emitted gases after the self-activation processes at 1,000°C for 2 h and 30 h, respectively.

2.3 Results and Discussion

2.3.1 Theory of Self-Activation

It was reported that the pyrolysis gases from biomass mainly contained H_2, CO_2, CO, CH_4, H_2O, etc. (Bommier et al., 2015; Yang et al., 2007) in which CO_2 and H_2O have been widely used to serve as activating agents in the activated carbon production (Mohan and Pittman Jr, 2006; Zhang et al., 2004). Therefore, the CO_2 and H_2O in the pyrolysis gases may activate the carbon, so that no additional gas needs to be introduced.

To demonstrate the self-activation process, one type of biomass, kenaf core (Biotech Mills Inc., USA, 3 – 30 meshes, 11.7% moisture content based on the ASTM D4442 standard), was used in a designed experiment. The dried kenaf core contains 49.0% cellulose, 29.7% hemicellulose, and 19.2% lignin (Nayeri et al., 2013), from which has 82.85% volatile matter (ASTM E872 standard), 15.41% fixed carbon, and 1.74% ash (ASTM E1755 standard). Carbon, hydrogen, oxygen, nitrogen, and sulfur

contents of kenaf core were found to be 48.00%, 6.37%, 42.10%, 0.35%, and 0.07%, respectively (Table 2.2) (Valerio et al., 2007). After self-activation at 1,000°C for 10 h, the resulted activated carbon contains 0.68% volatile matter (ASTM D5832 standard), 80.47% fixed carbon, and 18.85% ash (ASTM D2866 standard). The contents of carbon, hydrogen, oxygen, nitrogen, and sulfur of the resulted activated carbon were measured as 92.14%, 0.54%, 0.12%, 0.16%, and 0.02%, respectively (Table 2.2).

Table 2.2 Proximate analysis and ultimate analysis of kenaf core and activated carbon through self-activation process.

Sample	Proximate analysis (%)			Ultimate analysis (%)				
	Volatile matter	Fixed carbon	Ash	C	H	O	N	S
Kenaf core	82.85	15.41	1.74	48.00	6.37	42.10	0.35	0.07
PAC (1,000°C, 10 h)	0.68	80.47	18.85	92.14	0.54	0.12	0.16	0.02

From the ultimate analysis of the kenaf core, the chemical formula was found as $(C_{4.00}H_{6.32}O_{2.63})_n$. An equilibrium Equation of the pyrolysis of 179 g (equal to 1.86 mol of $C_{4.00}H_{6.32}O_{2.63}$) dried kenaf core was calculated from the FactSage software and databases and shown in Equation (1) (Bale et al., 2002).

$$1.86C_{4.00}H_{6.32}O_{2.63}(s) \xrightarrow{1{,}000^{o}C,\ 1atm} \begin{matrix} 2.57C(s) + 5.77H_2(g) + \\ 4.82CO(g) + 0.03H_2O(g) + \\ 0.03CH_4(g) + 0.02CO_2(g) + \cdots \end{matrix} \quad (1)$$

The pyrolysis condition was set as 1,000°C in temperature and 1 atm in pressure. From Equation (1), the yield of carbon at the equilibrium was obtained as 17.18% (2.57 mol), and the gas products resulting from the pyrolysis process were

mainly H_2 (5.77 mol) and CO (4.82 mol). Based on the Equation (1), experiments were carried out using the self-activation process (details in Experimental).

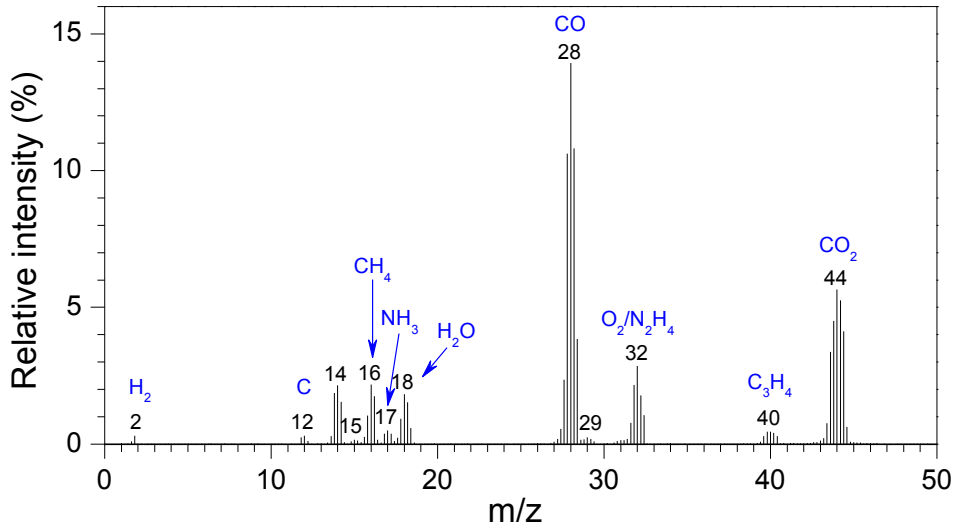

Figure 2.6 Mass spectrometry of the emitted gases from the self-activation of kenaf core at 1,000°C for 30 h.

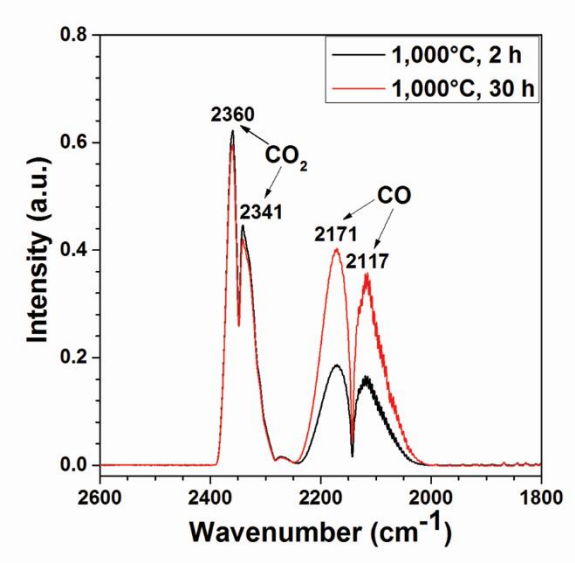

Figure 2.7 FT-IR absorbance of the emitted gases from self-activation processes at 1,000°C for 2 h and 30 h.

Table 2.3 FT-IR absorbance of CO_2 and CO in the emitted gases after self-activation processes at 1,000°C for 2 h and 30 h.

Parameter	FT-IR absorbance (a.u.) [a]				Value of CO/CO_2
	CO_2		CO		
	2360 cm^{-1}	2341 cm^{-1}	2171 cm^{-1}	2117 cm^{-1}	
1,000°C, 2 h	0.622	0.446	0.185	0.156	0.319
1,000°C, 30 h	0.596	0.420	0.400	0.342	0.730
Increase (%) [b]	-	-	-	-	128.8

[a] The four wavelengths are corresponding to the peaks in Figure 2.7;

[b] The increase of CO/CO_2 ratio from "1,000°C, 2 h" to "1,000°C, 30 h".

MS (Figure 2.6) and FT-IR (Figure 2.7) were performed on the gases emitted from the self-activation process to conform the Equation (1). The MS results showed that the emitted gases from self-activation of kenaf core included H_2, CO_2, CO, H_2O, CH_4, etc. In Figure 2.6, it showed that the H_2 amount was very little. This could be due to that some H_2 was diffused out through the Tedlar bag. The m/z peaks shown in Figure 2.6 at 12, 28, and 32 (C, CO, O_2) would have included those decomposed from CO_2, since the electron ionization was used. FT-IR was employed to examine the concentration changes of CO_2 and CO during the time (Figure 2.7 and Table 2.3). The peaks at 2360 and 2341 cm^{-1} belong to CO_2, and those at 2171 and 2117 cm^{-1} are attributed to CO (Yang et al., 2007). Comparing the gas components from self-activation at 1000°C for 2 h with those for 30 h, the CO/CO_2 ratio was increased by 128.8%, indicating that the CO_2 was reacted with C to generate CO with an increase of self-activation time.

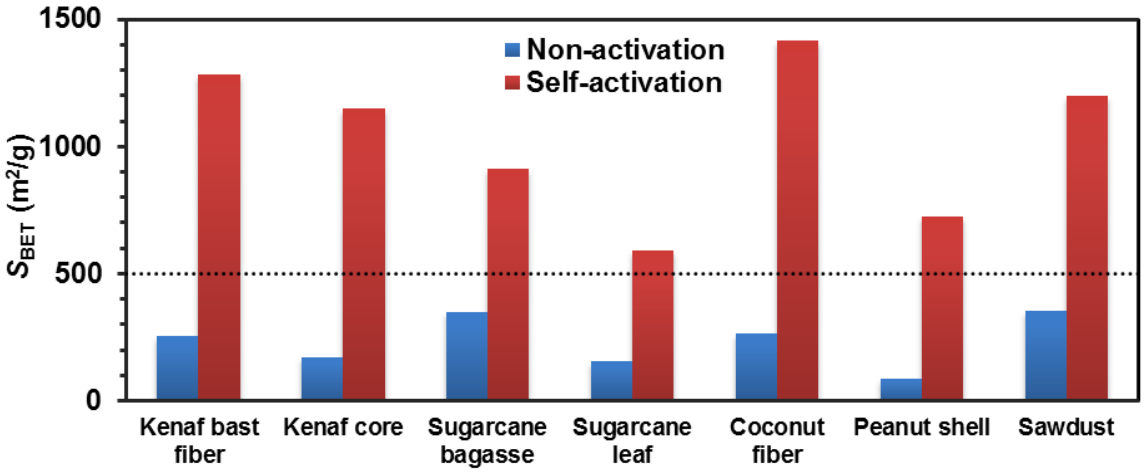

Figure 2.8 Comparisons of self-activation and non-activation.

2.3.2 Effectiveness of Self-Activation

The self-activation process was conducted on different biomass types, including kenaf fibre, kenaf core, sugarcane, sugarcane bagasse, sugarcane leaf, coconut fibre, peanut shell, and sawdust. A comparative experiment was conducted between the self-activation and non-activation (details in Experimental). Self-activation and non-activation were carried out in the same conditions except that for the self-activation, the material was activated by the emitted gases. Comparisons of self-activation and non-activation for different types of biomass are shown in Figure 2.8. The BET specific surface area (SSA_{BET}) results for different biomass types pyrolyzed at 1,100°C for 2 hours with self-activation or non-activation were: kenaf bast fibre ($SSA_{BET/Self\text{-}activation}$: 1,280 m^2 g^{-1}; $SSA_{BET/Non\text{-}activation}$: 252 m^2 g^{-1}; Increment: 408%), kenaf core (1,148 m^2 g^{-1}; 168 m^2 g^{-1}; 583%), sugarcane bagasse (910 m^2 g^{-1}; 349 m^2 g^{-1}; 161%), sugarcane leaf (591 m^2 g^{-1}; 155 m^2 g^{-1}; 281%), coconut fibre (1,413 m^2 g^{-1}; 264 m^2 g^{-1}; 435%), peanut shell (722 m^2 g^{-1}; 84 m^2 g^{-1}; 760%), and sawdust (1,199 m^2 g^{-1}; 354 m^2 g^{-1}; 239%). The activated carbon fabricated from the self-activation process presents a *SSA* greater than the

minimum requirement (500 m^2 g^{-1}) in accordance with the AWWA B600 standard. The results showed that the emitted gases had served as activating agents for the converted carbon from the biomass.

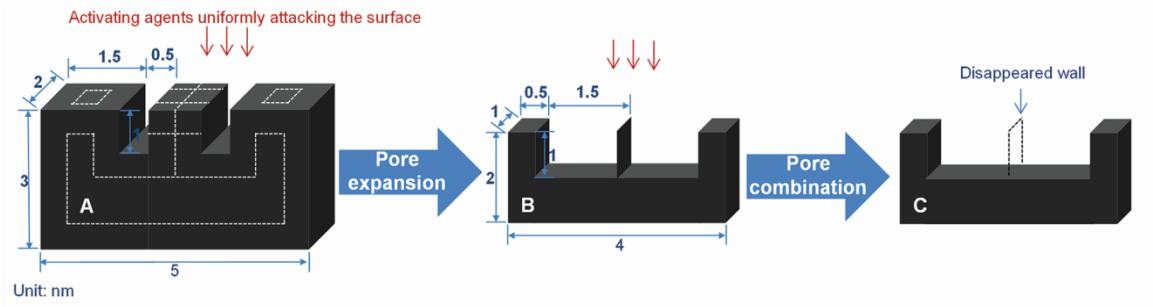

Figure 2.9 Illustration of the activation model. A carbon particle (A) (overall dimensions: 2 × 3 × 5 nm) with two pores (dimensions: 0.5 × 1 × 2 nm) was employed for the demonstration. After the pore expansion process (A to B), the SSA and SPV are increased by 114.1% and 8400%, respectively. After the pore combination process (B to C), the SSA is reduced by 7.7% and the SPV remains constant.

Table 2.4 Changes of SSA and SPV during the pore expansion and combination processes.

Status	A [g]	Pore expansion	B [g]	Pore combination	C [g]
SA [a] (nm^2)	68	↓58.8%	26	↓7.7%	24
PV [b] (nm^3)	2	↑50.0%	3	~0%	3
V [c] (nm^3)	28	↓82.1%	5	~0%	5
SSA [d] (nm^2 g^{-1})	2.4/D [f]	↑114.1%	5.2/D	↓7.7%	4.8/D
SPV [e] (nm^3 g^{-1})	0.071/D	↑8400%	0.6/D	~0%	0.6/D

[a] SA = surface area;

[b] PV = pore volume;

[c] V = volume of carbon particle;

[d] SSA =specific surface area, equal to SA/(V × D);

[e] SPV =specific pore volume, equal to PV/(V × D);

[f] D =density of carbon, assumed to be constant;

[g] A, B and C are related to the carbons in Figure 2.9.

2.3.3 An Activation Model

A number of models were developed to describe the activation process, such as kinetic models (Klose and Wolki, 2005; Ollero et al., 2002; Ollero et al., 2003; Senneca, 2007), gradual activation model (Mohammad-Khah and Ansari, 2009), and random pore model (RPM) (Matsumoto et al., 2009). However, these models have the limitations in explaining the changes of *SSA* and *SPV*. We developed a simplified model to describe the activation process as shown in Figure 2.9 and Table 2.4. Gas activation is an oxidation process on the carbon surface to increase the *SSA*. We assume that the oxidations happen uniformly on the entire surface of the carbon. Two scenarios may happen during the activation process: 1) pore expansion (A to B in Figure 2.9); and 2) pore combination (B to C in Figure 2.9). The pores are combined through the removal of the thin borders between the pores. During the pore expansion process, the *SA* and pore volume (*PV*) of the carbon particle are reduced by 58.8% and increased by 25%, respectively. In the meantime, the *SSA* and *SPV* are increased by 114.1% and 8,400%, respectively, with a corresponding 82.1% volume reduction. During the pore combination (B to C), both the surface area and the *SSA* are reduced by 7.7%, while the *SPV* is approximately constant. It indicates that the pore combination has negatively effect on the *SSA,* but little effect on the *SPV*. In the activation process, the *SSA* is increased by pore expansion, but is decreased by pore combination, from which the total *SSA* maybe unchanged during the process. In general, for the change of *SSA*, pore expansion dominates during the early stage of the pyrolysis process. As the pyrolysis process continues, pore expansion and pore combination will be balanced until the pore combination is gradually dominating. Eventually, the material will be

turned into ash. As the pore volume may not be affected by the pore combination, the *SPV* will keep increasing. Experiments were conducted to validate the developed activation model and are presented in a later section of the paper.

2.3.4 Pyrolysis Parameters for Self-Activation

The effect of different pyrolysis parameters on the efficiency of the self-activation process was studied. Kenaf core was selected for the investigation of the self-activation process. The following pyrolysis parameters were investigated: pyrolysis temperature, dwelling time, air in the furnace, and moisture of the kenaf core. Pyrolysis experiments were conducted on the kenaf core at different temperatures between 700 – 1,200°C with an interval of 50°C, dwelling for 10 hours. The relationship between yield and pyrolysis temperature is shown in Figure 2.10a. Four phases can be identified in Figure 2.10a: I) 700 – 898°C, II) 898 – 970°C, III) 970 – 1,090°C, and IV) 1,090 – 1,200°C. High yields (20.73 – 16.24%) were obtained in Phase I. As the pyrolysis temperature increased, the yield decreased, and a slow self-activation was presented in Phase I. In Phase II, as the temperature increased from 898°C to 970°C, the yield continued to decrease, and the yield reduction became much more rapid (0.14 % $°C^{-1}$) compared to that in Phase I (0.023% $°C^{-1}$). In Phase III, the yield reduction rate decreased to 0.034% $°C^{-1}$, indicating that the temperature had less effect on the yield reduction. In Phase IV, the yield increased as the pyrolysis temperature increased. This could be explained that during Phase IV, the decomposition rate of gases into carbon exceeded the gasification rate of the carbon by the activating gases.

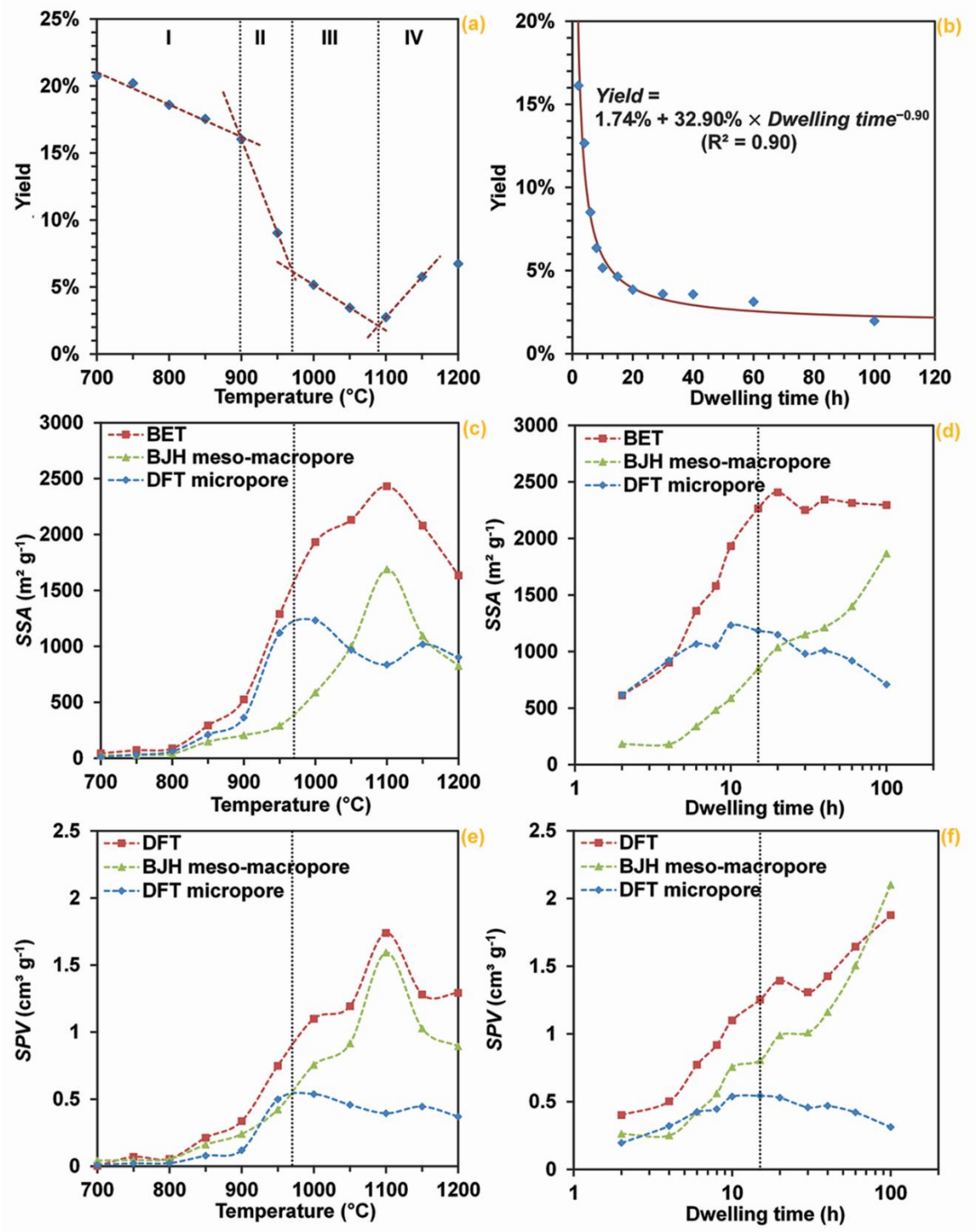

Figure 2.10 Temperature-dependent changes (pyrolysis time: 10 hours) of a) yield, c) SSA and e) SPV, and dwelling time-dependent changes (pyrolysis temperature: 1,000°C) of b) yield, d) SSA and f) SPV.

Figure 2.10b indicates a relationship between the yield and the dwelling time at a pyrolysis temperature of 1,000°C. Figure 2.10b shows that, as the dwelling time increased, the yield decreased rapidly at the initial stage and then slowed down until it levelled off. The process followed the exponential function:

$$Yield = 1.74\% + 32.90\% \times Dwelling\ time^{-0.90} \quad (2)$$

where 1.74% is the ash content determined based on the procedure described in ASTM E1755 standard. The coefficient of determination (R^2) for the Equation (2) was 0.90.

The effects of pyrolysis temperature and dwelling time on the SSA_{BET}, *SSA* of Barrett–Joyner–Halenda (BJH) meso-macropore ($SSA_{BJH\ meso\text{-}macropore}$), *SSA* of DFT micropore ($SSA_{DFT\ micropore}$), *SPV* of DFT overall pores (SPV_{DFT}), *SPV* of BJH meso-macropore ($SPV_{BJH\ meso\text{-}macropore}$), and *SPV* of DFT micropore ($SPV_{DFT\ micropore}$) were investigated, and the results are shown in Figure 2.10c-f. The changes of *SSA* and *SPV* as a function of pyrolysis temperature are shown in Figure 2.10c and Figure 2.10e, respectively. The SSA_{BET} of the activated carbon was lower than 500 $m^2\ g^{-1}$, when the kenaf core was pyrolyzed only in the stage of Phase I (Figure 2.10a), i.e. 700, 750, 800, and 850°C. During the stage Phase II (898 – 970°C), the SSA_{BET} and $SSA_{DFT\ micropore}$ increased quickly. The quickest increase for $SSA_{BJH\ meso\text{-}macropore}$ happened in Phase III (970 – 1090°C). The $SSA_{DFT\ micropore}$ reached the maximum at around 970°C, indicating that the micropore started to be translated into mesopore by the pore expansion process. In Phase III (970 – 1090°C), SSA_{BET} increased slightly slower than that of the $SSA_{BJH\ meso\text{-}macropore}$, because the pores were changed from micropore to mesopore during the pore expansion process. In Phase IV (1090 – 1200°C), the $SSA_{DFT\ micropore}$

remained the same, while the SSA_{BET} and $SSA_{BJH\ meso\text{-}macropore}$ decreased. Similar trends were found for the SPV_{DFT}, $SPV_{BJH\ meso\text{-}macropore}$ and $SPV_{DFT\ micropore}$ (Figure 2.10e).

The specific surface area (SSA_{BET}, $SSA_{BJH\ meso\text{-}macropore}$, and $SSA_{DFT\ micropore}$) changes as a function of dwelling time (at 1,000°C pyrolysis temperature) as shown in Figure 2.10d. In general, SSA_{BET} increased during the first 15 h and then stabilized. The $SSA_{BJH\ meso\text{-}macropore}$ increased throughout the whole pyrolysis period. The $SSA_{DFT\ micropore}$ reached the maximum at around 10 hours and then decreased. The *SPV* changes ($SPV_{BJH\ meso\text{-}macropore}$, $SPV_{DFT\ micropore}$, and SPV_{DFT}) as a function of dwelling time are shown in Figure 2.10f. As it is seen in Figure 2.10f, the $SPV_{BJH\ meso\text{-}macropore}$ shows a similar trend to that of the $SSA_{BJH\ meso\text{-}macropore}$ (Figure 2.10d). The $SPV_{DFT\ micropore}$ also shows a similar trend to that of the $SSA_{DFT\ micropore}$ (Figure 2.10d). However, while the total surface area (SSA_{BET}) levels off at a certain dwelling time (about 15 hours), the total pore volume (SPV_{DFT}) continues to increase beyond the 15-hour dwelling time. This finding indicated that the pore expansion and pore combination was balanced at the dwelling time of about 15 hours. During the activation process, the micropore was expanded into the mesopore by the pore expansion. For the internal pores in the activated carbon, when the walls between the adjacent pores disappear because of the pore expansion, the *PV* will continue to increase, while the *SA* may be decreased. Therefore, the pore combination will have a significant effect to the *SPV* of micropore and the total *SSA*, but litter effect to the meso-macropore and total *SPV*. The results indicated that the pore combination would be minor when the meso-macropore were important for the activated carbon.

Table 2.5 The effects of the moisture of biomass and the air-free condition of the furnace on the yield and specific surface area of the self-activated carbon.

Dwelling time (h)		2			10			Equilibrium [a]		
Conditions	Moisture [c]	Yes	No	No	Yes	No	No	Yes	No	No
	Air [d]	Yes	Yes	No	Yes	Yes	No	Yes	Yes	No
Yield (%)		16.13	16.54	17.04	5.16	6.21	7.05	7.93	15.71	17.18
SSA_{BET} [b] (m^2 g^{-1})		611	558	507	1932	1825	1689	-	-	-

[a] Theory data, calculated by FactSage software;

[b] SSA_{BET} = BET specific surface area;

[c] 21 g moisture in 200 g kenaf core;

[d] 11.8 L of air in the furnace (96.6% vacuum).

In order to investigate the effect of moisture in the biomass on the self-activation process, kenaf core with a moisture content of 9.1% was used for the pyrolysis experiments at an initial pressure of -26 ± 1 Torr (96.6% vacuum). From the ideal gas Equation, around 11.8 L of air was estimated to remain in the furnace. The pyrolysis treatment were carried out at 1,000°C for 2 or 10 h on the kenaf core samples at three conditions: (1) 200 g (21 g moisture) in 11.8 L air condition, (2) 179 g (dried) in 11.8 L air condition, and (3) 179 g (dried) in air-free condition. The air-free condition was achieved by applying vacuum and introducing argon into the furnace for three times. Before the pyrolysis experiments, the pressure in the furnace was kept at 96.6% vacuum with argon introduced. Table 2.5 shows the yield and SSA_{BET} of activated carbon processed at different conditions. When the other conditions remain the same, air and moisture in the furnace will accelerate the activation process of the materials (showing reduced yields and increased SSA_{BET}). The moisture and carbon dioxide in the air may serve as activating agents directly to activate the converted carbon, while the oxygen may react with biomass/converted carbon to form CO_2 as an activation

agent, so that a self-activation process can be implemented. The more the activating agent generated in the furnace, the faster the self-activation process would be.

The estimated yields for the self-activation at equilibrium was calculated using the FactSage software. The results, as seen in Table 2.5, show that the estimated yields agree with the measured yield results from the experiments. There are about 21% O_2 in the atmospheric environment, which are about 0.11 mol O_2 in the 11.8 L air (estimated from 350 L of furnace in 96.6% of vacuum). During the self-activation processes, the Equation of kenaf core with moisture and 11.8 L air in the furnace was estimated by the FactSage software and shown in Equation (3):

$$1.86C_{4.00}H_{6.32}O_{2.63}(s) + 1.17H_2O(l) + 0.11O_2(g) \xrightarrow{1{,}000^oC,\ 1atm} 1.18C(s) + 6.92H_2(g) + 6.18CO(g) + 0.04H_2O(g) + 0.03CH_4(g) + 0.02CO_2(g) + \cdots \quad (3)$$

The Equation of dried kenaf core and 11.8 L air in the furnace is shown in Equation (4):

$$1.86C_{4.00}H_{6.32}O_{2.63}(s) + 0.11O_2(g) \xrightarrow{1{,}000^oC,\ 1atm} 2.34C(s) + 5.77H_2(g) + 5.03CO(g) + 0.03H_2O(g) + 0.03CH_4(g) + 0.02CO_2(g) + \cdots \quad (4)$$

As shown in Table 2.5, the yields of the activated carbon pyrolyzed for 10 hours were much less than the yields that were pyrolyzed for 2 hours. The longer the pyrolysis, the less the yield. However, Table 2.5 also indicates that the yields at equilibrium estimated from the FactSage software were greater than the measured yields pyrolyzed for 10 hours. The reasons for these results can be twofold: 1) during the pyrolysis process, the biomass materials are decomposed into small molecules, some of which are vaporized, which causes some carbon losses; and 2) since the

activity of carbon (α) at the location of the sample is higher than that at other locations in the furnace, the Equation (5) goes reversely at the sample location, but not at the other locations. It was observed from the experiments that the inner surface of the furnace chamber was coated by a layer of carbon after the pyrolysis experiments.

$$2CO(g) \rightleftharpoons C(s) + O_2(g) \quad (5)$$

2.3.5 Yield-Dependent Surface Areas and Pore Volumes

According to the SSA_{BET} data in Table 2.1, a relationship between ln(SSA_{BET}) and the yield for the powdered activated carbon (PAC) was plotted and presented in Figure 2.11a. A linear relationship was established as shown below with a R^2 of 0.98.

$$\ln(SSA_{BET}) = -11.14 \times Yield + 8.16 \quad (6)$$

Please be noticed that a few data points were excluded in the analysis. These data points were presented in high yield end (PACs (700-850°C, 10 h)), which did not agree with most of the main trends. Some volatile matters might still be in the carbon, as the total residue from the volatile test was 17.15% (including 15.41% fixed carbon and 1.74% ash), which was lower than the measured yield of PACs (700-850°C, 10 h), i.e. 17.54 – 20.73%. These volatile matters would occupy the pores of the carbon, resulting in a lower SSA_{BET} than that in the trend line (Figure 2.11a). The abnormal data points at the low yield end (PAC (1,000°C, 100 h) and ash) were also excluded. The ash is an extreme case for the pyrolysis process with a minimum SSA_{BET}. For the PAC processed at 1,000°C, at 100 hours, the pore combination dominated the process (Figure 2.9), resulting in the SA_{BET} reduction.

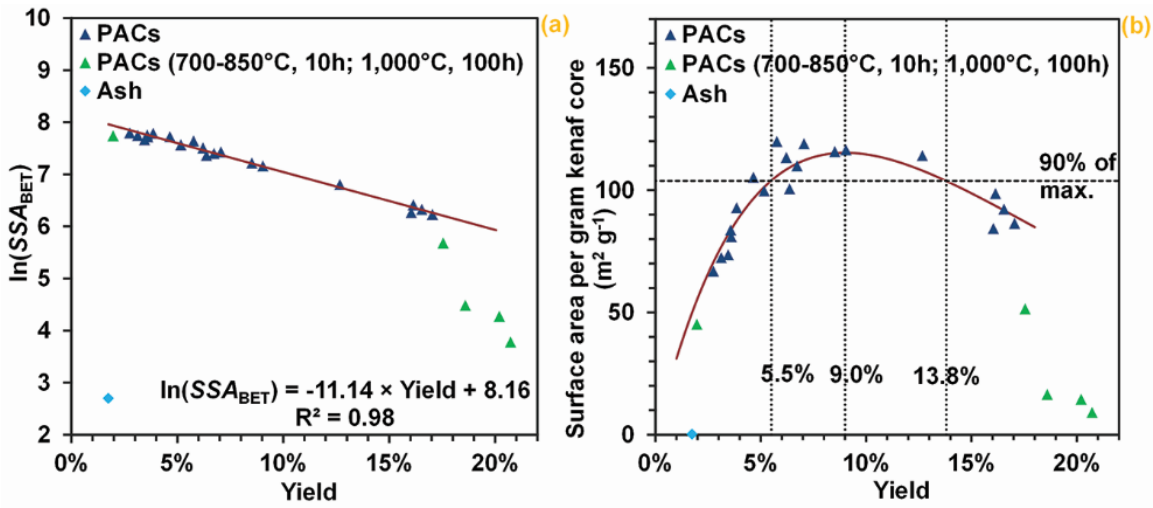

Figure 2.11 The relationships between the yield and a) nature log of the SSA_{BET} and b) the surface area per gram of the kenaf core.

The efficiency of total surface area generation from kenaf core was analysed and presented in Figure 2.11b. The surface area per gram kenaf core can be calculated by:

$$\textit{Surface area per gram kenaf core} = SSA_{BET} \times \textit{Yield} \quad (7)$$

Combining Equations (6) and (7), the relationship between surface area per gram kenaf core and yield can be obtained as:

$$\textit{Surface area per gram kenaf core} = e^{-11.14 \times \textit{Yield} + 8.16} \times \textit{Yield} \quad (8)$$

Figure 2.11b shows a comparison of the model estimates (Equation (8)) and the measured data for the relationship between the surface area per gram of kenaf core and the yield. It can be concluded from Figure 2.11b that the established model (Equation (8)) is a good predictor for the unit surface area. Figure 2.11b shows that the activated carbon from kenaf core with the yields between 5.5 – 13.8% are the most

efficient in activated carbon production, from which the highest unit surface area (115 m^2 g^{-1}) of the PAC was obtained at the yield of 9.0%.

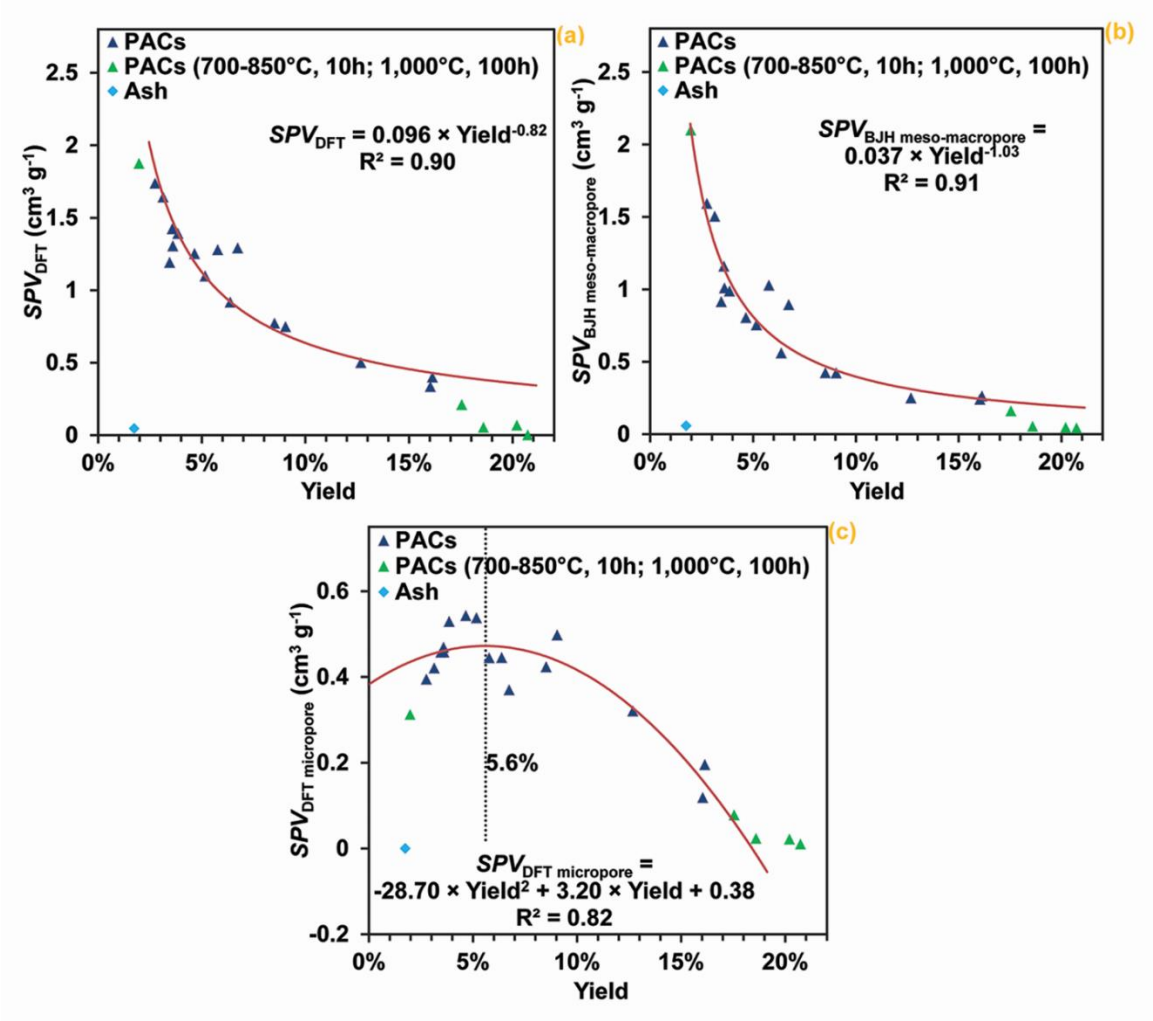

Figure 2.12 The relationships between yield and *SPV* from the models of a) DFT; b) BJH meso-macropore; and c) DFT micropore.

Usually, the larger the pore volume, the higher the capability of the activated carbon can be obtained to absorb the impurities. Absorptions for different sizes of the impurities require different pore volumes for the activated carbon. Micropores in the activated carbon tend to absorb small molecules (e.g. iodine), while meso-macropores

absorb large molecules (e.g. tannic acid). Figure 2.12 shows the relationships between the yields and the pore volumes for the three different pore volumes, including total pore volume (SPV_{DFT}), mesa-macropore volume ($SPV_{BJH\ meso\text{-}macropore}$), and micropore volume ($SPV_{DFT\ micropore}$). Again, the points of PACs (700-850°C, 10 h; 1,000°C, 100 h) and ash were not included in the analysis.

For the relationship between SPV_{DFT} and yield as shown in Figure 2.12a, a power fitting Equation was established as shown in Equation (9).

$$SPV_{DFT} = 0.096 \times Yield^{-0.82} \quad (9)$$

SPV_{DFT} represents the total pore volume of micro-macropores.

The BJH model is applied to the analysis of meso-macropore volume. The calculation range of BJH was set to be 2 – 300 nm. As shown in Figure 2.12b, a power fitting can also be applied to describe the data with an established Equation shown in Equation (10).

$$SPV_{BJH\ meso\text{-}macropore} = 0.037 \times Yield^{-1.03} \quad (10)$$

The micropore volume was analysed using the DFT model (Figure 2.12c). It was noticed from Figure 2.12c that some $SPV_{DFT\ micropore}$ data showed negative values, which were not realistic. A relationship between the micropore volume and the yield was established following the second order fitting as shown in Equation (11).

$$SPV_{DFT\ micropore} = -28.70 \times Yield^{2} + 3.20 \times Yield + 0.38 \quad (11)$$

The $SPV_{DFT\ micropore}$ reached a maximum when the yield was around 5.6%. Based on the proposed activation theory discussed in Figure 2.9, the size of the pore increases

during the activation process. When the pore size exceeds 2 nm, the pore is no longer considered a micropore. Therefore, at a certain point of activation, the micropore volume starts to decrease.

2.4 Conclusions

Self-activation is an effective activation process for activated carbon from biomass. The activated carbons were successfully produced without any additional activating gases or chemicals. A model of the activation process was developed to understand and explain the self-activation process. In the study of self-activation of kenaf core, the suggested pyrolysis temperature for the self-activation process is between 970 – 1,090°C, and the most effective pyrolysis temperature is expected to be around 1,090°C. The relationships between yields and specific surface areas (SSA_{BET}), specific pore volumes (SPV_{DFT}, $SPV_{BJH\ meso\text{-}macropore}$, and $SPV_{DFT\ micropore}$) were investigated, i.e. a lineal fitting between ln(SSA_{BET}) and yields, power fittings between SPV_{DFT}, $SPV_{BJH\ meso\text{-}macropore}$ and yields, and a second-order fitting between $SPV_{DFT\ micropore}$ and yields. The changes of specific surface areas (SSA_{BET}, $SSA_{BJH\ meso\text{-}macropore}$, and $SSA_{DFT\ micropore}$) and specific pore volumes (SPV_{DFT}, $SPV_{BJH\ meso\text{-}macropore}$, and $SPV_{DFT\ micropore}$) as a function of pyrolysis temperatures and dwelling times agree with our model prediction. In the analysis of these relationships, the PACs (700-850°C, 10 h; 1,000°C, 100 h) and ash were not included. In addition, the study of the effectiveness of kenaf core for producing highest total surface area showed that the yield of 9.0% received a maximum surface area per using gram kenaf core, and the yields between 5.5% and 13.8% were recommended for more than 90% of effectiveness.

2.5 References

Aber, S., Khataee, A., Sheydaei, M., 2009. Optimization of activated carbon fiber preparation from Kenaf using K2HPO4 as chemical activator for adsorption of phenolic compounds, *Bioresource Technology*, 100(24), 6586-6591.

Alvarez, P., Blanco, C., Granda, M., 2007. The adsorption of chromium (VI) from industrial wastewater by acid and base-activated lignocellulosic residues, *Journal of Hazardous Materials*, 144(1), 400-405.

Bale, C., Chartrand, P., Degterov, S., Eriksson, G., Hack, K., Mahfoud, R.B., Melançon, J., Pelton, A., Petersen, S., 2002. FactSage thermochemical software and databases, *Calphad*, 26(2), 189-228.

Benadjemia, M., Millière, L., Reinert, L., Benderdouche, N., Duclaux, L., 2011. Preparation, characterization and Methylene Blue adsorption of phosphoric acid activated carbons from globe artichoke leaves, *Fuel Processing Technology*, 92(6), 1203-1212.

Blanco, J., Petre, A.L., Yates, M., Martin, M.P., Suarez, S., Martin, J.A., 2006. Novel one-step synthesis of porous-supported catalysts by activated-carbon templating, *Advanced Materials*, 18(9), 1162-1165.

Bommier, C., Xu, R., Wang, W., Wang, X., Wen, D., Lu, J., Ji, X., 2015. Self-activation of cellulose: A new preparation methodology for activated carbon electrodes in electrochemical capacitors, *Nano Energy*, 13, 709-717.

Elazari, R., Salitra, G., Garsuch, A., Panchenko, A., Aurbach, D., 2011. Sulfur-impregnated activated carbon fiber cloth as a binder-free cathode for rechargeable Li-S batteries, *Advanced Materials*, 23(47), 5641-5644.

Fabicovicova, K., Malter, O., Lucas, M., Claus, P., 2014. Hydrogenolysis of cellulose to valuable chemicals over activated carbon supported mono- and bimetallic nickel/tungsten catalysts, *Green Chemistry*, 16(7), 3580-3588.

Gadkaree, K., Jaroniec, M., 2000. Pore structure development in activated carbon honeycombs, *Carbon*, 38(7), 983-993.

Gerçel, Ö, Gerçel, H.F., 2007. Adsorption of lead (II) ions from aqueous solutions by activated carbon prepared from biomass plant material of Euphorbia rigida, *Chemical Engineering Journal*, 132(1), 289-297.

Gurten, I.I., Ozmak, M., Yagmur, E., Aktas, Z., 2012. Preparation and characterisation of activated carbon from waste tea using K_2CO_3, *Biomass and Bioenergy*, 37, 73-81.

Hamerlinck, Y., Mertens, D., Vansant, E., 1994. Activated Carbon Principles in Separation Technology. Elsevier, New York.

Hu, Z.H., Srinivasan, M.P., Ni, Y.M., 2000. Preparation of mesoporous high-surface-area activated carbon, *Advanced Materials*, 12(1), 62-65.

Klose, W., Wolki, M., 2005. On the intrinsic reaction rate of biomass char gasification with carbon dioxide and steam, *Fuel*, 84(7-8), 885-892.

Li, Z., Kelkar, S., Raycraft, L., Garedew, M., Jackson, J.E., Miller, D.J., Saffron, C.M., 2014. A mild approach for bio-oil stabilization and upgrading: electrocatalytic hydrogenation using ruthenium supported on activated carbon cloth, *Green Chemistry*, 16(2), 844-852.

Liu, L., Deng, Q., Liu, Y., Ren, T., Yuan, Z., 2011. HNO_3-activated mesoporous carbon catalyst for direct dehydrogenation of propane to propylene, *Catalysis Communications*, 16(1), 81-85.

Lua, A.C., Yang, T., 2004. Effect of activation temperature on the textural and chemical properties of potassium hydroxide activated carbon prepared from pistachio-nut shell, *Journal of Colloid and Interface Science*, 274(2), 594-601.

Manickam, S.S., Karra, U., Huang, L., Nhu-Ngoc Bui, Li, B., McCutcheon, J.R., 2013. Activated carbon nanofiber anodes for microbial fuel cells, *Carbon*, 53, 19-28.

Matsumoto, K., Takeno, K., Ichinose, T., Ogi, T., Nakanishi, M., 2009. Gasification reaction kinetics on biomass char obtained as a by-product of gasification in an entrained-flow gasifier with steam and oxygen at 900-1000 degrees C, *Fuel*, 88(3), 519-527.

Mohammad-Khah, A., Ansari, R., 2009. Activated charcoal; preparation, characterization and applications: a review article, *International Journal of ChemTech Researc*h, 1, 859-864.

Mohan, D., Pittman Jr, C.U., 2006. Activated carbons and low cost adsorbents for remediation of tri-and hexavalent chromium from water, *Journal of Hazardous Materials*, 137(2), 762-811.

Moreno-Castilla, C., Ferro-Garcia, M., Joly, J., Bautista-Toledo, I., Carrasco-Marin, F., Rivera-Utrilla, J., 1995. Activated carbon surface modifications by nitric acid, hydrogen peroxide, and ammonium peroxydisulfate treatments, *Langmuir*, 11(11), 4386-4392.

Nayeri, M.D., Tahir, P.M., Harun, J., Abdullah, L.C., Bakar, E.S., Jawaid, M., Namvar, F., 2013. Effects of temperature and time on the morphology, pH, and buffering capacity of bast and core kenaf fibres, *BioResources*, 8(2), 1801-1812.

Ollero, P., Serrera, A., Arjona, R., Alcantarilla, S., 2003. The CO_2 gasification kinetics of olive residue, *Biomass & Bioenergy*, 24(2), 151-161.

Ollero, P., Serrera, A., Arjona, R., Alcantarilla, S., 2002. Diffusional effects in TGA gasification experiments for kinetic determination, *Fuel*, 81(15), 1989-2000.

Pang, M., Liu, C., Xia, W., Muhler, M., Liang, C., 2012. Activated carbon supported molybdenum carbides as cheap and highly efficient catalyst in the selective hydrogenation of naphthalene to tetralin, *Green Chemistry*, 14(5), 1272-1276.

Senneca, O., 2007. Kinetics of pyrolysis, combustion and gasification of three biomass fuels, *Fuel Processing Technology*, 88(1), 87-97.

Shi, S.Q., Xia, C., 2014. Porositization process of carbon or carbonaceous materials, US patent 14/211,357.

Valerio, V., Villone, A., Nanna, F., Barisano D., 2007. Chemical characterisation of biomass feedstocks for the gasifier test, http://www.uniqueproject.eu/public/deliverables/D5.3.pdf, UNIQUE Project, Accessed on 3/8/2016.

Wang, H., Gao, Q., Hu, J., 2009. High hydrogen storage capacity of porous carbons prepared by using activated carbon, *Journal of the American Chemical Society*, 131(20), 7016-7022.

Wang, J., Senkovska, I., Kaskel, S., Liu, Q., 2014. Chemically activated fungi-based porous carbons for hydrogen storage, *Carbon*, 75, 372-380.

Xu, B., Chen, Y., Wei, G., Cao, G., Zhang, H., Yang, Y., 2010. Activated carbon with high capacitance prepared by NaOH activation for supercapacitors, *Materials Chemistry and Physics*, 124(1), 504-509.

Yahya, M.A., Al-Qodah, Z., Ngah, C.W.Z., 2015. Agricultural bio-waste materials as potential sustainable precursors used for activated carbon production: A review, *Renewable & Sustainable Energy Reviews*, 46, 218-235.

Yang, H., Yan, R., Chen, H., Lee, D.H., Zheng, C., 2007. Characteristics of hemicellulose, cellulose and lignin pyrolysis, *Fuel*, 86(12-13), 1781-1788.

Zhang, H., Yan, Y., Yang, L., 2010. Preparation of activated carbon from sawdust by zinc chloride activation, *Adsorption*, 16(3), 161-166.

Zhang, T.Y., Walawender, W.P., Fan, L.T., Fan, M., Daugaard, D., Brown, R.C., 2004. Preparation of activated carbon from forest and agricultural residues through CO_2 activation, *Chemical Engineering Journal*, 105(1-2), 105, 53-59.

CHAPTER 3

SELF-ACTIVATION OF KENAF FIBER [§]

3.1 Introduction

Activated carbon is a crude form of graphite with a random or amorphous structure, which is highly porous with a large internal surface area (Hamerlinck et al., 1994; Mohan and Pittman Jr, 2006). Activated carbon may exhibit a broad range of pore sizes from visible cracks or crevices to slits of molecular dimensions. Generally, activated carbon has a specific surface area of higher than 500 m^2/g as determined by the gas adsorption technique. In the adsorption analysis, non-polar gases, e.g. N_2, CO_2, Ar, and CH_4, are usually used, from which N_2 adsorption at 77 K is widely used (Mohan and Pittman Jr, 2006).

The use of carbon can be traced back to ancient times. The earliest use of carbon in the form of wood chars (charcoal) was reported in 3750 BC by the Egyptians and Sumerians (Inglezakis and Poulopoulos, 2006). Activated carbon was first produced on an industrial scale in the early part of the twentieth century in Europe. In the early stage, the activated carbon was in the form of powder, called powdered activated carbon (PAC). Recently, many types of activated carbon, e.g. granular activated carbon (GAC) and pelletized activated carbon, have been developed. The Swedish chemist von Ostreijko obtained two patents, in 1900 and 1901, covering the basic concepts of chemical and physical/thermal activation of carbon, with metal

[§] This entire chapter is reproduced from Changlei Xia, Sheldon Q. Shi "Self-activation process to fabricate activated carbon from kenaf" Wood and Fiber Science, 2016, 48: 62–69, http://wfs.swst.org/index.php/wfs/article/view/2342/2271, with permission from the Society of Wood Science and Technology (SWST).

chlorides and with carbon dioxide and steam, respectively (Sontheimer et al., 1988). In 1909, a plant named 'Chemische Werke' was built to manufacture, for the first time on a commercial scale, the PAC Eponit® from wood, adopting von Ostrejko's gasification approach (Dabrowski, 1999).

Mozammel et al. (2002) reported that the activated carbon sales in the world market were estimated as 375,000 tons in 1990, excluding the sales in Eastern Europe and China. If Eastern Europe and China were considered, the total sales could be over 450,000 tons. By the late 1990s, the world market was estimated at about 700,000 tons/year, with a market growth of about 4 – 6%/year. The global activated carbon market was about $1.8 billion in 2011 and is estimated to reach $3.0 billion by 2016. In a recent report "World Activated Carbon to 2016", the worldwide activated carbon demand is expected to increase more than 10% per year to 1.9 million metric tons through 2016 (The Freedonia Group, 2012).

Currently, the methods of activation include physical/thermal and chemical activation (Wikipedia, 2016). The physical/thermal activation uses a mild oxidizing gas, e.g. CO_2 and water steam, to eliminate the bulk of the volatile matters, followed by partial gasification during the pyrolysis (Hameed and El-Khaiary, 2008; Rodriguezreinoso et al., 1995; Zhang et al., 2004). High porosity and surface area can be obtained from the physical/thermal activation method. Another activation method, called chemical activation, employs chemicals to increase the surface area (Aber et al., 2009; Lua and Yang, 2004; Shi et al., 2015; Xu et al., 2010; Zhang et al., 2010). Prior to the activation, the raw materials are impregnated with certain chemicals (e.g. $ZnCl_2$, KOH, NaOH, K_2HPO_4, etc.), and then are processed by the activation steps.

The self-activation process of biomass described in this research takes advantage of the gases emitted from the biomass during the carbonization process to serve as the activation agent, so that the carbonization and activation are combined into one step (Shi and Xia, 2014; Xia and Shi, 2015; Xia and Shi, 2016). From the literatures (Crombie and Masek, 2014; Mukarakate et al., 2014; Yang et al., 2007), the pyrolysis gases from the biomass mainly contain H_2, CO, H_2O, CO_2, CH_4, etc., in which CO_2 and H_2O have been widely used as activating agents in the activated carbon manufacturing (Mohan and Pittman Jr, 2006; Zhang et al., 2004). Thus, the pyrolysis gases, CO_2 and H_2O, may serve as activating agents to activate the carbon.

In our recent research, the activated carbon fabricated through self-activation process using kenaf core presented high specific surface area (up to 2,432 m^2/g) (Xia and Shi, 2016). In this work, kenaf fiber was employed for the self-activation process, and the highest specific surface area can be obtained as 1,742 m^2/g, which is comparable to that manufactured through the conventional activation processes (up to 1,926 m^2/g for the physical activation, and 1,642 m^2/g for the chemical activation) (Yahya et al., 2015).

Compared to conventional activated carbon manufacturing, using the self-activation saves the cost of activating agents and reduces the environmental impact, as compared with conventional activation processes. Physical activation using CO_2 and chemical activation using $ZnCl_2$ are two common methods in the conventional activation process. Both processes introduce additional CO_2 (Mohan and Pittman Jr, 2006) or $ZnCl_2$ (Zhang et al., 2010), from which both the CO_2 emission (the main emitted gas is still CO_2) from the activation process and the zinc compound removal by acid from the

follow-up process cause environmental concerns. However, the exhausting gases (mainly CO and H_2) from self-activation process can be used as fuel or as feedstock for methanol production with further synthesis.

In this study, self-activation process of kenaf fiber is investigated. The parameters of self-activation, including temperature and dwelling time, are evaluated, and the changes of specific surface area on the yield are elucidated. Additionally, the effective utilization of kenaf fibers for producing highest total surface area is discussed in this paper.

3.2 Materials and Methods

3.2.1 Self-Activation Process

A high-temperature versatile box furnace (STY-1600C, Sentro Tech Corp., USA) was used for the experiment (Figure 3.1a). The box furnace has a type-k thermocouple with a data logger (TC101A, MadgeTech, Inc., USA) for detecting the internal temperature, and a digital pressure gauge (ADT680W-25-CP15-PSI-N, Additel Corp., USA) for measuring the pressure of the furnace chamber. Kenaf fiber was obtained from Kengro Corp., USA. The moisture content of the fiber was measured as 11.7% based on the procedure described in ASTM D4442 standard (ASTM, 2010). A self-activation process was conducted on the kenaf fiber. The following procedures were carried out:

1) The kenaf fiber was placed into the box furnace chamber;

2) A vacuum was applied to the furnace for about 2 hours to reach a pressure of -734.36 ± 0.26 Torr (96.6% vacuum), and then all the values of the furnace were turned off to keep a closed system; and

3) The temperature of the furnace was increased in three steps (Figure 3.1b): A) ramping with 10°C/min, B) dwelling, and C) cooling with no more than 10°C/min to room temperature.

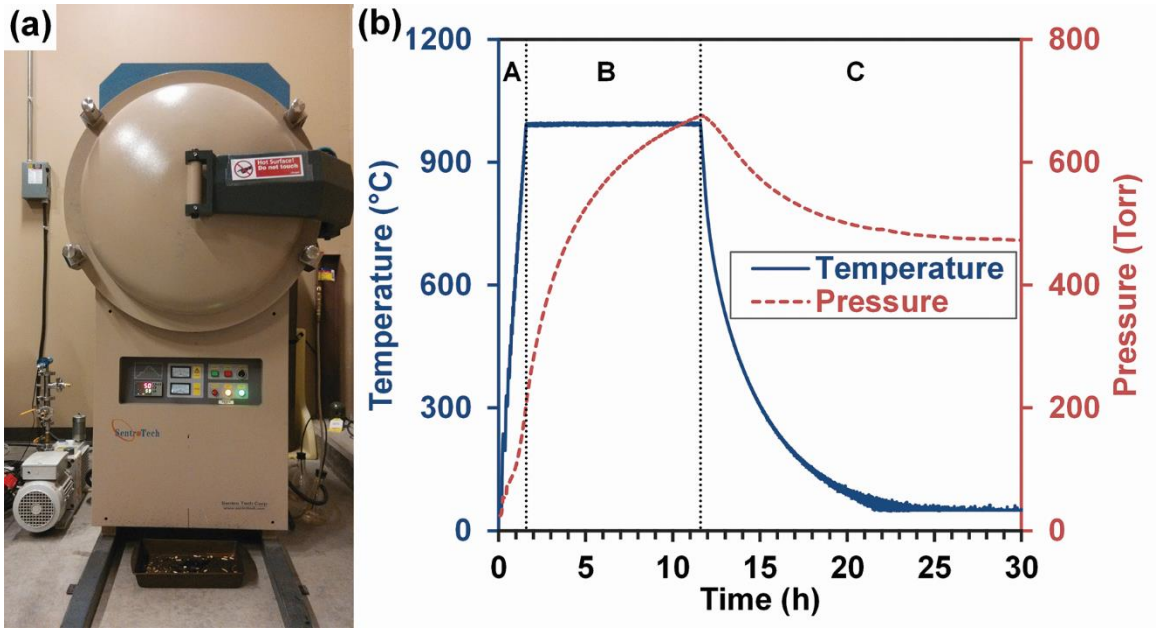

Figure 3.1 A box furnace (a) and (b) the internal pressure and temperature as a function of time in three pyrolysis periods: A) ramping of 10°C/min; B) dwelling for 10h; C) controlled cooling of 10°C/min and then self-cooling to room temperature.

3.2.2 Non-Activation

Comparative experiment was designed and carried out for examining the difference between self-activation and non-activation (Figure 3.2a). For the specimens with self-activation, the kenaf fiber was placed inside the furnace with no cover, which

allowed the gases generated from the biomass to flow through the converted carbon material. For the specimens with non-activation, the biomass was put in a crucible, and a cap was used to cover the container so that limited gases would access the biomass materials. The biomass in the crucible (volume about 0.5 L) was pyrolyzed to generate gases, which flowed out of the crucible to the furnace. When the pressure reached a balance inside and outside of the crucible, the gas exchange would stop. Thus, only a small amount of gases, 1.4% (0.5 L/350 L, crucible volume/furnace volume) remained in the crucible, which provided limited gas activation opportunity for the material. It was considered as non-activation.

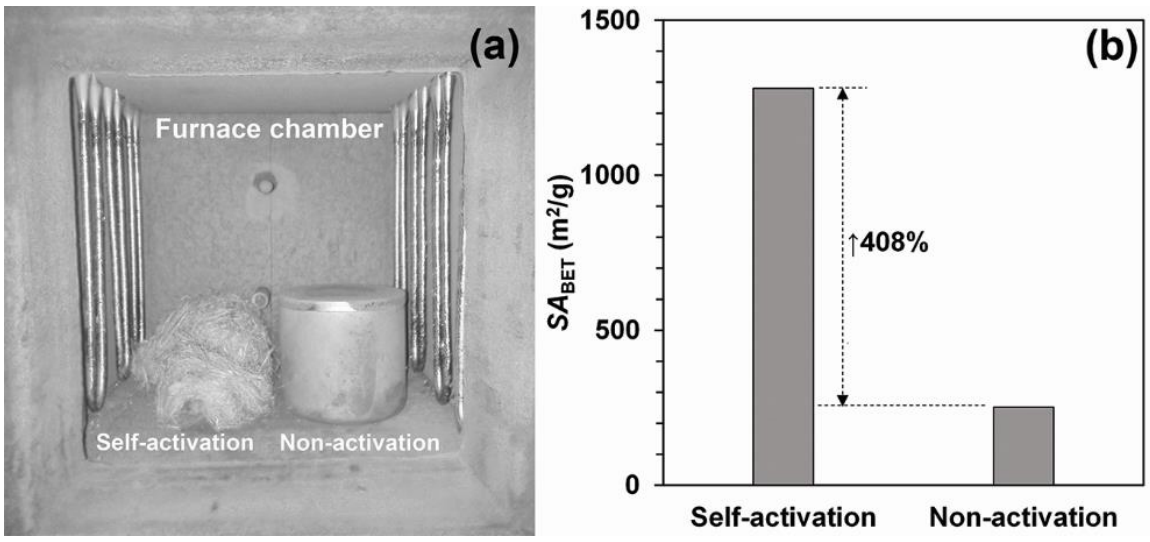

Figure 3.2 Self-activation vs. non activation: (a) Kenaf fibers in the furnace and (b) the SA_{BET} values.

Table 3.1 Data summary of the pyrolysis products with different parameters.

Sample	Pyrolysis temperature (°C)	Dwelling time (h)	Yield (%)	SA_{BET} [a] (m^2/g)
PAC (700°C, 10h)	700	10	17.08	122
PAC (750°C, 10h)	750	10	16.58	139
PAC (800°C, 10h)	800	10	15.99	194
PAC (850°C, 10h)	850	10	15.45	290
PAC (900°C, 10h)	900	10	13.14	542
PAC (950°C, 10h)	950	10	8.49	844
PAC (1,000°C, 2h)	1,000	2	11.28	681
PAC (1,000°C, 4h)	1,000	4	8.96	956
PAC (1,000°C, 6h)	1,000	6	7.49	1,072
PAC (1,000°C, 8h)	1,000	8	6.65	1,336
PAC (1,000°C, 10h)	1,000	10	3.52	1,534
PAC (1,000°C, 15h)	1,000	15	3.20	1,616
PAC (1,000°C, 30h)	1,000	30	2.91	1,540
PAC (1,000°C, 40h)	1,000	40	2.06	1,558
PAC (1,000°C, 60h)	1,000	60	1.34	282
PAC (1,050°C, 10h)	1,050	10	2.16	1,561
PAC (1,100°C, 10h)	1,100	10	2.21	1,742
PAC (1,150°C, 10h)	1,150	10	4.58	1,460
Ash [b]	650	12	1.16	34

[a] SA_{BET} = Brunauer–Emmett–Teller (BET) specific surface area;

[b] Ash content was determined in accordance with ASTM D2866 standard (ASTM, 2011) that kenaf core was pyrolyzed in an air-atmosphere muffle furnace at 650°C for 12 hours.

3.2.3 Characterization

Prior to the characterization, the activated carbon products were crushed into a powder by an ultra-fine pulverizing machine (RT-UF26, Rong Tsong Precision Technology Co., Taiwan). According to the ANSI/AWWA B600 standard (ANSI/AWWA, 2010), the requirements for the particle-size distribution of powdered activated carbon

(PAC) are: not less than 99% of the activated carbon shall pass a No. 100 sieve, not less than 95% shall pass a No. 200 sieve, and not less than 90% shall pass a No. 325 sieve. The activated carbon sample was labelled as PAC (pyrolysis temperature, dwelling time), e.g. PAC (1,000°C, 10 h).

The N_2 gas adsorption capabilities of the PACs were determined by nitrogen adsorption at 77 K with a surface area and pore size analyzer (3Flex 3500, Micromeritics Instrument Corp., USA). The samples were vacuum degassed at 350°C for 3–5 days using a degasser (VacPrep 061, Micromeritics Instrument Corp., USA), and then *in situ* degassed at 350°C for 20 hours by a turbo molecular drag pump (EXT75DX 63CF, Edwards Limited, Crawley, West Sussex, UK). Specific surface areas were calculated from the isothermal plots through the instrumental software (3Flex Version 1.02, Micromeritics Instrument Corp., USA). Brunauer–Emmett–Teller (BET) method was used for the specific surface area analysis. The pyrolysis parameters, yields, and BET specific surface area (SA_{BET}) are summarized in Table 3.1.

3.3 Results and Discussion

3.3.1 Self-Activation versus Non-Activation

Self-activation and non-activation were compared by a comparative experiment (Figure 3.2a). Both self-activation and non-activation were carried out at 1,100°C for 2 hours. The SA_{BET} of self-activation and non-activation were obtained as 1,280 m^2/g and 252 m^2/g, respectively, from which 408% increase was calculated with the self-activation compared with the non-activation (Figure 3.2b). It was indicated that the converted carbon was activated by the emitted gases during the self-activation process.

3.3.2 Yield versus Pyrolysis Parameters

The effect of different pyrolysis parameters (pyrolysis temperature and dwelling time) on the efficiency of the self-activation process was studied. Pyrolysis experiments were conducted on the kenaf fiber at different temperatures between 700 – 1,150°C with an interval of 50°C, dwelling for 10 hours. The relationship between yield and pyrolysis temperatures is shown in Figure 3.3a. Four phases can be identified in Figure 3.3a: A) 700 – 880°C, B) 880 – 1,000°C, C) 1,000 – 1,080°C, and D) 1,080 – 1,150°C. High yields (17.08% – 15.45%) were obtained in Phase A, compared to Phase B-D. As the pyrolysis temperature increased, the yield decreased, and a slow self-activation was presented in Phase A. In Phase B, as the temperature increased from 880°C to 1,000°C, the yield continued to decrease, and the reduction in yield accelerated (0.096 %/°C) compared to that in Phase I (0.011%/°C). In Phase C, the yield reduction rate decreased to 0.027%/°C, indicating that the temperature had less effect on the yield reduction. In Phase D, the yields increased as the pyrolysis temperature increased. The reason could be that the decomposition rate (gases into carbon) exceeded the gasification rate of the carbon by the activating gases during the Phase D (Xia and Shi, 2016).

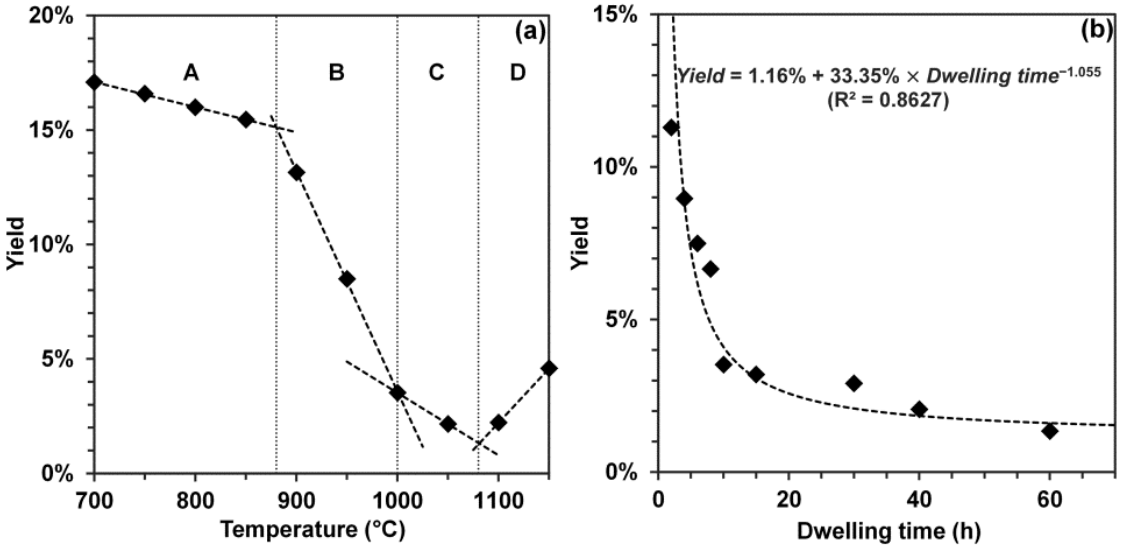

Figure 3.3 The yield of the activated carbon as a function of (a) pyrolysis temperature (pyrolysis time: 10 hours) and (b) pyrolysis time (pyrolysis temperature: 1,000°C).

Figure 3.3b shows a relationship between the yield and the dwelling time at a pyrolysis temperature of 1,000°C. As illustrated in Figure 3.3b, as the dwelling time increased, the yield decreased rapidly at the initial stage and then slowed down until it was levelled off. The process followed the exponential function:

$$Yield = 1.16\% + 33.35\% \times Dwelling\ time^{-1.055} \quad (1)$$

where 1.16% is the ash content determined based on the procedure described in ASTM D2866 standard (ASTM, 2011). The coefficient of determination (R^2) for Equation (1) was 0.8627.

3.3.3 Specific Surface Area versus Pyrolysis Parameters

The effects of pyrolysis temperature and dwelling time on the SA_{BET} of activated carbon were investigated, and the results are shown in Figure 3.4. The SA_{BET} changes

as a function of pyrolysis temperature (dwelling time: 10 hours) are shown in Figure 3.4a. In general, SA_{BET} increased as the pyrolysis temperature increased from 700°C to 1,000°C, and then levelled off. Figure 3.4b shows that the SA_{BET} increased during the first 10 hours and then levelled off. This phenomena was consistent with our previous research on the self-activation for kenaf core (Xia and Shi, 2016), in which the SA_{BET} of produced activated carbon became constant after 15 hours of self-activation (pyrolysis temperature: 1,000°C). However, the SA_{BET} suddenly dropped when the pyrolysis time increased from 40 h to 60 h, i.e. SA_{BET} from 1,558 m^2/g to 282 m^2/g. The reason could be that the yield of the sample with 60-hour pyrolysis time was 1.34%, which was very close to the ash content, 1.16%, at which the SA_{BET} value was only 34 m^2/g.

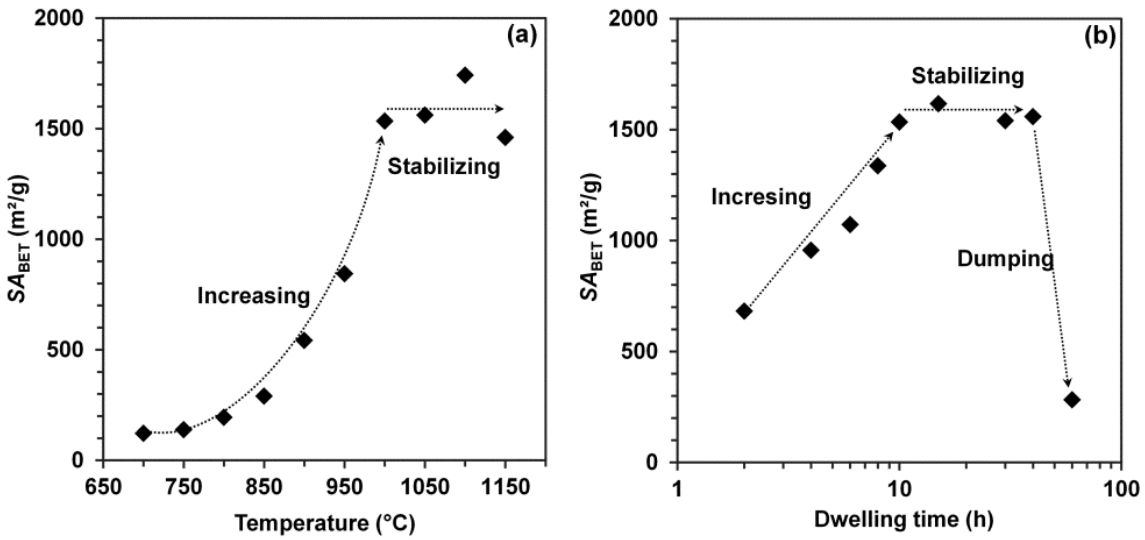

Figure 3.4 The specific surface area of activated carbon as a function of (a) pyrolysis temperature (pyrolysis time: 10 hours) and (b) pyrolysis time (pyrolysis temperature: 1,000°C).

3.3.4 Yield-Dependent Specific Surface Area

According to the data in Table 3.1, it was found that the surface area of the produced activated carbon from self-activation process could be designed by controlling the yields. A relationship between ln(SA_{BET}) and yield (Figure 3.5a) was established as the following equation with R^2 equal to 0.9577:

$$\ln(SA_{BET}) = -9.8460 \times Yield + 7.6702 \quad (2)$$

PACs (700-850°C, 10 h) were excluded in the analysis because they had relatively lower SA_{BET} and higher yields. The possible reason could be that some volatile matters remain during the relatively low temperature (700-850°C), resulting in the blocking of the pores (Xia and Shi, 2016). The yield of PAC (1,000°C, 60h) was 1.34%, very close to the ash content (1.16%), causing a dramatic reduction of SA_{BET}. In general, the SA_{BET} of the activated carbon increased as the yield is decreased to a certain point, and then the SA_{BET} decreased until turning into ash. An activation model (Xia and Shi, 2016) was developed to explain the changes of SA_{BET} on the yield. Two steps were included in the activation model, i.e. pore expansion, and pore combination. At the initial stage, pore expansion dominates. The small pores are expanded, while the specific surface area is increased. After a certain point, pore expansion dominates. Two or more pores are combined into one pore, while the specific surface area is dramatically reduced because of the disappearing wall between the pores. During the final stage, the produced activated carbon turns into ash.

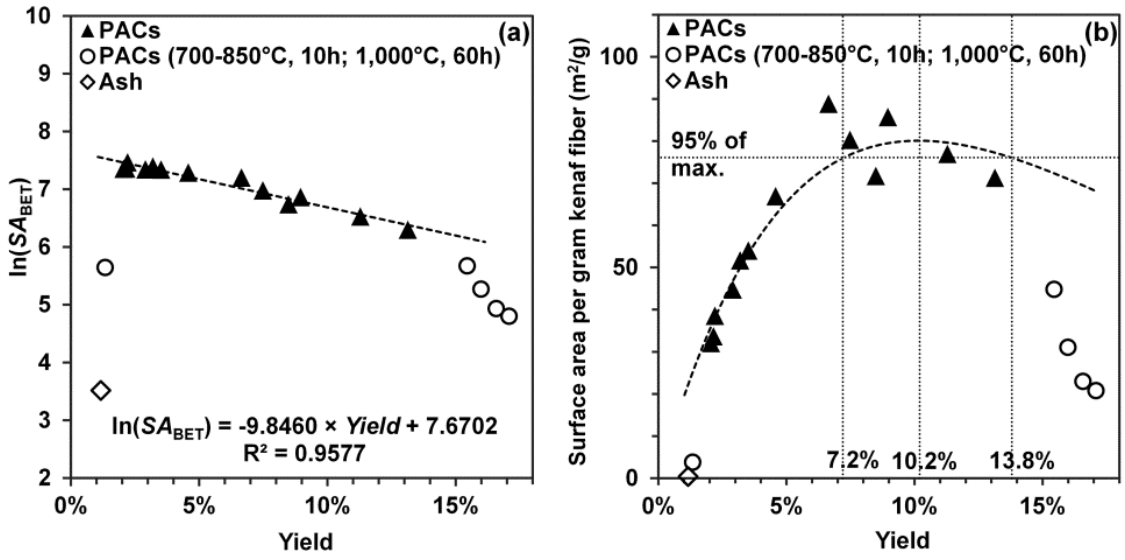

Figure 3.5 The relationships between the yields of activated carbon and (a) ln(SA_{BET}) and (b) the total surface area produced by 1 g biomass.

The efficiency of total surface area generation from kenaf fiber was analyzed (Figure 3.5b). The surface area per gram kenaf fiber was calculated using the following equation:

$$Surface\ area\ per\ gram\ biomass\ = SA_{\mathrm{BET}} \times Yield \quad (3)$$

According Equations (2) and (3), a relationship between surface area per gram biomass and yield was established and shown in Equation (4):

$$Surface\ area\ per\ gram\ biomass\ = \mathrm{e}^{-9.8460 \times Yield + 7.6702} \times Yield \quad (4)$$

The data calculated from Equation (4) were plotted and, as shown in Figure 3.5b (dash line), the PAC with a yield of 10.2% gives the highest surface area by gram kenaf fiber (80 m^2 per gram biomass). The yields between 7.2% – 13.8% produce a surface area per gram kenaf fiber within 95% of the maximum (76 m^2 per gram kenaf fiber).

These results provide a guide for taking full advantage of kenaf fiber to create the maximum surface area by controlling the yields.

3.4 Conclusions

Self-activation is an effective activation process for activated carbon from biomass. The kenaf fiber based activated carbon was successfully produced using the self-activation process without introducing additional activating gases or chemicals. The comparisons of self-activation and non-activation showed that the surface area of produced carbon can be dramatically increased. The relationships between yields and surface area (SA_{BET}) were found to have a lineal fitting between ln(SA_{BET}) and yields. In additional, the study of kenaf fiber's effectiveness for producing highest total surface area showed that the yield of 10.2% received a maximum surface area per using gram kenaf fiber, and the yields between 7.2% and 13.8% were recommended to obtain an effectiveness of more than 95% of the maximum.

3.5 References

Aber, S., Khataee, A., Sheydaei, M., 2009. Optimization of activated carbon fiber preparation from Kenaf using K_2HPO_4 as chemical activator for adsorption of phenolic compounds, *Bioresource Technology*, 100(24), 6586-6591.

ANSI/AWWA, 2010. ANSI/AWWA B600 - Powdered activated carbon. American National Standards Institute/American Water Works Association, doi: 10.12999/AWWA.B600.10.

ASTM, 2011. ASTM D2866 - Standard test method for total ash content of activated carbon, American Society for Testing and Materials.

ASTM, 2010. ASTM D4442 - Standard test methods for direct moisture content measurements of wood and wood-base materials. American Society for Testing and Materials.

Crombie, K., Masek, O., 2014. Investigating the potential for a self-sustaining slow pyrolysis system under varying operating conditions, *Bioresource Technology*, 162, 148-156.

Dabrowski, A., 1999. Adsorption-its development and application for practical purposes, *Studies in Surface Science and Catalysis*, 123, 3-28.

Hameed, B.H., El-Khaiary, M.I., 2008. Equilibrium, kinetics and mechanism of malachite green adsorption on activated carbon prepared from bamboo by K_2CO_3 activation and subsequent gasification with CO_2, *Journal of Hazardous Materials*, 157(2-3), 344-351.

Hamerlinck, Y., Mertens, D., Vansant, E., 1994. Activated Carbon Principles in Separation Technology. Elsevier, New York.

Inglezakis, V., Poulopoulos, S., 2006. Adsorption, Ion Exchange and Catalysis: Design of Operations and Environmental Applications. Elsevier, New York.

Lua, A.C., Yang, T., 2004. Effect of activation temperature on the textural and chemical properties of potassium hydroxide activated carbon prepared from pistachio-nut shell, *Journal of Colloid and Interface Science*, 274(2), 594-601.

Mohan, D., Pittman Jr, C.U., 2006. Activated carbons and low cost adsorbents for remediation of tri-and hexavalent chromium from water, *Journal of Hazardous Materials*, 137(2), 762-811.

Mozammel, H.M., Masahiro, O., Sc, B., 2002. Activated charcoal from coconut shell using $ZnCl_2$ activation, *Biomass and Bioenergy*, 22(5), 397-400.

Mukarakate, C., Watson, M.J., ten Dam, J., Baucherel, X., Budhi, S., Yung, M.M., Ben, H., Iisa, K., Baldwin, R.M., Nimlos, M.R., 2014. Upgrading biomass pyrolysis vapors over beta-zeolites: role of silica-to-alumina ratio, *Green Chemistry*, 16(12), 4891-4905.

Rodriguezreinoso, F., Molinasabio, M., Gonzalez, M.T., 1995. The use of steam and CO_2 as activating agents in the preparation of activated carbons, *Carbon*, 33(1), 15-23.

Shi, S.Q., Che, W., Liang, K., Xia, C., Zhang, D., 2015. Phase transitions of carbon-encapsulated iron oxide nanoparticles during the carbonization of cellulose at various pyrolysis temperatures, *Journal of Analytical and Applied Pyrolysis*, 115, 1-6.

Shi, S.Q., Xia, C., 2014. Porositization process of carbon or carbonaceous materials, US patent 14/211,357.

Sontheimer, H., Crittenden, J.C., Summers, R.S., Hubele, C., 1988. Activated Carbon for Water Treatment, 2 edition ed. DVGW-Forschungsstelle, Engler-Bunte-Institut, Universitat Karlsruhe (TH).

The Freedonia Group, 2012. World Activated Carbon to 2016, http://www.freedoniagroup.com/brochure/28xx/2878smwe.pdf, Accessed on 3/8/2106.

Wikipedia, 2016. Activated Carbon, https://en.wikipedia.org/wiki/Activated_carbon, Accessed on 3/8/2016.

Xia, C., Shi, S.Q., 2015. Self-activation process for biomass based activated carbon, *Proceedings of 58th International Convention of Society of Wood Science and Technology (SWST)*, 2015, 98-104.

Xia, C., Shi, S.Q., 2016. Self-activation for activated carbon from biomass: theory and parameters, *Green Chemistry*, Accepted Manuscript, In Press, doi: 10.1039/C5GC02152A.

Xu, B., Chen, Y., Wei, G., Cao, G., Zhang, H., Yang, Y., 2010. Activated carbon with high capacitance prepared by NaOH activation for supercapacitors, *Materials Chemistry and Physics*, 124(1), 504-509.

Yahya, M.A., Al-Qodah, Z., Ngah, C.W.Z., 2015. Agricultural bio-waste materials as potential sustainable precursors used for activated carbon production: A review, *Renewable & Sustainable Energy Reviews*, 46, 218-235.

Yang, H., Yan, R., Chen, H., Lee, D.H., Zheng, C., 2007. Characteristics of hemicellulose, cellulose and lignin pyrolysis, *Fuel*, 86(12-13), 1781-1788.

Zhang, H., Yan, Y., Yang, L., 2010. Preparation of activated carbon from sawdust by zinc chloride activation, *Adsorption*, 16(3), 161-166.

Zhang, T.Y., Walawender, W.P., Fan, L.T., Fan, M., Daugaard, D., Brown, R.C., 2004. Preparation of activated carbon from forest and agricultural residues through CO_2 activation, *Chemical Engineering Journal*, 105(1-2), 53-59.

CHAPTER 4

LITHIUM-ION BATTERY ANODE [§]

4.1 Introduction

Lithium-ion batteries (LIBs) have been one of the most commonly used electrical energy storage devices for electric vehicles (EVs) and portable electronics due to the remarkable characteristics such as high operating voltage (>3.0V), high energy densities (110-170 Wh kg^{-1} and 230-400 Wh L^{-1}), long cycle life, and low self-discharge rate (Manthiram, 2003). Furthermore, the recent developments of portable electronic devices demands excellent electrochemical performance including cycling stability and high rate capability (Winter et al., 2003). To realize this challenge, the development of highly efficient, alternative anode materials is inevitable to overcome a current limitation of commercially available graphite anode, which has a low theoretical specific capacity of 372 mAh g^{-1} (Kang et al., 2015). Nanostructured carbons are promising as alternative anode materials owing to their unique physico-chemical properties including large surface area, short diffusion length for lithium ions, and high electrical conductivity (de las Casas and Li, 2012). These properties are closely responsible for the outstanding LIB performance for a variety of nanostructured carbon anode materials previously reported (e.g carbon nanotubes (Sharifi et al., 2015) and graphene (Jeong et al., 2013; Novák et al., 2009)). Compared to these carbon anodes, the activated carbon enables exhibits its exceptional high surface area (2494 m^2 g^{-1}) and porosity (2.28 cm^3

[§] This entire chapter is from the manuscript: Changlei Xia, Chiwon Kang, Mumukshu D. Patel, Liping Cai, Bharat Gwalani, Raj Banerjee, Sheldon Q. Shi, Wonbong Choi “Activated carbons extracted from pine wood for high-performance lithium-ion battery” 2016, In Submitting.

g^{-1}) with hierarchical porous structures, which are unique properties to obtain high LIB performance (Hou et al., 2015).

In a recent study, Hou et al. synthesize the activated carbon derived from biorenewable silk as an anode material for LIB, showing a high specific capacity of 1,401 mAh g^{-1} at 1C with cycling stability and C-rate capability (Hou et al., 2015). Nevertheless, most activated carbon reported so far has been manufactured by the physical/chemical activation (Mohan and Pittman Jr, 2006), which may cause detrimental impact on the environment. For instance, chemical activation using $ZnCl_2$ (Lua and Yang, 2004), the zinc-compound needs to be removed from the activated carbon by strong concentrating acids (e.g. HCl, H_2SO_4), which introduces chemical wastes. Furthermore, the physical activation using CO_2 gas may raise environmental issues (Yahya et al., 2015), as it is considered as a major component of greenhouse gases (Knox et al., 2015; Rao and Rubin, 2002; Zhang et al., 2015). Both chemical and physical activations lead to environmental concerns, and the multiple steps in fabrication may require a high cost as well. To address these current limitations, an alternative activation, coined self-activation, is developed and reported.

Self-activation of biomass is first disclosed in our patent (Shi and Xia, 2014), which utilize the emission of gases from carbonization process to serve as the activating agents, so that no additional activating agents are required for activation process (Xia and Shi, 2015; Xia and Shi, 2016a; Xia and Shi 2016b). As reported, the pyrolytic gases from the biomass contain CO_2 and H_2O, widely used as activating agents for producing activated carbon (Bommier et al., 2015; Yang et al., 2007; Zhang et al., 2004; Shi et al., 2015). Therefore, the CO_2 and H_2O in the pyrolysis gases may activate the carbon; as a

result, no additional gas is required. A recent publication containing the term “self-activation” presents a one-step pyrolysis of cellulose for activated carbon (Bommier et al., 2015); however, flowing argon is essential during the process. The self-activation of a kenaf core, without introducing any gas or chemical, proved that the emitted CO_2 could serve as an activating agent. We have also thoroughly investigated the self-activation theory and parameters monitoring the process (Xia and Shi, 2016a).

In this study, we have developed a novel, facile, and environmental-friendly process of self-activation for converting pine (Pinus) wood into activated carbons with their applications in LIB anode. The pine wood-derived activated carbon possesses high SSA and SPV of 2738 $m^2\ g^{-1}$ and 2.209 $cm^3\ g^{-1}$, respectively, which are superior to those obtained from the conventional activation processes (1926 $m^2\ g^{-1}$ from coconut shell and 1720 $m^2\ g^{-1}$ from cotton stalk for the physical and chemical activation processes, respectively) (Yahya et al., 2015), self-activation of cellulose (2602 $m^2\ g^{-1}$ and 2.110 $cm^3\ g^{-1}$) (Bommier et al., 2015), and self-activation of kenaf core (2432 $m^2\ g^{-1}$ and 1.876 $cm^3\ g^{-1}$) (Xia and Shi, 2016a). The noticeably high SSA and SPV of the as-prepared activated carbon shows good electrochemical performance leading to high specific capacity of 384 mAh g^{-1} at 1C, which is higher than those of other reported carbon-based anodes (i.e. carbon nanotubes, graphites) (Chen et al., 2007; Chew et al., 2009; Jeong et al., 2013; Li et al., 2012; Novák et al., 2009; Sharifi et al., 2015). The unique fabrication method of the activated carbon-based anode may open up new fields for the development of next-generation, high-performance LIBs.

4.2 Experimental

4.2.1 Self-Activation Process

Self-activation process was carried out in a high-temperature vacuum box furnace (STY−1600C, Sentro Tech Corp., USA), with a vacuum system (ultimate pressure: 2 mmHg) and a maximum temperature of 1,600°C. The heating chamber had a dimension of 254 mm × 254 mm × 305 mm, which was made of alumina ceramic. Pine wood blocks with appoximate dimensions of 20 mm^3 were introduced as a raw material. The pine wood taken for this study had a 7.0 ± 0.1% moisture content in accordance with ASTM (American Society for Testing and Materials) D4442 standard. From the proximate and ultimate analysis, pine wood contains 0.9 ± 0.1% ash content, 43.8 ± 0.5% cellulose, 19.8 ± 0.3% hemicellulose, and 24.3 ± 2.1% lignin; these components are mainly comprised of elemental carbon (45.7 ± 0.1%), hydrogen (6.5 ± 0.1%), and oxygen (45.5 ± 0.1%) (Thangalazhy-Gopakumar et al., 2011).

The self-activation process was performed in three steps: 1) Placing 200 g wooden blocks into the vacuum box furnace chamber; 2) Pumping down the furnace to a pressure of 40 ± 1 Torr (94.7% vacuum) (the valves of the furnace were then turned off to create a closed system so that no matter is exchanged with the surroundings, during the pyrolysis process); and 3) Conducting the self-activation process by following three stages: a) ramping the temperature of the furnace to 1050°C with an heating rate of 10°C min^{-1}; b) dwelling at 1050°C for 2, 4, 8, 16, and 32 hours; and c) cooling down (rate < 10°C min^{-1}) to room temperature. The as-produced activated carbon was taken from the furnace and then pulverized by an ultra-fine pulverizing machine to obtain fine powders (RT-UF26, Rong Tsong Precision Technology Co., Taiwan).

4.2.2 Microstructure Analysis

The adsorption capabilities of activated carbons were determined by nitrogen adsorption at 77 K with a surface area and pore size analyzer (3Flex 3500, Micromeritics Instrument Corp., USA). The samples were degassed in vacuum at 350°C for 3-5 days using a degasser (Vac Prep 061, Micromeritics Instrument Corp., USA) followed by *in-situ* degassing in high vacuum (~10^{-5} Torr or lower) at 350°C for 20 h prior to the analysis. The Brunauer-Emmett-Teller (BET) method was used for the SSA analysis, and Density Functional Theory (DFT) was used for the SPV and pore size distribution studies.

4.2.3 XRD and Raman Analyses

The X-ray diffraction (XRD) analysis was carried out with an XRD-6000 meter (Shimadzu, Japan, Cu Kα radiation, λ = 1.54060Å), operating at 40 kV and 40 mA. The samples were scanned in the continuous scanning mode with the 2θ ranging from 10° to 50° at a scan rate of 2° min^{-1}, where θ was the incident angle of the X-ray beam onto the sample. Raman spectroscopy studies were performed in the range of 1000 – 2000 cm^{-1} using 532 nm continuous wave as the excitation source (Almega XR).

4.2.4 SEM and TEM Observation

The morphology of the as-prepared activated carbon was analyzed by scanning electron microscopy (SEM) and transmission electron microscopy (TEM). A Quanta 200 environmental SEM with an accelerating voltage of 15 kV was used to observe the specimens. An FEI Tecnai™ transmission electron microscopy (TEM) was

employed to identify the nanoscale porous structures and arrangement of graphene layers in the activated carbon.

4.2.5 Electrochemical Performance

The LIB anode based on activated carbon was prepared through the following key steps: (1) Activated carbon (75 wt%) and polyvinylidene difluoride (PVDF) (25 wt%) binder were dissolved into *N*-Methyl-2-pyrrolidone (NMP) solvent; (2) After sonication for 40 min., the mixture was uniformly cast by using a doctor blade onto a three-layered compressed Cu-mesh (> 99% purity, TWP Inc.) and was uniformly spread; (3) The cast mixture was subsequently heated at 80°C under a vacuum pressure of ~0 Torr in a drying oven to completely evaporate the NMP solvent. The activated carbon on Cu-mesh served as a working electrode and was integrated into a coin cell (CR 2032, Wellcos Ltd.) in an argon-filled glove box (MBraun) under extremely low levels of humidity and oxygen (< 0.5 ppm). The Li discs serve as counter and reference electrodes. 1 M solution of lithium hexafluorophosphate ($LiPF_6$) salt in 1:1:1 (volume ratio) mixture solvent of ethylene carbonate (EC), dimethylene carbonate (DMC), and diethylene carbonate (DEC) (MTI Corp.) was employed as an electrolyte. A typical polypropylene (PP)-based membrane (Separator-2400, Wellcos Ltd.) was used as a separator. The cell was finally assembled using a CR 2032 coin-cell crimping tool (Hohsen Corp.). The charge (delithiation) and discharge (lithiation) cycling tests were performed in a multi-channel battery testing unit (MACCOR-series 4000) at room temperature in the voltage window of 0.01-3.0V. The electrochemical impedance spectroscopy (EIS) measurement for the activated carbon-based anode was performed

before and after 31st cycle in a frequency range from 0.01 Hz to 10^6 Hz using a potentiostat (Reference 3000, Gamry Instrument). The perturbation amplitude was set as ±5 mV, and ten points per decade were collected. The impedance data of real and imaginary parts were plotted as a function of frequency in a complex plane diagram (Nyquist plot) and were fitted using a software (Echem Analyst™, Gamry Instrument).

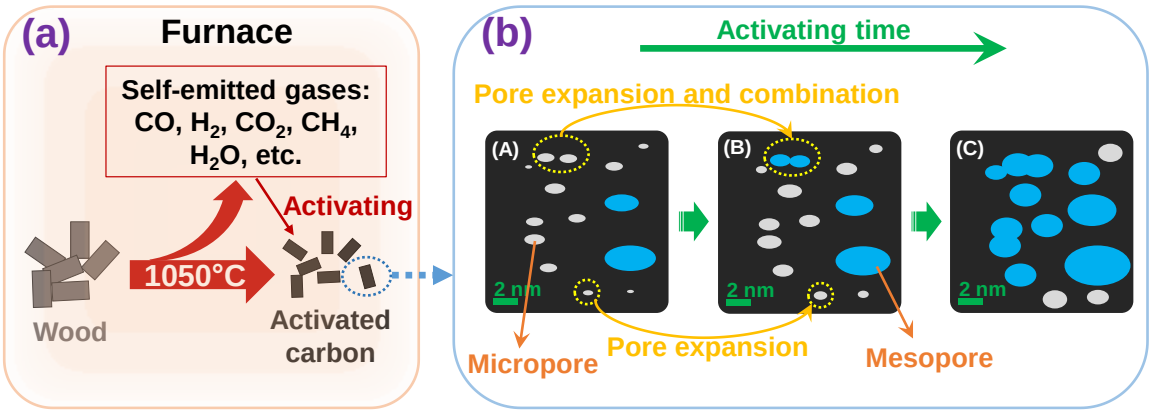

Figure 4.1 Illustrations of (a) self-activation process, and (b) changes of pores with the increasing of activating time.

4.3 Results and Discussion

4.3.1 BET Surface Area and Pore Volume of Activated Carbon

The illusion of self-activation process is presented in Figure 4.1a. Two products are extracted, including activated carbon and self-emitted gases. Moreover, the self-emitted gases are able to service as activating agents for the activation. The effect of dwelling time for self-activation on SSA and SPV is evident from the N_2 adsorption measurements of the as-prepared activated carbon (Figure 4.2 and Table 4.1). From the isothermal plots (Figure 4.2a), the adsorption of N_2 steadily increases, when the dwelling time for self-activation increases from 2 h to 4 h, 8 h, 16 h and 32 h. As a

result, SSA increases from 692 m^2 g^{-1} to 968 m^2 g^{-1}, 1838 m^2 g^{-1}, 2633 m^2 g^{-1}, and 2738 m^2 g^{-1}, respectively (Table 4.1). However, after comparing these values, it is observed that the SSA saturates after 16 h, reaching a maximum value of 2738 m^2 g^{-1} at dwelling time of 32 h. This similar trend was found in our earlier study on self-activation of kenaf core (Xia and Shi, 2016a). The SSA of kenaf core-based activated carbon reaches about 2400 m^2 g^{-1} after the pyrolysis for 15 h at a temperature of 1000°C. An activation model, with physical parameters including pore expansion (pore becomes bigger) and combination (two or more pores merge into one), is developed and the variation of SSA with dwelling time is well investigated (Xia and Shi, 2016a). Figure 4.1b presents the pore expansion and pore combination with the increase of activating time. In this activation model, SSA is increased by 114.1% during the pore expansion, but decreased by 7.7% at the pore combination. From the experimental data of the self-activation of kenaf core (Xia and Shi, 2016a), it is found that the pore expansion dominates in the early stage of the pyrolysis process (Figure 4.1b), the pore combination increases as the pyrolysis process continues, and eventually, the residual activated carbon would be converted into ash because of the pore combination.

The pore size distribution and SPV using DFT model are shown in Figure 4.2b and Table 4.1, respectively. The SPV of micropore ($SPV_{micropore}$) increases (0.282 cm^3 g^{-1}, 0.388 cm^3 g^{-1}, and 0.591 cm^3 $g^{-}1$) as the dwelling time increases (2, 4, and 8h). However, beyond dwelling time of 8h, the SPV decreases (from 0.485 cm^3 g^{-1}: 16h and 0.359 cm^3 g^{-1}:32h), which could be ascribed to the dominance of expansion of micropore (< 2 nm) over mesopores (2-50 nm; defined by IUPAC (International Union of Pure and Applied Chemists)) with the dwelling time (Xia and Shi, 2016a). Accordingly,

SPV of mesopore ($SPV_{mesopore}$) increases from 0.049 cm^3 g^{-1} to 1.838 cm^3 g^{-1} with the increase of dwelling time from 2 h to 32 h. In comparison, SPV of macropore ($SPV_{macropore}$) presents relatively small volume between 0.003 cm^3 g^{-1} and 0.013 cm^3 g^{-1} within these dwelling times. Therefore, the total SPV (SPV_{total}) increases from 0.334 cm^3 g^{-1}, to 2.209 cm^3 g^{-1}, when the dwelling time increases from 2 h to 32 h. The increase of $SPV_{mesopore}$ and SPV_{total} are contributed to the pore expansion during the activation process (Xia and Shi, 2016a). Figure 4.1b clearly shows the changes of pore volumes. SPVmicropore increases at the beginning (A to B in Figure 4.1b) and then decreases (B to C in Figure 4.1b), however, SPVmesopore increases in the whole process (A to C in Figure 4.1b).

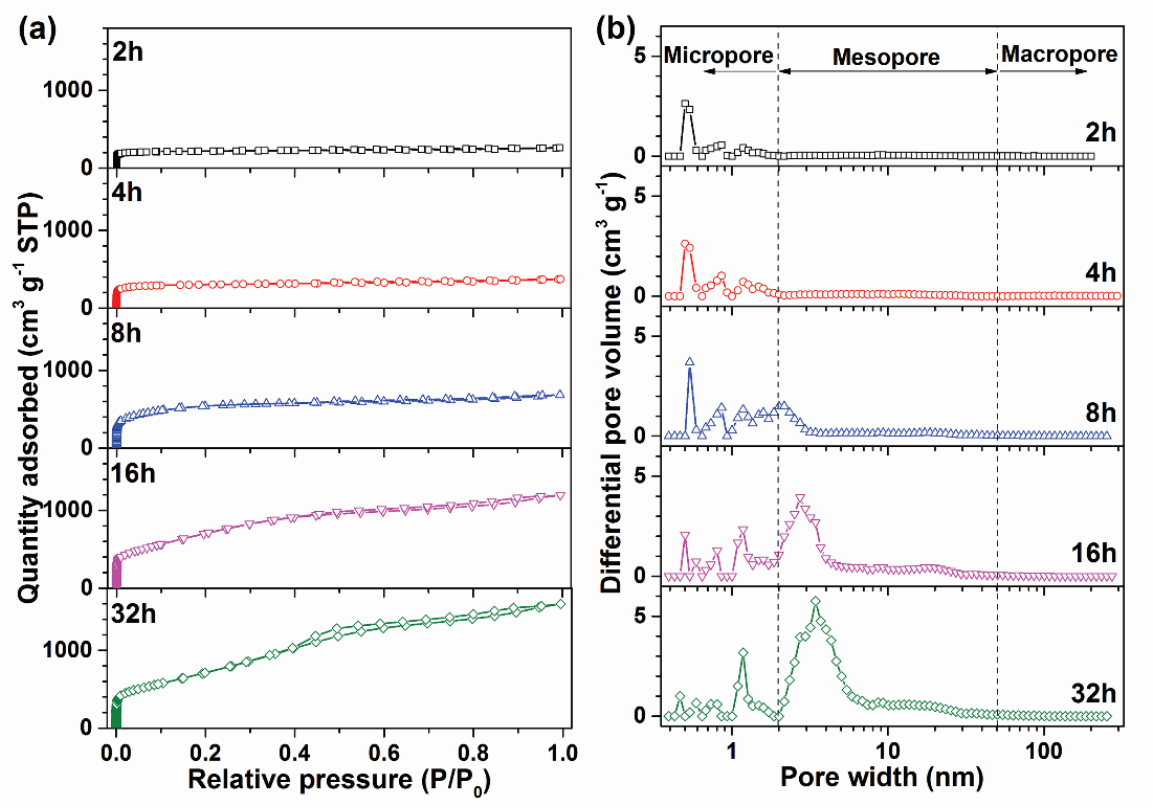

Figure 4.2 Isothermal plots (a) and DFT pore size distributions (b) of the activated carbon products through self-activation process at 1050°C with different dwelling times.

Table 4.1 Results of specific surface area and pore volume of the activated carbon products through self-activation process at 1050°C with different dwelling times.

Dwelling time	Yield	SSA_{BET} [a]	SPV_{DFT} [b] ($cm^3\ g^{-1}$)			
(h)	(%)	($m^2\ g^{-1}$)	Micropore (<2 nm)	Mesopore (2-50 nm)	Macropore (>50 nm)	Total
2	17.5	692	0.282	0.049	0.003	0.334
4	14.5	968	0.388	0.099	0.013	0.500
8	11.6	1838	0.591	0.305	0.005	0.902
16	7.3	2633	0.485	1.131	0.011	1.627
32	5.6	2738	0.359	1.838	0.012	2.209

[a] *SSA* = specific surface area by BET method;
[b] SPV_{DFT} = specific pore volume by DFT.

4.3.2 Structural and Morphological Properties of Activated Carbon

Besides the surface area and pore size analyses, the as-prepared activated carbon are further structurally characterized by XRD and Raman (Figure 4.3). The XRD patterns of as-prepared activated carbon are shown in Figure 4.3a. Two characteristic peaks of the sample are located at the 2θ of around 23° and 43°, corresponding to the (002) and (100) planes, respectively (Bommier et al., 2015). The broad peaks reveal that the activated carbon is assembled by defective graphene layers (Marsh and Reinoso, 2006). The degrees of the order of nano-domains along the c-axis were analyzed by empirical parameter (R), which was defined by Liu et al. (1996), i.e. measuring a ratio of (002) peak intensity compared to the background at the same diffraction angle (Figure 4.4). The R of the produced activated carbon decreases from 1.92 to 1.00 with the increase in dwelling time for self-activation process from 2 to 32 h. The R value is lower, the more disordered structure was developed. From these results, the activated carbon with high SSA owns a low R value. This could be attributed to a large number of nano-pores. Accordingly, the nanoscale morphology of as-prepared activated carbon by self-activation process becomes more disordered with the longer

dwelling time leading to the higher SSA, which is consistent with the recent reports (Bommier et al., 2015; Karthikeyan et al., 2014). For LIB application, the nano-porosity structure provides free-interlayer voids, which is beneficial for the facile Li^+ ion transport and can offer more electrochemically active sites (Inagaki et al., 2010; Pandolfo and Hollenkamp, 2006). Furthermore, the Raman peaks in Figure 4.3(b) around 1335 cm^{-1} (D-band) and 1590 cm^{-1} (G-band) correspond to the diamond (sp^3) and graphitic (sp^2) structures (Hou et al., 2015). The I_G/I_D values of the activated carbons are calculated in Figure 4.5, i.e. 0.55 – 0.65 for the produced activated carbons (Figure 4.3b). These results confirm that the microstructure of activated carbon is composed of sp^2-carbons containing vacancies and other symmetry-breaking defects (Dresselhaus et al., 2002).

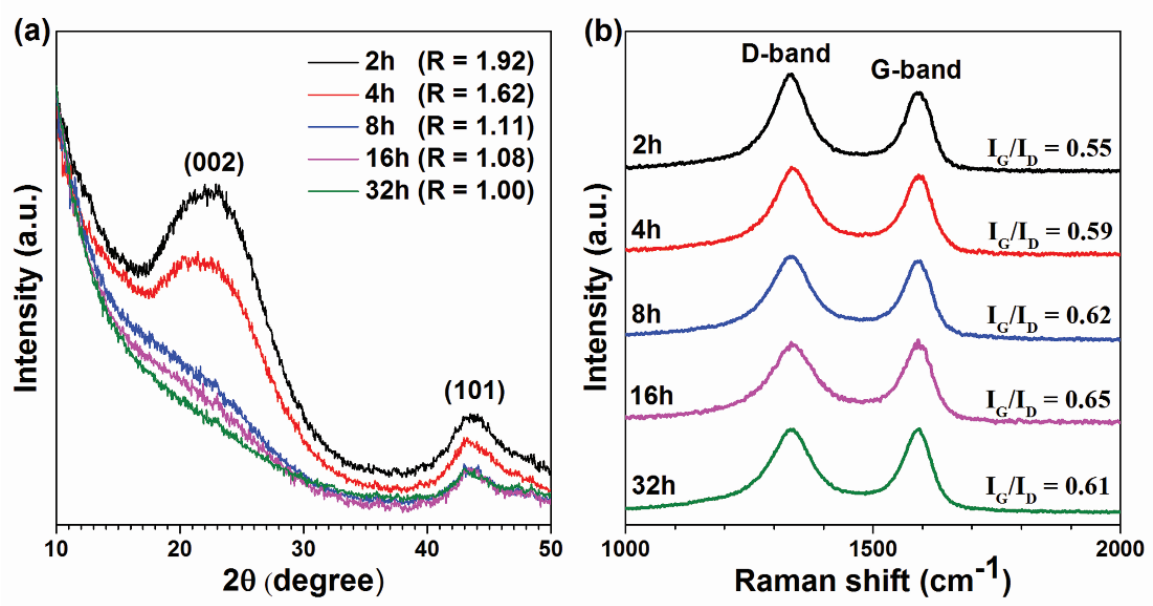

Figure 4.3 XRD patterns (a) and Raman spectra (b) of the activated carbon products through self-activation process at 1050°C with different dwelling times.

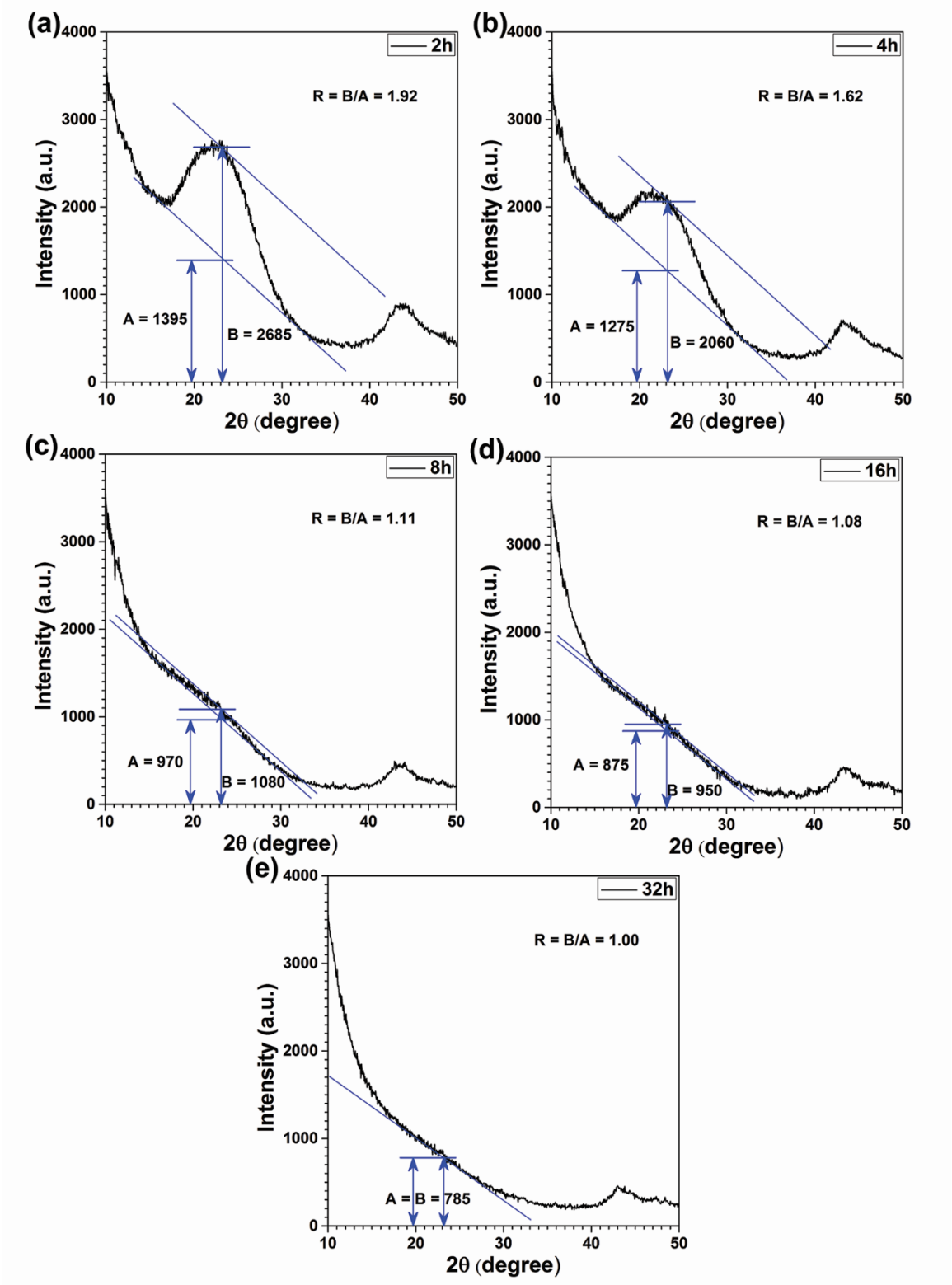

Figure 4.4 XRD patterns of the activated carbon products through self-activation process at 1050°C for 2 h (a), 4 h (b), 8 h (c), 16 h (d), and 32 h (e), respectively.

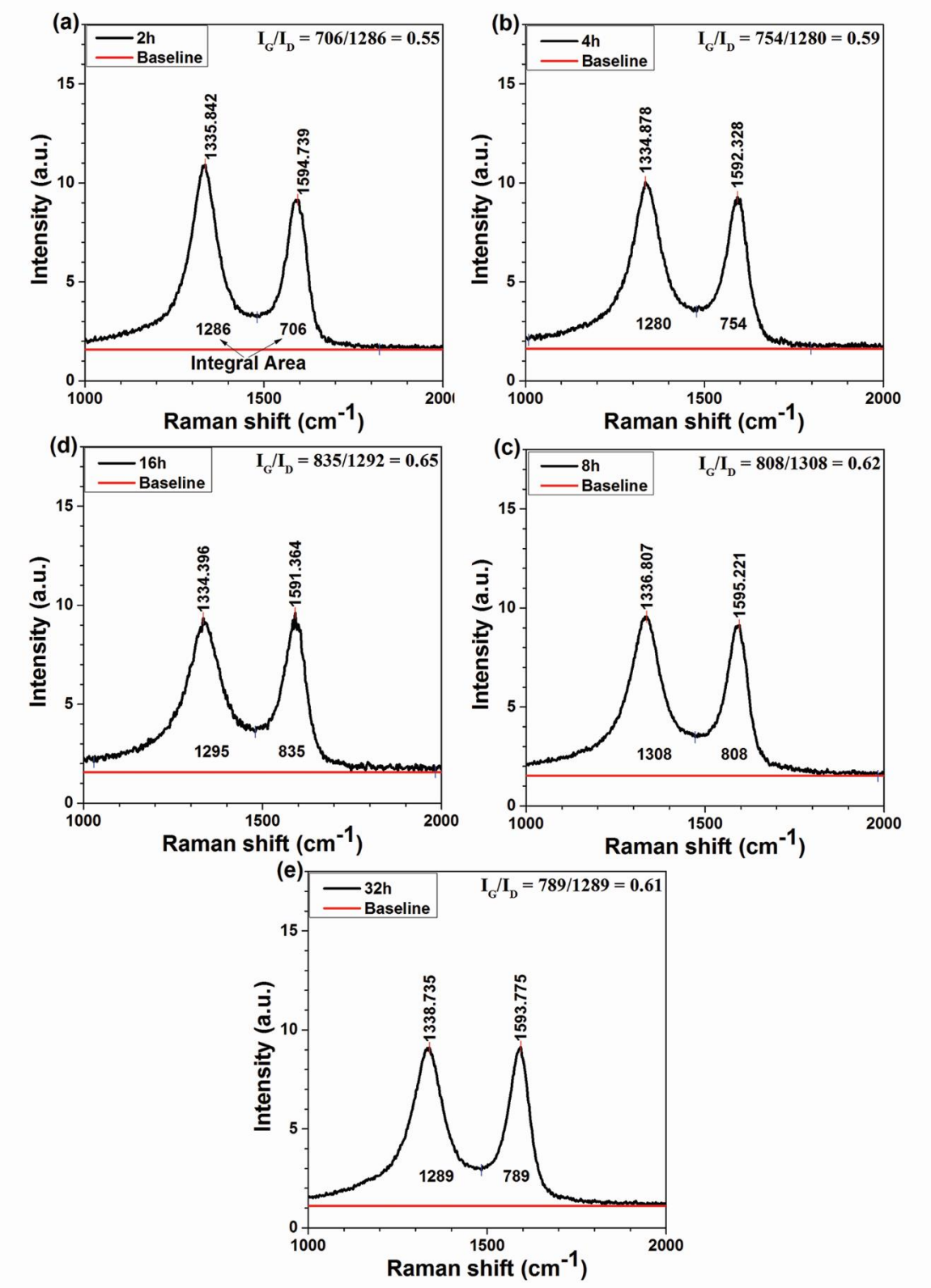

Figure 4.5 Raman spectra of the activated carbon products through self-activation process at 1050°C for 2 h (a), 4 h (b), 8 h (c), 16 h (d), and 32 h (e), respectively.

The SEM images show longitudinally and transversely fractured surfaces of a carbonized pine wood through self-activation process for 32 h, respectively. (Figure 4.6a,b). In Figure 4.6b, the SEM image demonstrates that the microscale honeycomb-like structure of the activated carbon stems from the inherent cells of the wood (Jebrane et al., 2015; Olsson et al., 2015). For a better utilization of high surface area and nano-pores of activated carbon, the materials are grinded into the microscale particulate structure as seen in Figure 4.6c.

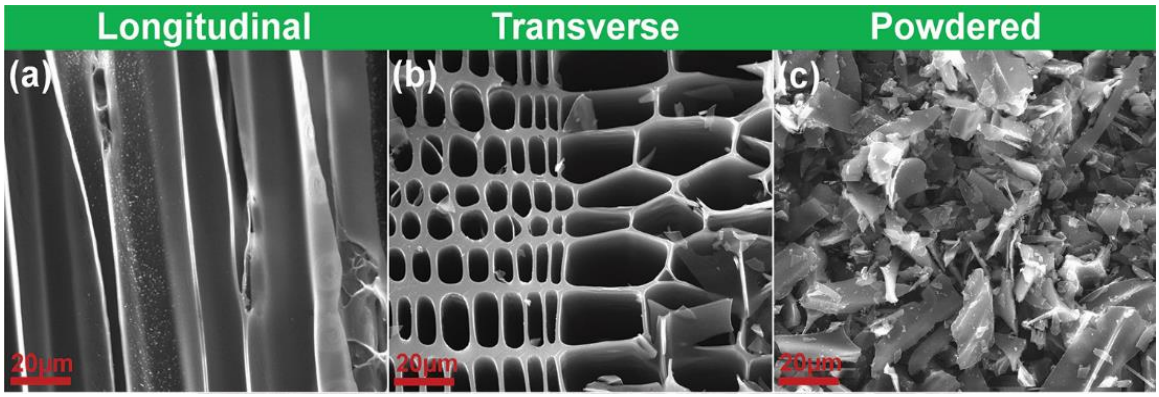

Figure 4.6 SEM images of tangential longitudinal (a) and transverse (b) sections of pine wood-derived activated carbon through self-activation process for 32 h, and its powdered activated carbon (c).

TEM images shown in Figure 4.7a reveal the nanoporous structures of activated carbon. Furthermore, the selective area diffraction pattern (SADP) (inset of Figure 4.7a) shows the broad widths and no speckle in the rings, indicating the amorphous structure of the activated carbon as verified from the XRD results (Figure 4.3a). Figure 4.7b and Figure 4.7c,d manifest characteristic hierarchical porous structures of micro- (<2 nm) and mesopore (2-50 nm) (i.e. dark spots in yellow circles) in contrast to defective carbon (i.e. white spots), respectively, justifying the porosity analysis as illustrated from

Figure 4.2 and Table 4.1 (Williams and Carter, 1996). The unique structures of the hierarchical nanoscale pores serve as abundant electroactive sites for Li^+ ions during the charge and discharge LIB cycling process (Marsh and Reinoso, 2006).

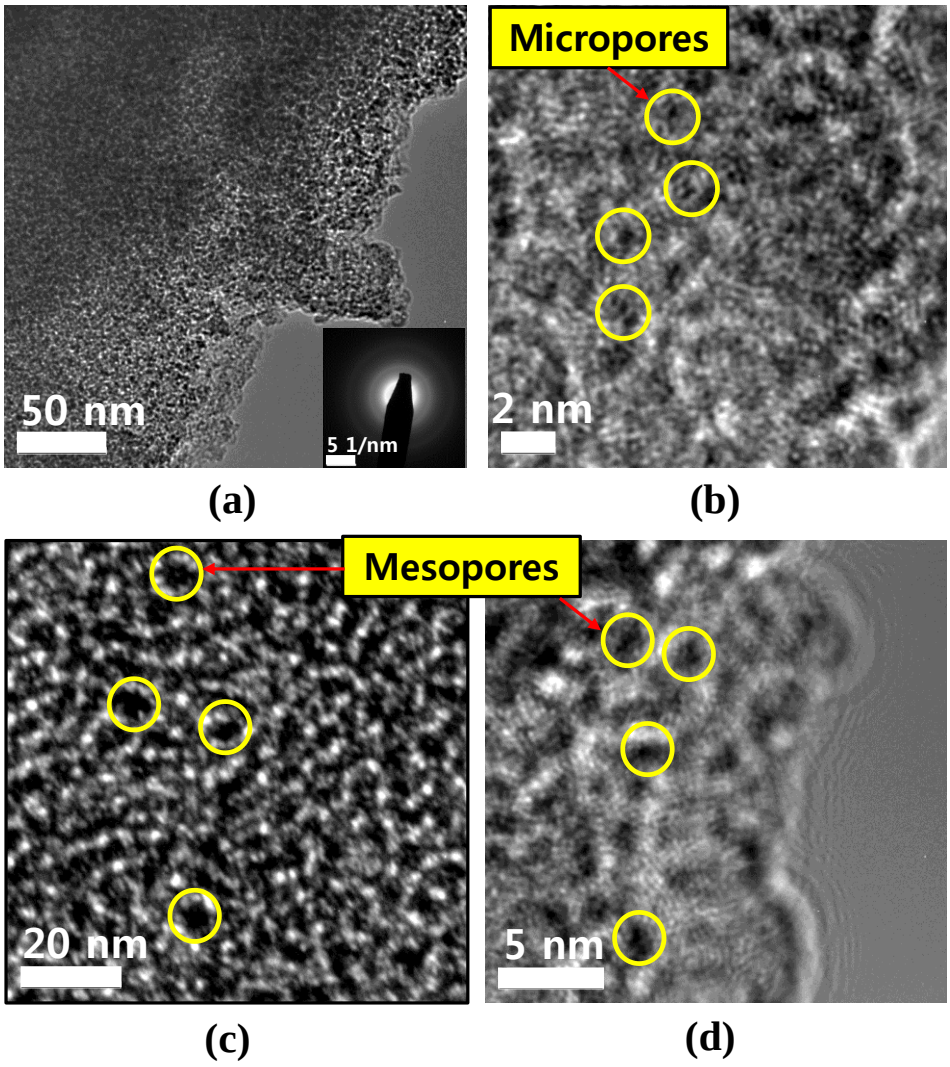

Figure 4.7 A low magnification TEM image of activated carbon with nanoscale porous structures (a); the higher magnification HRTEM image showing micropores (<2 nm) in the activated carbon (b); and the lower magnification HRTEM images exhibiting mesopores (2-50 nm) (c)-(d).

Also, the HRTEM image in Figure 4.7d shows that activated carbon is constituted of the low ordered 4-5 layered graphene sheets with an overall thickness of 2 nm and the corresponding layer-to-layer distance of ~0.36 nm (cf. 0.335 nm for graphite), similar to the previously reported activated carbon (Hou et al., 2015). The graphene sheets provide the high surface area for the accommodation of a large amount of Li^+ ions in conjunction with their exceptional electrical conductivity and excellent structural flexibility during insertion/extraction of Li^+ ions, which is favorable for enhanced LIB performance (Wu et al., 2011).

4.3.3 Li-Ion Battery Performance of Activated Carbon Anode

To evaluate the electrochemical performance of the activated carbon as anode material, Galvanostatic (constant current density) charge/discharge cycle performance is conducted in the voltage range of 0.01-3V at different C-rates. In Figure 4.8a, the first and second charge/discharge cycles result in the non-linear voltage profiles as a function of specific capacities. These characteristic profiles can be attributed to highly defective activated carbon structure as illustrated in Figure 4.3 and Figure 4.6d-e. The activated carbon structure possesses a wide range of electroactive sites with different energies for the lithiation/delithiation of lithium ions (Huggins, 2008). The first discharge voltage profile shows a clear plateau in the voltage range of 0.8−1V, which is closely related to the solid electrolyte interphase (SEI) layer formation on the surface of activated carbon by electrolyte decomposition. The SEI formation is observed in most carbon-based anode materials including graphite, carbon nanotubes, and activated carbon (de las Casas and Li, 2012; Hou et al., 2015; Winter et al., 2003). The first

charge and discharge capacities are 2070 mAh g^{-1} and 835 mAh g^{-1}, respectively. The charge capacity is about 224% higher than the theoretical capacity of graphite. Such enhancement is mainly due to its exceptionally high SSA and SPV as evident from Figure 4.2 and Table 4.1 (Hou et al., 2015). The high SSA and SPV in activated carbon provide large number of electroactive sites (e.g. hierarchical pores, defects, randomly oriented graphene layers) for Li^+ ions during charge/discharge processes; therefore, the higher specific capacity is obtained. The similar mechanism was reported by other groups (Inaba et al., 1996; Mabuchi et al., 1995). From Figure 4.8b, the reversible capacity at 1C gradually decreases from 387 $mAhg^{-1}$ at the first cycle to 258 $mAhg^{-1}$ at the 20^{th} cycle and then increases to 384 $mAhg^{-1}$ up to the 200^{th} cycles. The increasing trend shown in the range of 20^{th} to 200^{th} cycles could be due to the reactivated hierarchical porous nanostructure of the activated carbon (Hou et al., 2015). Moreover, the high structural integrity of activated carbon can be manifested by good capacity retention (~99%) with almost no loss up to 200 cycles. The reversible specific capacity is in the range of 258-391 mAh g^{-1}, which is superior to those of the recently reported carbon nanotubes (Sharifi et al., 2015) and porous graphite (Jeong et al., 2013). The high capacity could be attributed to exceptionally large SSA and SPV of activated carbon, providing larger electrode/electrolyte interfaces for facilitated charge transfer and porous nanostructures for shorter Li^+ ions diffusion length (Qie et al., 2012). Furthermore, the Coulombic efficiency of the activated carbon is higher than 90% after the initial 6 cycles at 1C and then increases up to 97-99% after the 20th cycle as presented in Figure 4.8c, suggesting a high reversibility of charge-discharge capacity.

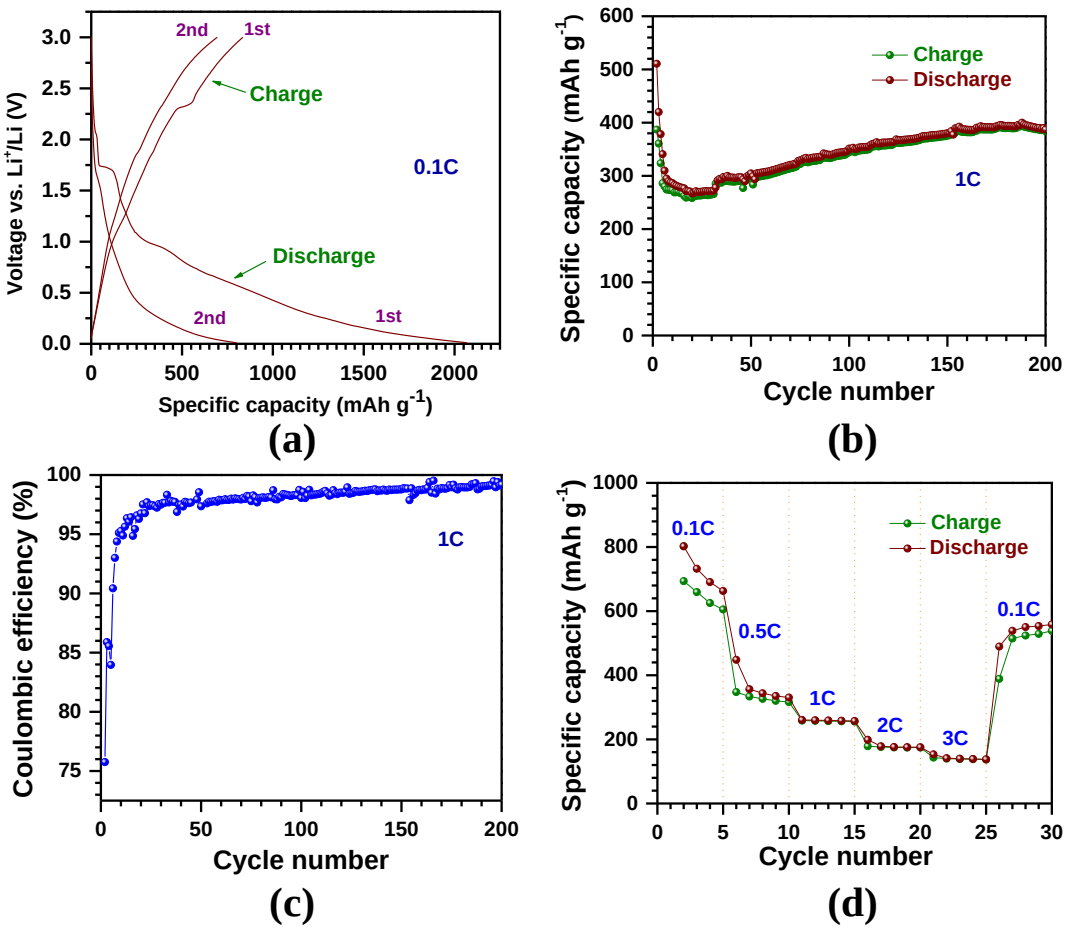

Figure 4.8 Electrochemical performance of the activated carbon anode. (a) Voltage profiles with specific capacity at the initial two charge-discharge cycles at 0.1C, (b) The cycling performance at 1C up to 200 cycles, (c) Coulombic efficiency for charge-discharge capacity reversibility at 1C up to 200 cycles, (d) The variation of specific capacities with different C-rates.

In addition, Figure 4.8d illustrates the variation of reversible capacities with the different C-rates. At 0.1C, 0.5C, 1C, 2C, and 3C, the average reversible capacities are 646 mAh g^{-1}, 329 mAh g^{-1}, 257 mAh g^{-1}, 176 mAh g^{-1}, and 139 mAh g^{-1}, respectively. The overall reversible capacities obtained from the different C-rates are higher than those of commercially available graphitized mesocarbons (Novák et al., 2009), free-standing CNTs (Chew et al., 2009; Li et al., 2012), and the vertically aligned

CNTs/conducting polymer composite (Chen et al., 2007). Importantly, the capacity at 0.1C after the C-rate test up to 3C recovers to an initial capacity of ~499 mAh g^{-1}, indicating the well-preserved structural integrity of activated carbon during cycling. Considering the high capacities, self-activation method for the fabrication of activated carbon can be a promising approach to design large-scale synthesis of anode material for next-generation LIBs.

4.3.4 EIS Study of Activated Carbon Anode

EIS analysis is carried out in the frequency range of 0.01 Hz to 10^6 Hz with a perturbation voltage of 5 mV. Figure 4.9 shows the Nyquist plot of the activated carbon before and after 31 cycles, along with the corresponding models for each condition. It is clearly visible that the impedance spectra before cycling has only one semicircle in the high to medium frequency range with R_e and R_{ct} values of 4.5 and 118 ohm. After 31 cycles, the impedance spectra show the emerging semicircle in the medium frequency range, corresponding to the formation of the SEI film on the electrode during cycling. The electrolyte (R_e), charge transfer (R_{ct}), and SEI film resistance (R_s) of the impedance spectra after 31 cycles are 5, 345, and 395 ohm, respectively. The linear slope in low frequency region is related to solid state diffusion of Li^+ ions into the electrode.

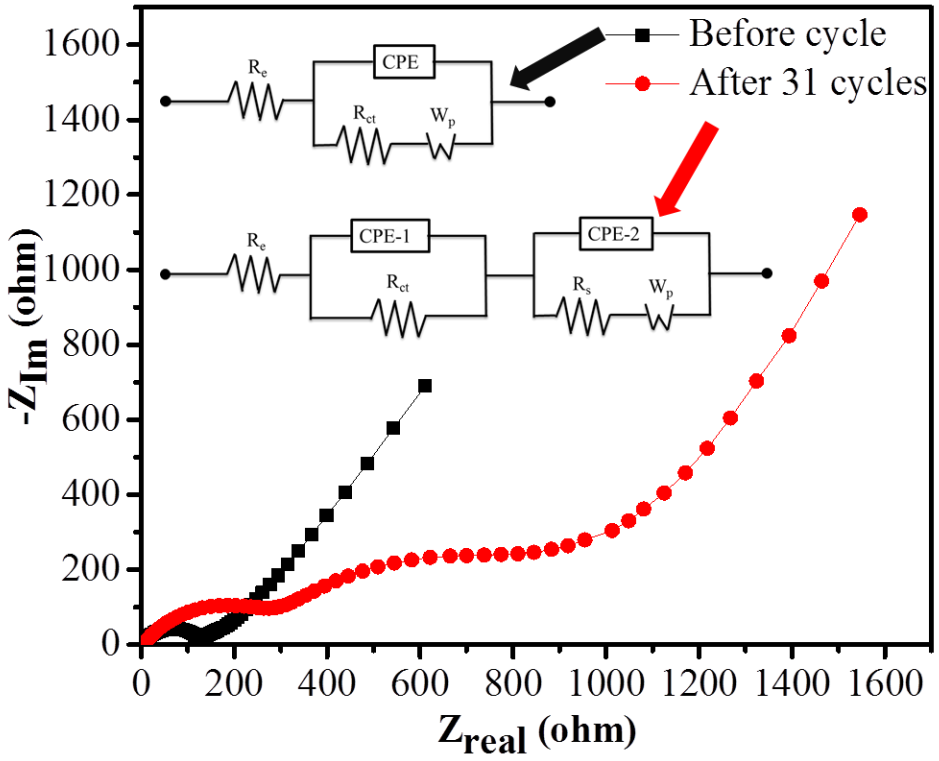

Figure 4.9. Nyquist plot of activated carbon before and after 31 cycles, measured in the frequency range of 10^6-0.01Hz.

4.4 Conclusions

In summary, an unprecedented approach was designed to fabricate large-scale activated carbon by an environmentally benign and efficient self-activation process that employs no additional oxidizing/inert gases or chemical reagents. The as-prepared activated carbon tailored by dwelling conditions yields exceptionally high SSA and SPV up to 2738 $m^2\ g^{-1}$ and 2.209 $cm^3\ g^{-1}$, respectively, which are superior to other activated carbons synthesized by conventional physical/thermal and chemical activation processes. Owing to the excellent physico-chemical properties offering a large number of electroactive sites, activated carbon was used as an anode material for LIBs. The outstanding electrochemical performance, including cycling stability up to 200 cycles

and high C-rate capability (till 3C) with a specific capacity of 646 mAh g^{-1} at 0.1C. These appealing results are much higher than those of commercially available graphite and lab-produced carbon nanotube anode materials. This novel self-activation process, integrated with good LIB performance, may offer a feasible way toward the advanced, large-scale and highly efficient synthesis for activated carbon-based anodes for LIBs.

4.5 References

Bommier, C., Xu, R., Wang, W., Wang, X., Wen, D., Lu, J., Ji, X., 2015. Self-activation of cellulose: A new preparation methodology for activated carbon electrodes in electrochemical capacitors, *Nano Energy*, 13, 709-717.

Chen, J., Liu, Y., Minett, A.I., Lynam, C., Wang, J., Wallace, G.G., 2007. Flexible, aligned carbon nanotube/conducting polymer electrodes for a lithium-ion battery, *Chemistry of Materials*, 19(15), 3595-3597.

Chew, S.Y., Ng, S.H., Wang, J., Novak, P., Krumeich, F., Chou, S.L., Chen, J., Liu, H.K., 2009. Flexible free-standing carbon nanotube films for model lithium-ion batteries, *Carbon*, 47(13), 2976-2983.

de las Casas, C., Li, W., 2012. A review of application of carbon nanotubes for lithium ion battery anode material, *Journal of Power Sources*, 208, 74-85.

Dresselhaus, M.S., Dresselhaus, G., Jorio, A., Souza, A.G., Saito, R., 2002. Raman spectroscopy on isolated single wall carbon nanotubes, *Carbon*, 40(12), 2043-2061.

Hou, J., Cao, C., Idrees, F., Ma, X., 2015. Hierarchical porous nitrogen-doped carbon nanosheets derived from silk for ultrahigh-capacity battery anodes and supercapacitors, *ACS Nano*, 9(3), 2556-2564.

Huggins, R., 2008. Negative Electrodes in Lithium Cells. In: Huggins, R. (Ed.), Advanced Batteries: Materials Science Aspects. Springer Science & Business Media, New York, pp. 134-135.

Inaba, M., Yoshida, H., Ogumi, Z., 1996. In situ Raman study of electrochemical lithium insertion into mesocarbon microbeads heat-treated at various temperature, *Journal of the Electrochemical Society*, 143(8), 2572-2578.

Inagaki, M., Konno, H., Tanaike, O., 2010. Carbon materials for electrochemical capacitors, *Journal of Power Sources*, 195(24), 7880-7903.

Jebrane, M., Fernandez-Cano, V., Panov, D., Terziev, N., Daniel, G., 2015. Novel hydrophobization of wood by epoxidized linseed oil. Part 2. Characterization by FTIR spectroscopy and SEM, and determination of mechanical properties and field test performance, *Holzforschung*, 69(2), 179-186.

Jeong, S., Lee, J., Ko, M., Kim, G., Park, S., Cho, J., 2013. Etched graphite with internally grown Si nanowires from pores as an anode for high density Li-ion batteries, *Nano Letters*, 13(7), 3403-3407.

Kang, C., Patel, M., Rangasamy, B., Jung, K., Xia, C., Shi, S., Choi, W., 2015. Three-dimensional carbon nanotubes for high capacity lithium-ion batteries, *Journal of Power Sources*, 299, 465-471.

Karthikeyan, K., Amaresh, S., Lee, S.N., Sun, X., Aravindan, V., Lee, Y., Lee, Y.S., 2014. Construction of high-energy-density supercapacitors from pine-cone-derived high-surface-area carbons, *ChemSusChem*, 7(5), 1435-1442.

Knox, S.H., Sturtevant, C., Matthes, J.H., Koteen, L., Verfaillie, J., Baldocchi, D., 2015. Agricultural peatland restoration: effects of land-use change on greenhouse gas (CO_2 and CH_4) fluxes in the Sacramento-San Joaquin Delta, *Global Change Biology*, 21(2), 750-765.

Li, X., Yang, J., Hu, Y., Wang, J., Li, Y., Cai, M., Li, R., Sun, X., 2012. Novel approach toward a binder-free and current collector-free anode configuration: highly flexible nanoporous carbon nanotube electrodes with strong mechanical strength harvesting improved lithium storage, *Journal of Materials Chemistry*, 22(36), 18847-18853.

Liu, Y.H., Xue, J.S., Zheng, T., Dahn, J.R., 1996. Mechanism of lithium insertion in hard carbons prepared by pyrolysis of epoxy resins, *Carbon*, 34(2), 193-200.

Lua, A.C., Yang, T., 2004. Effect of activation temperature on the textural and chemical properties of potassium hydroxide activated carbon prepared from pistachio-nut shell, *Journal of Colloid and Interface Science*, 274(2), 594-601.

Mabuchi, A., Tokumitsu, K., Fujimoto, H., Kasuh, T., 1995. Charge-discharge characteristics of the mesocarbon microbeads heat-treated at different temperatures, *Journal of the Electrochemical Society*, 142(4), 1041-1046.

Manthiram, A., 2003. Materials Aspects: An Overview. In: Nazri, G., Pistoia, G. (Eds.), Lithium Batteries: Science and Technology. Springer, New York, pp. 1-11.

Marsh, H., Reinoso, F.R., 2006. Activated Carbon, pp. 2, 375.

Mohan, D., Pittman Jr, C.U., 2006. Activated carbons and low cost adsorbents for remediation of tri-and hexavalent chromium from water, *Journal of Hazardous Materials*, 137(2), 762-811.

Novák, P., Goers, D., Spahr, M.E., 2009. Carbon Materials in Lithium-Ion Batteries. In: Béguin, F., Frackowiak, E. (Eds.), Carbons for Electrochemical Energy Storage and Conversion Systems. CRC Press, Boca Raton, pp. 300.

Olsson, S.K., Matsunaga, H., Kataoka, Y., Johansson, M., Matsumura, J., Westin, M., Ostmark, E., 2015. A SEM study on the use of epoxy functional vegetable oil and reactive UV-absorber as UV-protecting pretreatment for wood, *Polymer Degradation and Stability*, 113, 40-45.

Pandolfo, A.G., Hollenkamp, A.F., 2006. Carbon properties and their role in supercapacitors, *Journal of Power Sources*, 157(1), 11-27.

Qie, L., Chen, W., Wang, Z., Shao, Q., Li, X., Yuan, L., Hu, X., Zhang, W., Huang, Y., 2012. Nitrogen-doped porous carbon nanofiber webs as anodes for lithium ion batteries with a superhigh capacity and rate capability, *Advanced Materials*, 24(15), 2047-2050.

Rao, A.B., Rubin, E.S., 2002. A technical, economic, and environmental assessment of amine-based CO_2 capture technology for power plant greenhouse gas control, *Environmental Science & Technology*, 36(20), 4467-4475.

Sharifi, T., Valvo, M., Gracia-Espino, E., Sandstrom, R., Edstrom, K., Wagberg, T., 2015. Hierarchical self-assembled structures based on nitrogen-doped carbon nanotubes as advanced negative electrodes for Li-ion batteries and 3D microbatteries, *Journal of Power Sources*, 279, 581-592.

Shi, S.Q., Che, W., Liang, K., Xia, C., Zhang, D., 2015. Phase transitions of carbon-encapsulated iron oxide nanoparticles during the carbonization of cellulose at

various pyrolysis temperatures, *Journal of Analytical and Applied Pyrolysis*, 115, 1-6.

Shi, S.Q., Xia, C., 2014. Porositization process of carbon or carbonaceous materials, US patent 14/211,357.

Thangalazhy-Gopakumar, S., Adhikari, S., Gupta, R.B., Tu, M., Taylor, S., 2011. Production of hydrocarbon fuels from biomass using catalytic pyrolysis under helium and hydrogen environments, *Bioresource Technology*, 102(12), 6742-6749.

Williams, D.B., Carter, C.B., 1996. Indexing Diffraction Patterns. In: Williams, D.B., Carter, C.B. (Eds.), Transmission Electron Microscopy: A Textbook for Materials Science. Springer, New York, pp. 273-277.

Winter, M., Moeller, K., Besenhard, J., 2003. Carbonaceous and Graphitic Anodes. In: Nazri, G., Pistoia, G. (Eds.), Lithium Batteries. Springer, New York, pp. 145-194.

Wu, Z., Ren, W., Xu, L., Li, F., Cheng, H., 2011. Doped graphene sheets as anode materials with superhigh rate and large capacity for lithium ion batteries, *ACS Nano*, 5(7), 5463-5471.

Xia, C., Shi, S.Q., 2015. Self-activation process for biomass based activated carbon, *Proceedings of 58th International Convention of Society of Wood Science and Technology (SWST)*, 2015, 98-104.

Xia, C., Shi, S.Q., 2016a. Self-activation for activated carbon from biomass: theory and parameters, *Green Chemistry*, Accepted Manuscript, In Press, doi: 10.1039/C5GC02152A.

Xia, C., Shi, S.Q., 2016b. Self-activation process to fabricate activated carbon from kenaf, *Wood and Fiber Science*, 48, 62-69.

Yahya, M.A., Al-Qodah, Z., Ngah, C.W.Z., 2015. Agricultural bio-waste materials as potential sustainable precursors used for activated carbon production: A review, *Renewable & Sustainable Energy Reviews*, 46, 218-235.

Yang, H., Yan, R., Chen, H., Lee, D.H., Zheng, C., 2007. Characteristics of hemicellulose, cellulose and lignin pyrolysis, *Fuel*, 86(12-13), 1781-1788.

Zhang, T.Y., Walawender, W.P., Fan, L.T., Fan, M., Daugaard, D., Brown, R.C., 2004. Preparation of activated carbon from forest and agricultural residues through CO_2 activation, *Chemical Engineering Journal*, 105(1-2), 53-59.

Zhang, X., Ma, X., Wu, Y., Li, Y., 2015. Enhancement of farmland greenhouse gas emissions from leakage of stored CO_2: Simulation of leaked CO_2 from CCS, *Science of the Total Environment*, 518, 78-85.

CHAPTER 5

WATER CLEARING AND OIL ABSORPTION

5.1 Introduction

Activated carbon products have a number of distinctive characteristics, including large internal surface area, dedicated surface chemical properties, good accessibility of internal pores, etc. (Wikipedia, 2016). The specific surface area, dedicated chemical properties and pore size distribution are the indices to categorize the product grades and their application areas. The pore size can be sorted into three different categories based on International Union of Pure and Applied Chemistry (IUPAC) definitions: 1) macropore (> 50 nm), 2) mesopore (2-50 nm) and 3) micropore (≤ 2 nm). For the water purification applications based on the ANSI/AWWA (American National Standards Institute/American Water Works Association standard) B600-10 standard, the minimum specific surface area should be 500 m^2/g, while it can have a large range of the pore size distribution from micropore to macropore. For the activated carbon in air purification application, the requirements are much higher. The specific surface areas of most air purification activated carbons should be higher than 1,000 m^2/g, and the pore size distribution is in micropore level.

Recently, the market for the emergency oil spill can be huge for the activated carbon product. One significant example as a critical national need is that Deepwater Horizon oil spilled in the Gulf of Mexico in 2010, approximately 4.9 million barrels of oil was lost and contaminated the ocean, and the total cost was estimated as $63 billion (Corkery, 2010). Another one is the recent West Virginia chemical spill in January 2014,

which forced 300,000 West Virginians to shut down their taps for up to ten days costing their inconvenience and, for some, illness and suffering. It has incurred business cost of $61 million in January based on the preliminary economic impact study by Marshall University Center for Business and Economic Research (Hardcastle, 2014).

Self-activation process has been investigated and proofed to be a green way for high-performance activated carbon (Shi and Xia, 2014; Xia and Shi, 2016a; Xia and Shi, 2015; Xia and Shi, 2016b). The highest specific surface area and pore volume of self-activation of kenaf core, kenaf fiber, and pine wood are shown in Table 5.1. The activated carbons fabricated through self-activation process presented high specific surface areas and pore volumes (Table 5.1), which are comparable with that manufactured by the conventional activation processes (up to 1926 m^2 g^{-1} for the physical activation, and 1642 m^2 g^{-1} for the chemical activation) (Yahya et al., 2015). However, compared to the conventional activated carbon manufacturing, when the self-activation technology is used, it saves the cost of activating agents since no activating gas or chemical is needed. In addition, the self-activation process is more environmentally friendly.

Table 5.1 Specific surface areas and pore volumes from different biomass through self-activation process

Activated carbon	Specific surface area [a] (m^2 g^{-1})	Specific pore volume [b] (cm^3 g^{-1})
Kenaf core-derived	2,432	1.740
Kenaf fiber-derived	1,742	1.192
Pine wood-derived	2,738	2.209

[a] Brunauer–Emmett–Teller (BET) specific surface area;

[b] Density Functional Theory (DFT) specific pore volume.

Activated carbon owns excellent capabilities of water purification and oil absorption, because of its highly porous structure. In this section, these properties of the activated carbon from self-activation process were investigated.

5.2 Materials and Methods

5.2.1 Preparation of Powdered Activated Carbon

Four activated carbons were used in the tests. Three of them were kenaf core-based activated carbons and coded as PAC-I, PAC-II, and PAC-III. The last one was purchased from Calgon Carbon Corporation, USA, and marked as Calgon AC. Prior to the tests, all of four activated carbons were pulverized by an ultra-fine pulverizing machine (RT-UF26, Rong Tsong Precision Technology Co., Taiwan) to match the size requirement of powdered activated carbon (PAC) in accordance with the American National Standards Institute/American Water Works Association (ANSI/AWWA) B600-10 standard (not less than 99% of the activated carbon shall pass a No. 100 sieve, not less than 95% shall pass a No. 200 sieve, and not less than 90% shall pass a No. 325 sieve).

5.2.2 Specific Surface Area and Pore Volume

The N_2 gas adsorption capabilities of the PACs were determined by the nitrogen adsorption at 77 K with a surface area and pore size analyzer (3Flex 3500, Micromeritics Instrument Corp., USA). The samples were vacuum degassed at 350°C for 3–5 days using a degasser (VacPrep 061, Micromeritics Instrument Corp., USA), and then *in situ* degassed at 350°C for 20 hours by a turbo molecular drag pump

(EXT75DX 63CF, Edwards Limited, Crawley, West Sussex, UK). Specific surface areas were calculated from the isothermal plots through the instrumental software (3Flex Version 1.02, Micromeritics Instrument Corp., USA). The Brunauer–Emmett–Teller (BET) method was used for the specific surface area (SSA) analysis. The Dubinin-Radushkevich model was used for analyzing micropore (<2 nm) specific pore volume (SPV). The Barrett-Joyner-Halenda (BJH) method was employed for determining the meso-macropore (≥2 nm) volumes.

5.2.3 Iodine Number Determination

Iodine number is an important characteristic for the chemical absorption evaluation of activated carbon. The ANSI/AWWA B600-10 standard requires that the iodine number of PAC should be higher than 500 mg/g. The iodine numbers of the four PACs were determined in accordance with the ASTM D4607 standard.

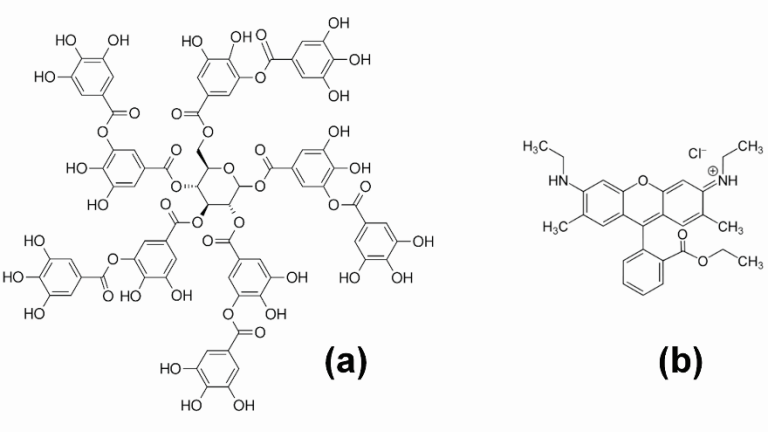

Figure 5.1 Chemical formulas of tannic acid (a) and rhodamine 6G (b) (from Wikipedia)

5.2.4 Tannin Value Test

The tannin value is defined as the concentration of activated carbon in milligrams per liter required to reduce the standard tannic acid (MP Biomedicals Corporation, USA) concentration from 20 mg/L to 2 mg/L. The chemical formula was presented in Figure 5.1a. Based on the AWWA B600-10 standard, the tests for tannin values of the four PACs were carried out.

Figure 5.2 Shimadzu UV-vis spectrophotometer.

5.2.5 Absorption of Copper (II)

Copper bromide ($CuBr_2$) (Sigma-Aldrich Corporation, USA) was used as targeting material for the Cu(II) absorption tests. For each test, 50 mg PAC was added into 200 mL $CuBr_2$ aqueous solution (200 mg L^{-1}). The mixture was stirred for 24 h, and then filtered to clarify the solution. The residual concentration of $CuBr_2$ aqueous solution

was determined by the UV-vis absorption in according with the Beer's Law. A UV-2600 UV-vis spectrophotometer (Shimadzu Corp., Japan) (Figure 5.2).

5.2.6 Rhodamine 6G Adsorption

Rhodamine 6G (Figure 5.1b) was purchased from Sigma-Aldrich Corporation, USA. The removal of Rhodamine 6G from water was carried out in accordance with the procedure from the literatures (Annadurai et al., 2001; Zhang et al., 2012). For each test, 50 mg PAC was mixed with 50 mL rhodamine 6G aqueous solution (400 μM L^{-1}). After 24 h stirring, the mixture was filtered to remove the solid. The residual concentration of Rhodamine 6G aqueous solution was determined by the UV-vis absorption.

5.2.7 Crude Oil Removal

Crude oil was dispersed into the water to prepare the saturated crude oil aqueous solution (~50mg L^{-1}). For each test, 100 mg PAC was mixed with 100 mL crude oil aqueous solution and stirred for 24 h. After that, the solid was filtered from the solution. The concentration of the solution was determined with the UV-vis spectrophotometer.

5.2.8 Absorption Capacity of Oil

The procedure described in Standard Method 5520F (Standard Method 5520F, 2001) was used for the oil absorption characterization. The oil absorption capacity of PAC-II and kenaf core was tested by the procedures shown in Figure 5.3.

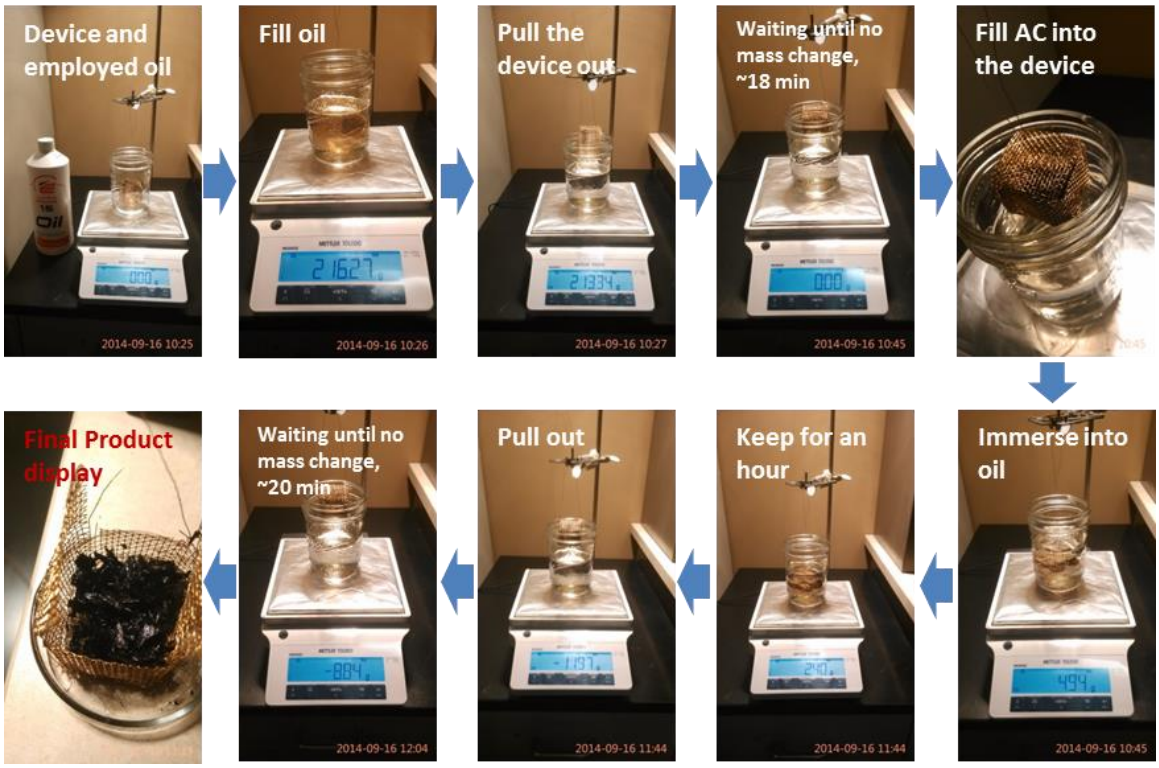

Figure 5.3 The procedures of oil absorption tests.

5.3 Results and Discussion

5.3.1 PAC Performance

5.3.1.1 Specific Surface Area and Pore Volume

Table 5.1 shows the SSA, $SPV_{micropore}$, and $SPV_{meso\text{-}macropore}$ results of the PACs. Three kenaf core-based PACs and a commercial activated carbon (Calgon AC) were selected for the comparison. These four PACs owned different/similar SSA, different/similar $SPV_{micropore}$, and different $SPV_{meso\text{-}macropore}$ of the structures (Table 5.1).

Table 5.2 Specific surface areas and pore volumes of the PACs.

Sample	SSA [a] ($m^2\ g^{-1}$)	$SPV_{micropore}$ [b] ($cm^3\ g^{-1}$)	$SPV_{meso\text{-}macropore}$ [c] ($cm^3\ g^{-1}$)
PAC-I	901	0.395	0.251
PAC-II	2266	0.783	0.805
PAC-III	2296	0.809	2.100
Calgon AC [d]	836	0.402	0.044

[a] Specific surface area, using Brunauer–Emmett–Teller (BET) method;

[b] Specific pore volume of micropore, from Density Functional Theory (DFT);

[c] Specific pore volume of meso-macropore in accordance with Dubinin-Radushkevich model;

[d] Commercial activated carbon from Calgon Carbon Corporation, USA.

5.3.1.2 Iodine Number

Carbons preferentially adsorb small molecules. The iodine number is a fundamental parameter used to characterize the activated carbon mainly for the micropore sizes up to 2 nm through measuring the adsorption ability of iodine from the liquid solution. The iodine number is defined as the amount of iodine adsorbed by 1 g carbon at the mg level. The minimum iodine number requirement of PAC for drinking-water cleaning is 500 mg g^{-1} based on the ANSI/AWWA B600-10 standard. In Figure 5.4, it is presented that PAC-III has the highest iodine number (2120 mg g^{-1}), and the iodine numbers of PAC-II (2040 mg g^{-1}) Calgon AC (1053 mg g^{-1}) and PAC-I (952 mg g^{-1}) are decreased systematically, which are fully corresponding to the order of $SPV_{micropore}$ values (Table 5.1) of the PAC-III (0.809 $cm^3\ g^{-1}$), PAC-II (0.783 $cm^3\ g^{-1}$), Calgon AC (0.402 $cm^3\ g^{-1}$), and PAC-I (0.395 $cm^3\ g^{-1}$). It indicates that the iodine as a small molecular prefers to be absorbed by the micropore of activated carbon.

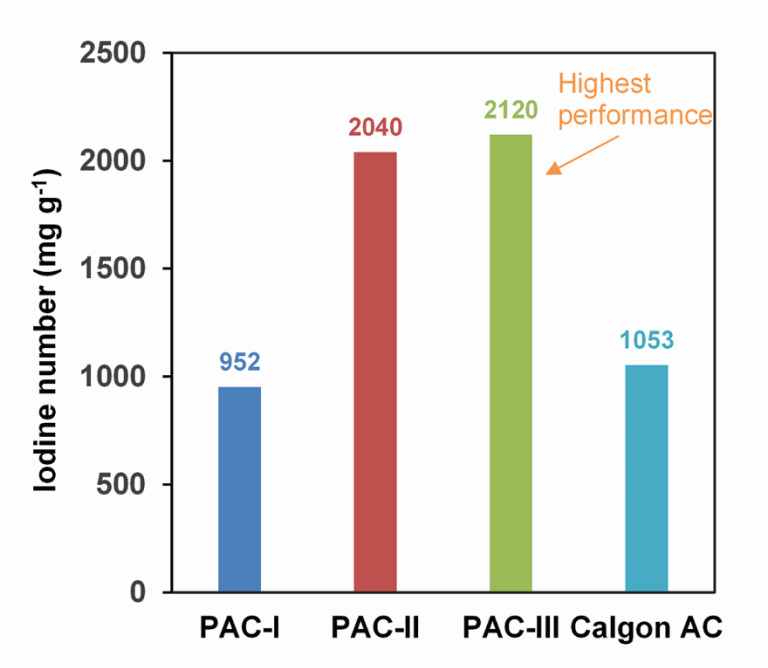

Figure 5.4 Iodine numbers of the PACs.

5.3.1.3 Tannin Value

Tannin value test is another performance-based evaluation test item described in the ANSI/AWWA B600-10 standard. The tannin value is an index of PAC's ability to remove high molecular weight impurities, such as organic compounds in the water by decayed vegetation. Tannin value is defined as the concentration of PAC requires to reduce the standard tannic acid (Figure 5.1a) concentration from 20 mg L^{-1} to 2 mg L^{-1} (90% removed of tannic acid from 20 mg/L standard tannic acid/water solution). Figure 5.5 shows the tannin values of the PAC-I (469 mg L^{-1}), PAC-II (266 mg L^{-1}), PAC-III (103 mg L^{-1}), and Calgon AC (633 mg L^{-1}). The lower tannin value means the less PAC is needed for removing 90% tannic acid from 20 mg L^{-1} tannic acid solution. The results are fully consistent with the $SPV_{meso\text{-}macropore}$ values of PACs (Table 5.1), i.e. higher $SPV_{meso\text{-}macropore}$ of the PAC has lower tannin value.

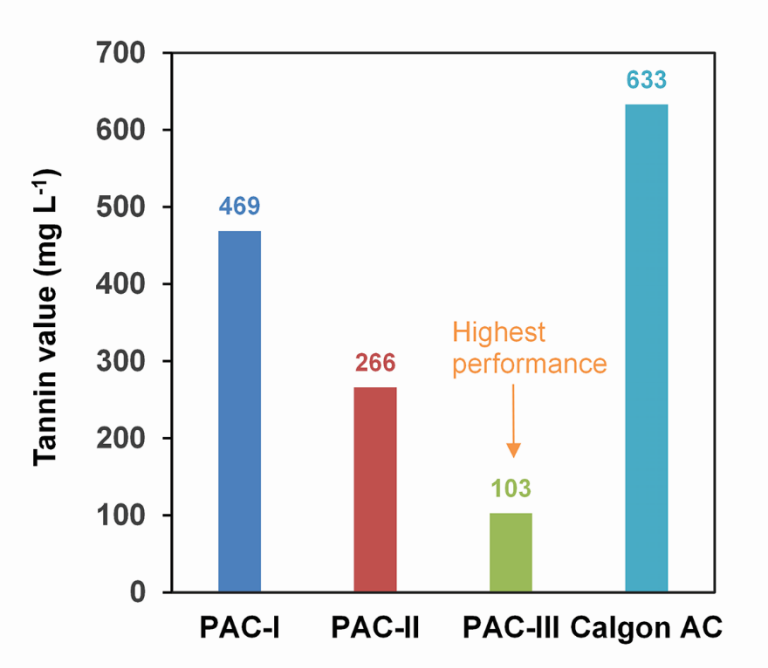

Figure 5.5 Tannin values of the PACs.

5.3.2 Chemical Absorption

5.3.2.1 Copper (II) Absorption

Copper is a micro-essential trace element for the growth of all biological creatures such as humans, plants, animals, and microorganisms (Ghaedi et al., 2015). However, if the concentration of copper exceeds the safe limit, it will lead to various injurious health problems. The excess copper may be related with the liver, bone, central nervous system, immune system impairment and even pernicious anemia (Goodman et al., 2005; Stern, 2010). Thus, copper ion absorption is important for drinking water. Figure 5.6 shows that the copper (II) removal of PAC-I, PAC-II, PAC-III, and Calgon AC can be 96.4%, 97.4%, 97.4%, and 97.2%, respectively. Among them, PAC-II and PAC-III showed better property for copper (II) absorption, which matched

the results of $SPV_{micropore}$ of PACs. As a small molecular, copper ion prefers to be absorbed by the micropore of the carbon (Table 5.1).

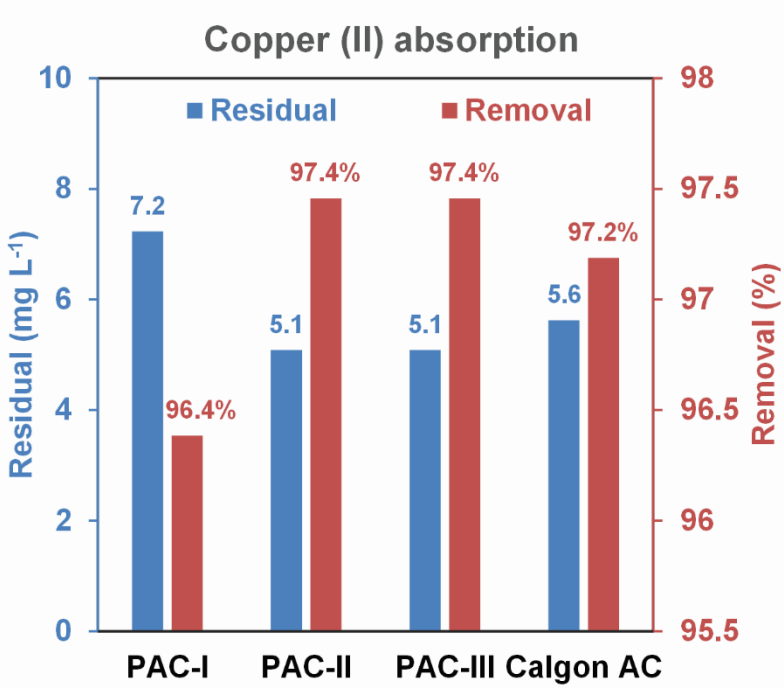

Figure 5.6 Copper (II) absorptions of the PACs.

5.3.2.2 Rhodamine 6G Absorption

The removal of rhodamine 6G (Figure 5.1b) is a common organic dye with a molecular size larger than 2 nm, therefore, the meso-macropore structure of the carbon may play a critical role in the rhodamine 6G absorption. Figure 5.7 shows the rhodamine 6G solution after being treated with PACs for 24 h. It was easy to see that the solution being treated by Calgon AC still presented red color, however, the others (kenaf core-based PAC) were visible to be as clear as water (Figure 5.7). The UV-vis analysis showed that 99.93% of the rhodamine 6G was removed by PAC-I, PAC-II, and PAC-III, however, only 99.19% of that by Calgon AC (Figure 5.8). The reason could be

the relatively low meso-macropore structure in the Calgon AC (Table 5.1) to absorb the rhodamine 6G molecular (Figure 5.1b).

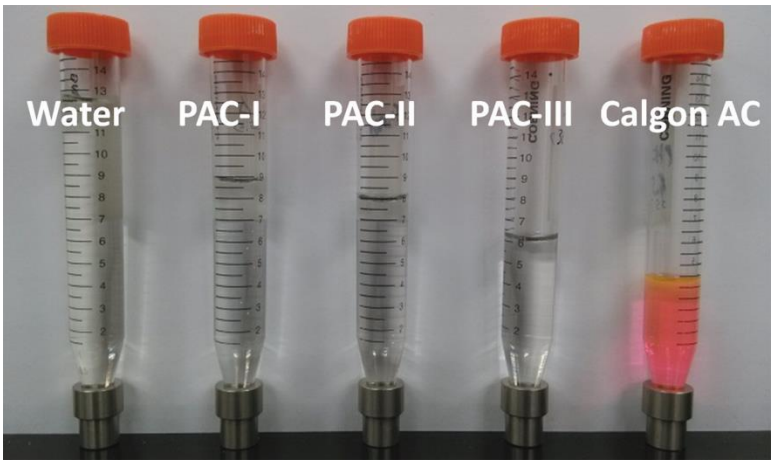

Figure 5.7 Comparison of the Rhodamine 6G solution after 24 h stirring with the PACs.

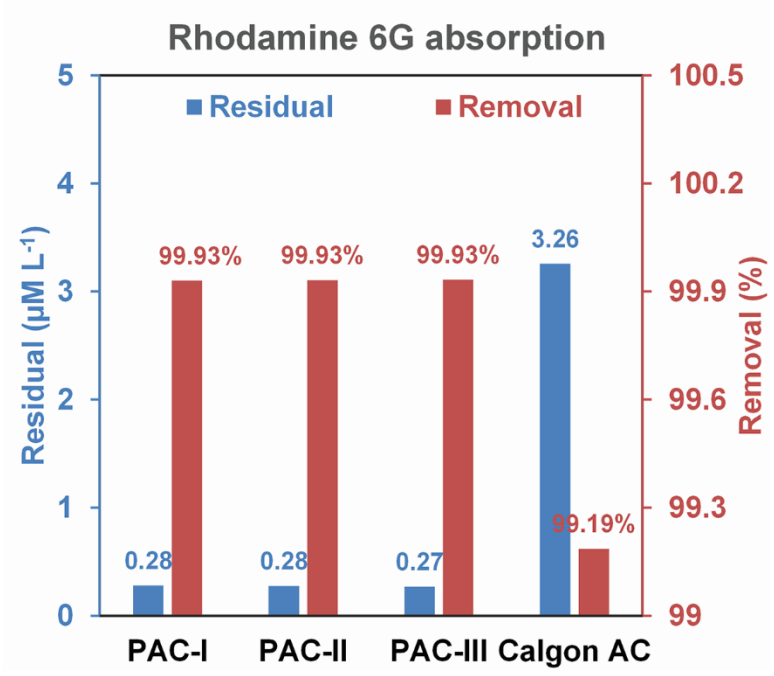

Figure 5.8 Rhodamine 6G absorptions of the PACs.

5.3.2.3 Crude Oil Absorption

The problem of crude oil dissolved water widely exists in the oil industry. It is challengeable work to clarify the water that is trapped in underground formations and brought to the surface along with oil or gas (Veil et al., 2004). The produced water mainly come from oil, gas, and coal bed methane productions. According to the report from American Petroleum Institute (API) (The American Petroleum Institute, 2000), about 18 billion barrels (bbl) of produced water was generated by United States onshore operations in 1995. Figure 5.9 presents the comparison of the PACs on the capability of crude oil absorption in the water, indicating that PAC-II owns the best capability, and Calgon AC produced the worst. The results do not show any relationship with the SPV of PACs, and the further investigation is needed.

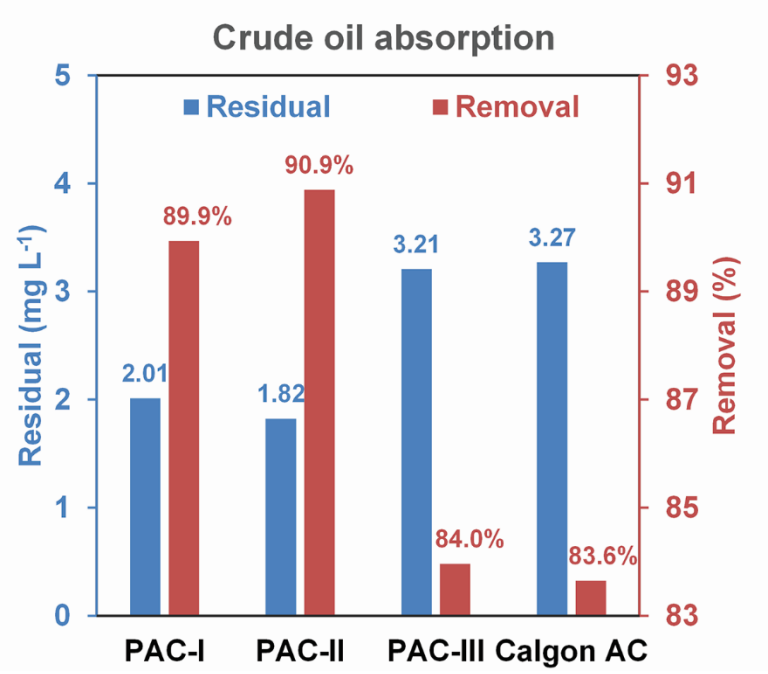

Figure 5.9 Crude oil absorptions of the PACs.

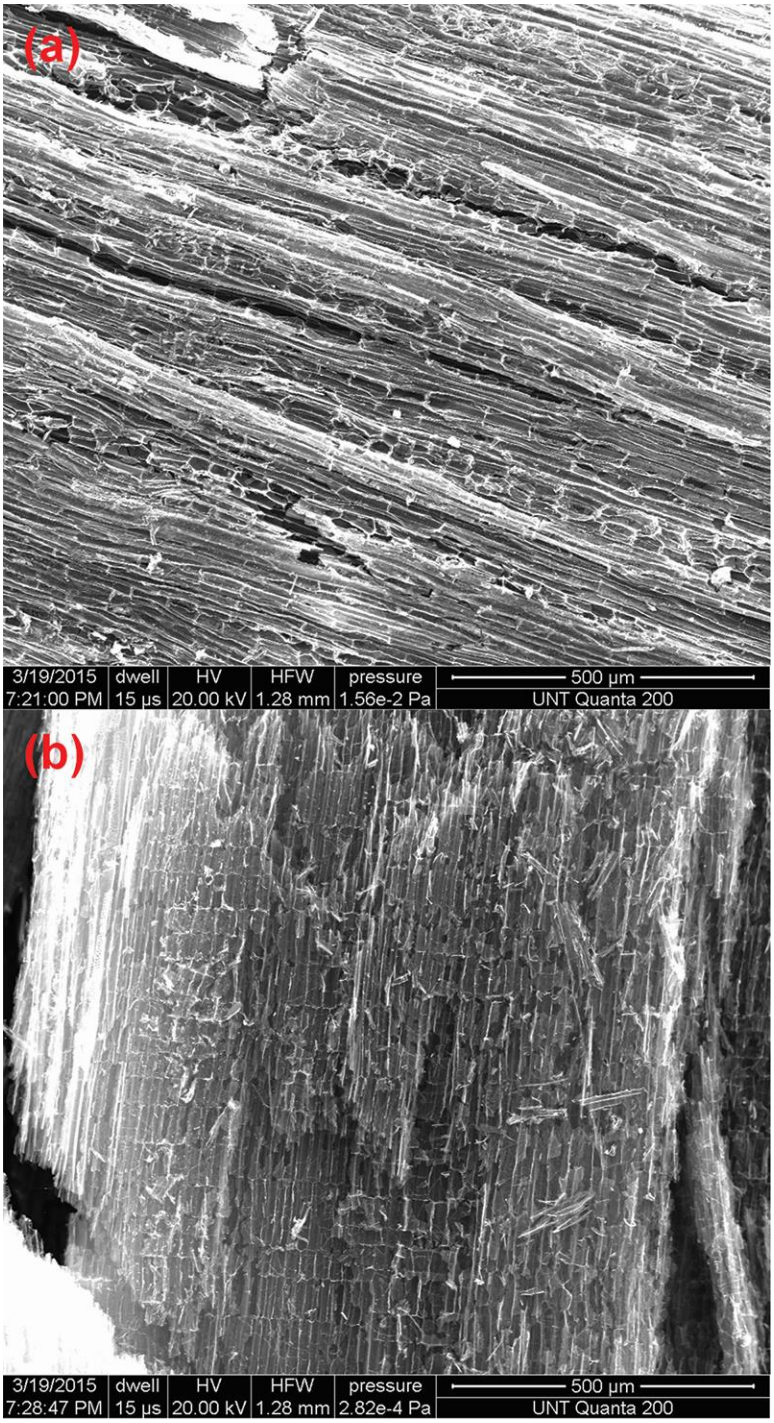

Figure 5.10 SEM observation of kenaf core-based activated carbon with non-activation (a) and self-activation (b).

5.3.3 Oil-Absorption Capacity

Kenaf core is a current commercial product as oil absorbent by Kengro Corporation, USA. However, after being converted into activated carbon, the internal porosity is able to increase, resulting in a better capacity of oil absorption. Based on the activation model shown in Figure 2.8, the porosity is significantly increased during the activation process. Figure 5.10 shows the scanning electron microscope (SEM) images of the kenaf core-based activate carbon with non-activation and self-activation. It is observed that the cell walls of the carbon become really thin after the self-activation process, which will dramatically increase the porosity of the carbon.

The oil absorption tests were carried out with the procedures described in Figure 5.3. The results show that the oil-absorption capacity of kenaf core-based activated carbon can be 22.4 g per 1 g absorbent, which is approximate 4.6 times higher than the original kenaf core (Figure 5.11). As expected, the oil-absorption capacity was dramatically improved after the treatment. Additionally, the dispose of oil-absorbed activated carbon was investigated. The preliminary experiment of oil recycling from the oil absorbed activated carbon was carried out (Figure 5.12). A syringe was used to extrude the oil out from the absorbent. It showed that about 52.5% oil is able to recycle using hand pressure.

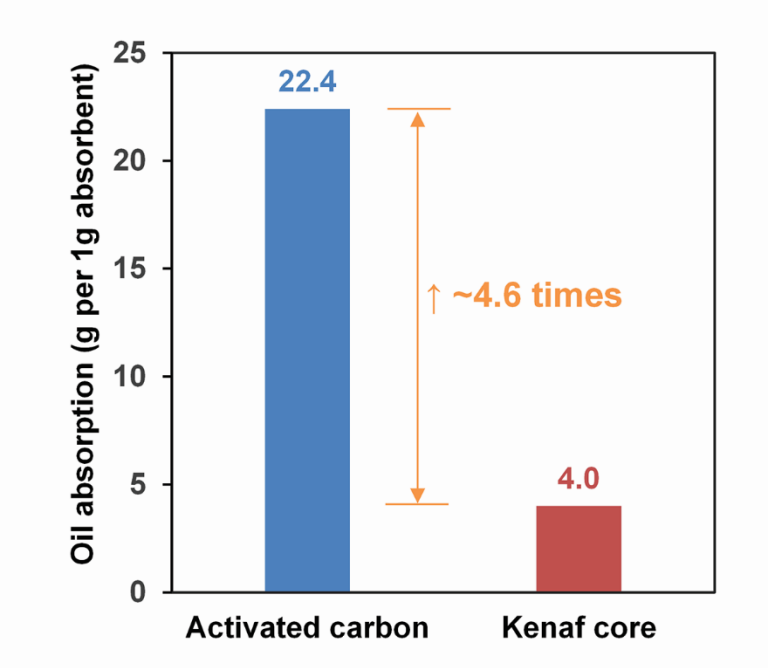

Figure 5.11 Comparison of oil absorption of PAC-II and kenaf core.

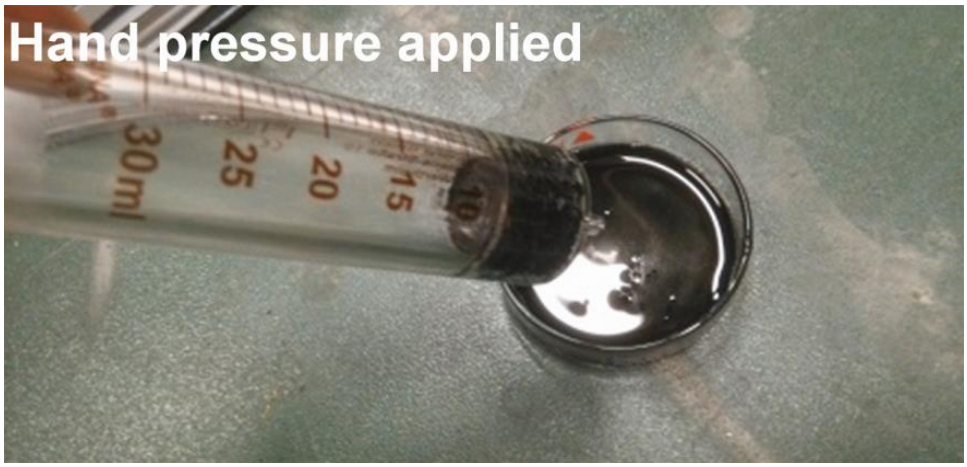

Figure 5.12 Oil recycle after absorbed by PAC-II.

5.4 Conclusions

Kenaf core-based activated carbon from self-activation showed good performances on the water cleaning and oil absorption. Compared to the commercial

activated carbon from Calgon Corporation, these activated carbons own comparable or better capacities (Table 5.3). It is found that micropore of the activated carbon more prefers to absorb small-molecular impurities, and meso-macropore is good at absorbing big-molecular impurities. Additionally, the oil-absorption capacity was increased by 4.6 times after the kenaf core being converted into activated carbon.

Table 5.3 Data summary of performances of PACs for water cleaning.

Performance	High → low			
BET surface area (m^2/g)	PAC-III (2296)	PAC-II (2266)	PAC-I (901)	Calgon AC (836)
Micropore volume (cm^3/g)	PAC-III (0.809)	PAC-II (0.783)	Calgon AC (0.402)	PAC-I (0.395)
Meso-Macropore volume (cm^3/g)	PAC-III (2.329)	PAC-II (0.962)	PAC-I (0.251)	Calgon AC (0.044)
Iodine Number (mg/g)	PAC-III (2120)	PAC-II (2040)	Calgon AC (1053)	PAC-I (952)
Tannin Value (mg/L)	PAC-III (103)	PAC-II (266)	PAC-I (469)	Calgon AC (633)
Cu(II) (200mg/L) removed (final conc. mg/L)	PAC-III (5.1)	PAC-II (5.1)	Calgon AC (5.6)	PAC-I (7.2)
Rhodamine 6G (4μM) removed (final conc. μM)	PAC-III (0.27)	PAC-II (0.28)	PAC-I (0.28)	Calgon AC (3.26)

5.5 References

Annadurai, G., Juang, R.S., Lee, D.J., 2001. Adsorption of Rhodamine 6G from aqueous solutions on activated carbon, *Journal of Environmental Science and Health Part A-Toxic/Hazardous Substances & Environmental Engineering*, 36(5), 715-725.

Corkery, M., 2010. BP Oil Spill Costs: $20 Billion? Try $63 Billion, http://blogs.wsj.com/deals/2010/06/16/bp-oil-spill-costs-20-billion-try-63-billion/, Accessed on 3/8/2016.

Ghaedi, A.M., Ghaedi, M., Vafaei, A., Iravani, N., Keshavarz, M., Rad, M., Tyagi, I., Agarwal, S., Gupta, V.K., 2015. Adsorption of copper (II) using modified activated carbon prepared from Pomegranate wood: Optimization by bee algorithm and response surface methodology, *Journal of Molecular Liquids*, 206, 195-206.

Goodman, V.L., Brewer, G.J., Merajver, S.D., 2005. Control of copper status for cancer therapy, *Current Cancer Drug Targets*, 5(7), 543-549.

Hardcastle, J.L., 2014. Chemical Spill Cost West Virginia Businesses $61M, http://www.environmentalleader.com/2014/02/05/chemical-spill-cost-west-virginia-businesses-61m/, Accessed on 3/8/2016.

Shi, S.Q., Xia, C., 2014. Porositization process of carbon or carbonaceous materials, US patent 14/211,357.

Stern, B.R., 2010. Essentiality and toxicity in copper health risk assessment: overview, update and regulatory considerations, *Journal of Toxicology and Environmental Health-Part A-Current Issues*, 73(2-3), 114-127.

The American Petroleum Institute, 2000. Overview of exploration and production waste volumes and waste management practices in the United States, http://www.api.org/~/media/files/ehs/environmental_performance/icf-waste-survey-of-eandp-wastes-2000.pdf?la=en, 2/17/2016.

Veil, J.A., Puder, M.G., Elcock, D., Redweik Jr, R.J., 2004. A white paper describing produced water from production of crude oil, natural gas, and coal bed methane, http://www.circleofblue.org/waternews/wp-content/uploads/2010/08/prodwaterpaper1.pdf, Argonne National Laboratory, Technical Report 3/8/2016.

Wikipedia, 2016. Activated Carbon, https://en.wikipedia.org/wiki/Activated_carbon, Accessed on 3/8/2016.

Xia, C., Shi, S.Q., 2016a. Self-activation for activated carbon from biomass: theory and parameters, *Green Chemistry*, Accepted Manuscript, In Press, doi: 10.1039/C5GC02152A.

Xia, C., Shi, S.Q., 2016b. Self-activation process to fabricate activated carbon from kenaf, *Wood and Fiber Science*, 48, 62-69.

Xia, C., Shi, S.Q., 2015. Self-activation process for biomass based activated carbon, *Proceedings of 58th International Convention of Society of Wood Science and Technology (SWST)*, 2015, 98-104.

Yahya, M.A., Al-Qodah, Z., Ngah, C.W.Z., 2015. Agricultural bio-waste materials as potential sustainable precursors used for activated carbon production: A review, *Renewable & Sustainable Energy Reviews*, 46, 218-235.

Zhang, D., Shi, S.Q., Pittman Jr, C.U., Jiang, D., Che, W., Gai, Z., Howe, J.Y., More, K.L., Antonyraj, A., 2012. Versatile and biomass synthesis of iron-based nanoparticles supported on carbon matrix with high iron content and tunable reactivity, *Journal of Nanoparticle Research*, 14(8), 1-12.

CHAPTER 6

ELECTROMAGNETIC INTERFERENCE SHIELDING [§]

6.1 Introduction

Electromagnetic interferences (EMI), which are conducting and radiating electromagnetic signals emitted by electrical circuits, perturb proper operation of surrounding electrical equipment or cause radiative damage to living organisms (Huynen et al., 2011; Thomassin et al., 2013). An abundance of EMI shielding materials and technologies have been synthesized and designed to reduce the interferences caused by electromagnetic signals, e.g., metal sheets (Mihut et al., 2012), carbon materials (Chen et al., 2015; Chiang and Ao, 1995; Das et al., 2011; Hu and Kim, 2008; Joshi et al., 2015; Liang et al., 2009; Luo and Chung, 1999; Mohanraj et al., 2006; Xia and Shi, 2016; Xu et al., 2007), electroless plating (Sun et al., 2012), honeycomb design (Huynen et al., 2011), and coating (Lee et al., 2002). Three mechanisms of EMI shielding were investigated (Chung, 2001): reflection, which involves the application of metal sheets; absorption mechanism, which happens in amorphous materials; and multiple reflections, which refer to the reflections at various surfaces or interfaces in the shield.

Currently, the most common EMI shielding is metal sheets (such as nickel film (Yu et al., 2009), copper film (Xia et al., 2016a), and iron and cobalt particles (Jalali et

[§] This entire chapter is reproduced from Changlei Xia, Shifeng Zhang, Han Ren, Sheldon Q. Shi, Hualiang Zhang, Liping Cai, Jianzhang Li “Scalable fabrication of natural-fiber reinforced composites with electromagnetic interference shielding properties by incorporating powdered activated carbon” Materials, 2016, 9(1): 10, http://dx.doi.org/10.3390/ma9010010, with permission from the Multidisciplinary Digital Publishing Institute (MDPI) AG (Basel, Switzerland).

al., 2011)) because of their excellent reflection of electromagnetic signals. However, metal sheets also have disadvantages such as high density, corrosive action, uneconomic processing and secondary electromagnetic pollution resulting from the reflection (Wang et al., 2005). These drawbacks deter metal sheets from practical applications in the EMI shielding field. Therefore, a need exists to develop new materials that feature similar EMI shielding characteristics as metal sheets but are easier to be manufactured, as well as more economical and portable.

Interest in the development of carbon-based EMI shielding has arisen driven because of the following advantages the material offers: corrosion-resistance, low density, environmentally friendly, and easy to manufacture. The reported EMI shielding applications of carbon materials included carbon black (Mohanraj et al., 2006), carbon nanotube (Chen et al., 2015; Xu et al., 2007), carbon fiber (Chiang and Ao, 1995; Luo and Chung, 1999), carbon nonfiber (Das et al., 2011), activated carbon fiber (Hu and Kim, 2008), and graphene sheets (Joshi et al., 2015; Liang et al., 2009). Like other carbon materials, activated carbon demonstrates good EMI shielding effectiveness and EMI absorption (Chen et al., 2015; Chiang and Ao, 1995; Das et al., 2011; Hu and Kim, 2008; Joshi et al., 2015; Liang et al., 2009; Luo and Chung, 1999; Mohanraj et al., 2006; Xu et al., 2007). Activated carbon is an inexpensive resource with low density, and the cost effectiveness and large production of activated carbon increase the possibility of wide utilization as an EMI shielding candidate. However, no report was found in the literature review about the use of powdered activated carbon (PAC) for EMI shielding composites. Vacuum-assisted resin transfer molding (VARTM) process was performed to manufacture PAC incorporated kenaf-fiber reinforced composites, which is turned out

to be an excellent process for fabricating hybrid polymer-matrix composites (Xia et al., 2015b; Xia et al., 2015c; Xia et al., 2016b).

Activated carbon is a crude form of graphite with a random or amorphous structure, which is highly porous with large internal surface area (Hamerlinck et al., 1994; Mohan and Pittman Jr, 2006). Activated carbon is a cheap resource with low density and electromagnetic absorption properties. The low price and large production of activated carbon increase the possibility of the wide utilization as an EMI shielding candidate. This work was aimed at developing EMI shielding composites using kenaf fibers by incorporating PAC.

6.2 Materials and Methods

6.2.1 Materials

The kenaf bast fibers were obtained from Kengro Corporation (Charleston, MS, USA). The sodium hydroxide (NaOH) solution (5%, w/v) was prepared using NaOH beads (≥97%, Acros Organics, Morris Plains, NJ, USA) and deionized water. The activated carbon (12 × 40 mesh) was purchased from Calgon Carbon Corporation (Pittsburgh, PA, USA). The unsaturated polyester AROPOL Q6585 (30% styrene, Ashland Chemicals, Roseland, NJ, USA) and tert-butyl peroxybenzoate (t-BP, 98%, Acros Organics, Morris Plains, NJ, USA) were used to fabricate the kenaf fiber reinforced composites.

6.2.2 Preparation of Powdered Activated Carbon

Using the ultra-fine pulverizing machine (RT-UF26, Rong Tsong Precision Technology Co., Taichung, Taiwan), the activated carbon was reduced to powder. According to the requirements of the American National Standards Institute/American Water Works Association (ANSI/AWWA) B600-10 standard, the particle-size distribution of PAC was: not less than 99% of the activated carbon shall pass a No. 100 sieve, not less than 95% shall pass a No. 200 sieve, and not less than 90% shall pass a No. 325 sieve. The particle-size distribution of the PAC was measured by a Beckman Coulter Delsa™ Nano C Particle Analyzer (Beckman Coulter, Inc., Irving, TX, USA). PAC was dispersed into the DI-water with a concentration of 1 $mg \cdot mL^{-1}$. Prior to the particle-size measurement, PAC/aqueous dispersion was treated by a VCX 1500 ultrasonic (Sonics & Materials Inc., Newtown, CT, USA) for 5 min.

6.2.3 Preparation of Preformed Mats

Measured by a Mettler-Toledo HB43-S Moisture Analyzer (Mettler-Toledo LLC, Columbus, OH, USA), the average moisture content of the kenaf bast fibers was 9.1%. A mixture of 100 g kenaf fibers and 1.8 L NaOH solution was added into a hermetical reactor (251 M, Parr Instrument Co., Moline, IL, USA). With a saturated vapor pressure of 0.60 MPa, the alkali retting process was conducted at 160 °C for one hour while the mixture was being mechanically stirred. The excessive ionic solution was removed from the kenaf fibers by gravity after cooling to room temperature, and then by hand-squeezing. After the retting process, the retted fibers were measured as 36.6% ± 1.2% of the original ones.

PAC was stirred in 1 L water at 70 °C for approximate 30 min, and then mixed with fresh alkali retted kenaf fibers with another 30 min of stirring. The mixture was formed into a preform mat with a dimension of approximate 100 × 165 × 10 mm^3, and was dried at 105 °C for 24 h. Three different amounts (10, 20, and 30 g) of PAC (6.1% moisture content, measured by a Mettler-Toledo HB43-S Moisture Analyzer) were loaded to kenaf fibers to create three types of composites, Fiber/PAC10, Fiber/PAC20, and Fiber/PAC30.

6.2.4 Composites Fabrication through VARTM Process

Four types of composites, *i.e.*, Fiber/PAC10/polyester, Fiber/PAC20/polyester, Fiber/PAC30/polyester and Fiber/polyester (as control panels using un-treated fibers), were fabricated using the unsaturated polyester resin with 1.5% of t-BP catalyst and the VARTM process, which was described in our previous reports (Xia et al., 2014; Xia et al., 2015a). Briefly, after applying a mold-release agent on the surface of the mold, the preform was placed on the mold. A vacuum bag was placed over the mold. After vacuum tubes were inserted in the bag, resin infusion was carried out by a vacuum that was created between the mold and the bag. As a result, the catalyzed resin was supplied to the infusion tubes. The vacuum pulled the resin along the distribution layer into the preformed mats. A vacuum of 10–12 Torr was applied to the infusion system by the vacuum pump (Vacmobile 20/2 System with Becker U4.20, Vacmobiles.com Limited, Auckland, New Zealand). The resin was cured in the hot press with a pressure of 13 MPa. The resin-infused preforms were cured in two temperature steps, *i.e.*, 100 °C for 2 h, and then 150 °C for 2 h. Once the resin cured and cooled down to room

temperature, the vacuum bag and distribution layer were removed. Before the mechanical property measurements, all the specimens were conditioned approximate 30 days to a constant weight in a conditioning chamber maintained at a relative humidity of 50% ± 2% and a temperature of 20 ± 3 °C.

6.2.5 Specific Surface Area and Pore Structure Analysis

The specific surface areas of the samples were analyzed by the surface area analyzer (3Flex, Micromeritics Instrument Corp., Norcross, GA, USA) in terms of nitrogen adsorption/desorption at 77 K. Based on the isothermal plots from P/P_0 = 0.05 to 0.3, the surface areas of the samples were obtained in accordance with the Brunauer-Emmett-Teller (BET) model. The specific pore volume distribution of the samples was analyzed by means of the Density Functional Theory (DFT) model.

6.2.6 Microtopography Analysis of Fibers

The surface topologies of the un-treated kenaf fibers and Fiber/PAC30 were examined using a Quanta 200 environmental scanning electron microscope (SEM, FEI Company, Hillsboro, OR, USA) with an accelerating voltage of 20 kV and magnifications of 1000× and 2000×. Prior to the SEM tests, the specimens were coated by a gold sputtering coater for 5 min to prevent charging of the specimen by the SEM electron beam.

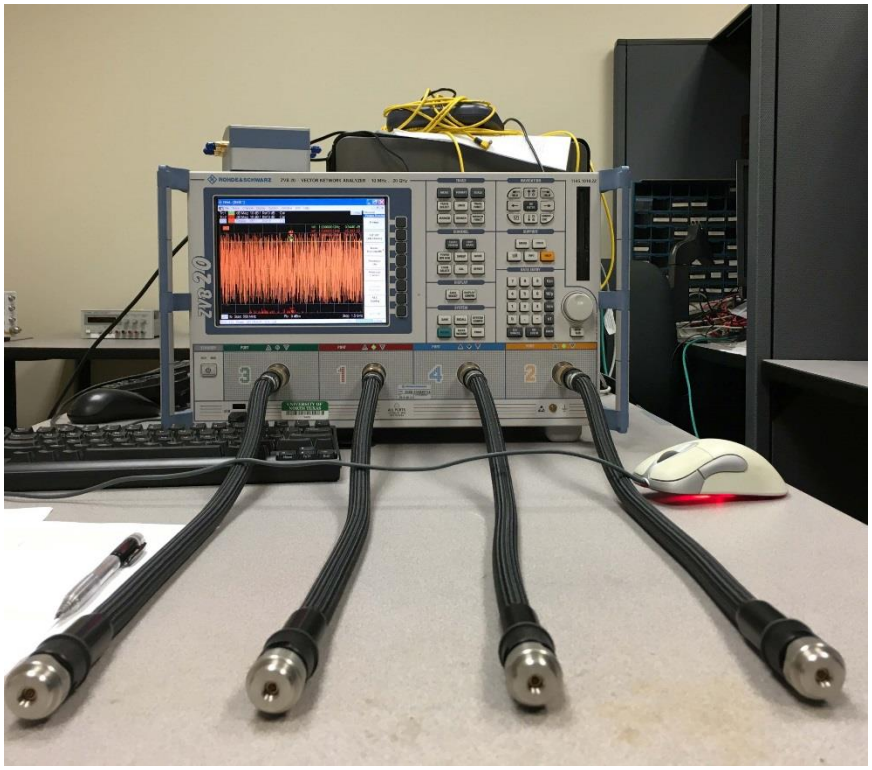

Figure 6.1 Vector Network Analyzer for the measurement of EMI shielding effectiveness.

6.2.7 Electromagnetic Interference Shielding Tests

The EMI shielding effectiveness measurement with both amplitude and phase properties were carried out using the vector network analyzer (HP E8363B, Agilent Technologies, Inc., Santa Clara, CA, USA) (Figure 6.1) with a frequency ranging from 8 GHz to 12 GHz. As the most common type of network analyzer, the vector network analyzer could be also called a gain-phase meter or an automatic network analyzer. Two *S*-parameters (%), including *S*11 (reflected), and *S*21 (transmitted), were detected and recorded. The EMI shielding effectiveness (%) and EMI absorption of composites were plotted using with Equations (1) and (2), respectively.

$$\text{EMI shielding effectiveness}\ (\%) = (1 - S21) \times 100 \quad (1)$$

$$\text{EMI absorption}\ (\%) = (1 - S21 - S11) \times 100 \quad (2)$$

6.2.8 Mechanical Property Tests

From each composite, twelve specimens measuring 25 × 160 × 3 mm^3 were cut in order to examine the modulus of elasticity (MOE) and modulus of rupture (MOR) of the composites. The Shimadzu AGS-X universal testing machine was used for the examinations in accordance with the procedure of 3-point bending test described in ASTM D790 standard. Three-point bending set-up was used with a span of 50 mm and a crosshead speed of 1.3 mm/min.

6.2.9 Dynamic Mechanical Analysis

The dynamic mechanical analysis (DMA) was performed using a TA instruments Q800 DMA tester (TA instruments Inc., New Castle, DE, USA). Each specimen measuring about 1 × 4 × 30 mm^3 were used for the tests. Three-point bending with a gauge length of 25.4 mm was performed. These testing parameters were conducted, including the temperature range of 22–200 °C with a ramping of 5 °C·min^{-1}, and the frequency of the oscillation at 1 Hz. The storage modulus (*E′*), loss modulus (*E″*) and mechanical loss factor (tan(δ)) were recorded and plotted as a function of temperature.

6.3 Results and Discussion

6.3.1 Fiber Characterization

The particle-size and distribution of PAC were determined by the light scattering method. Figure 6.2a shows that the diameter of the PAC particle was mainly in 95–400

nm with a peak at 140.3 ± 35.6 nm. The average particle size of PAC was calculated to be 265.9 ± 5.1 nm. The specific surface area of the PAC was 835.7 ± 22.3 m^2/g according to the BET theory, in which the micropore (<2 nm, as defined by the International Union of Pure and Applied Chemistry (IUPAC)) specific surface area was 708.5 m^2/g (84.8% of the total surface area). The pore structure of the PAC is shown in Figure 6.2b by means of a DFT model. The total specific pore volume was 0.362 cm^3/g, and almost all of the pore volume was in the micropore range (Figure 6.2b).

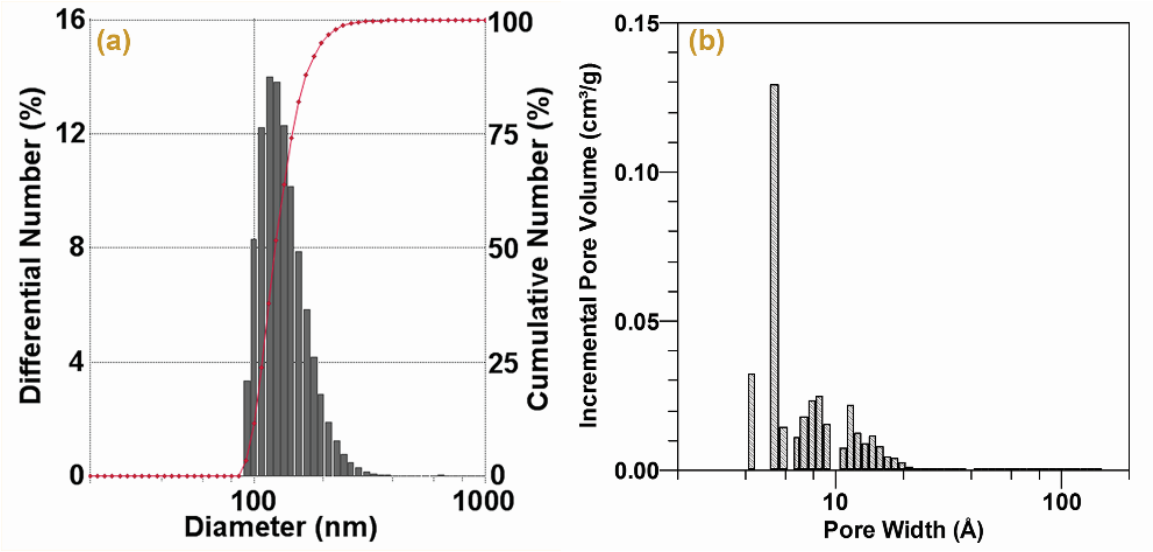

Figure 6.2 Particle-size distribution (a) and DFT pore-size distribution; (b) of PAC.

The SEM photos of the un-treated fiber and Fiber/PAC30 are shown in Figure 6.3 for comparison. PACs on the surface were visible in the Fiber/PAC30 (Figure 6.3b1,b2), when compared with the un-treated fiber (Figure 6.3a1,a2). The PAC loading effectiveness was calculated from Equation (3) in terms of BET specific surface area (SA) and the results are shown in Table 6.1.

$$\text{PAC content (\%)} = \frac{SA_{Fiber/PAC} - SA_{Fiber}}{SA_{PAC} - SA_{Fiber}} \times 100 \quad (3)$$

where SA_{PAC}, SA_{Fiber}, $SA_{Fiber/PAC10}$, $SA_{Fiber/PAC20}$, and $SA_{Fiber/PAC30}$ were 835.6 ± 22.3, 3.3 ± 0.2, 115.1 ± 3.3, 221.0 ± 6.3, and 319.8 ± 9.5 m^2/g, respectively. The PAC loading effectiveness of each Fiber/PAC was calculated by Equation (4):

$$\text{PAC loading effectiveness (\%)} = \frac{\text{PAC content} \times \text{Weight of Fiber/PAC}}{\text{PAC feed}/(1+\text{PAC moisture content})} \times 100 \quad (4)$$

where PAC content was calculated by Equation (3), and PAC moisture content was 6.1%. The PAC loading effectiveness was found to be 66.6%, 77.9% and 84.7% for Fiber/PAC10, Fiber/PAC20, and Fiber/PAC30, respectively. These results show that the loading effectiveness increases with the increment of PAC feed. The reason was that hydrophobic PAC was absorbed onto the hydrophilic fiber surface that resulted from the very big specific surface area and high porosity as well as absorbability. The surface of the Fiber/PAC became hydrophobic and absorbed more PAC when the PAC loading further increased, which resulted in more effective absorption for PAC. The results reflect as the increment of the PAC loading effectiveness.

Table 6.1 Contents of PAC loaded fibers.

Sample	PAC Feed (g)	PAC Loading Effectiveness (%)	Content (%)	
			PAC [a]	Fiber
Fiber	-	-	0.0	100.0
Fiber/PAC10	10	66.6	13.4	86.6
Fiber/PAC20	20	77.9	26.2	73.8
Fiber/PAC30	30	84.7	38.0	62.0

[a] PAC = powdered activated carbon.

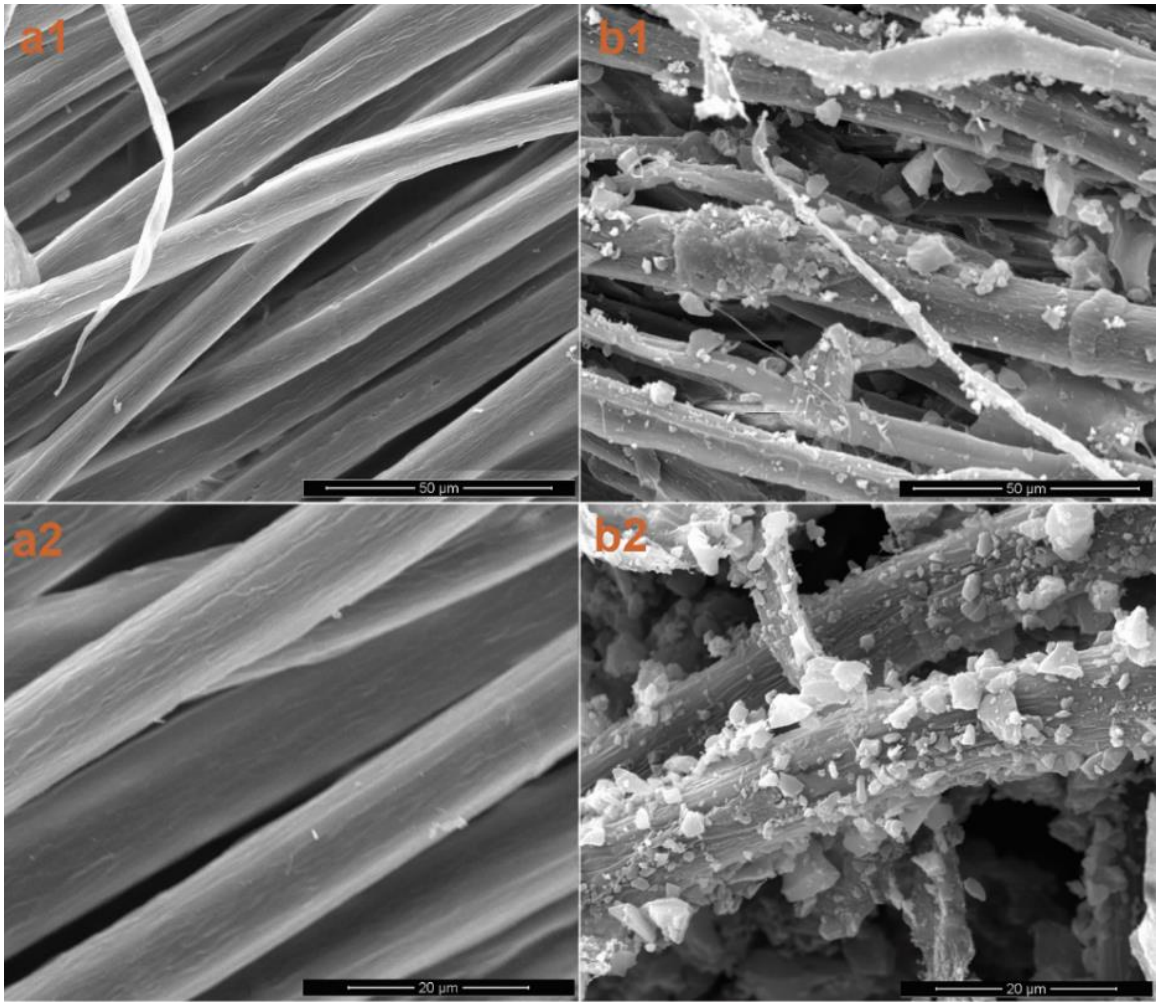

Figure 6.3 SEM observation of the un-treated fiber (a1,a2); and Fiber/PAC30 (b1,b2).

6.3.2 Composites Properties

The physical properties of composites manufactured through VARTM technology are shown in Table 6.2. The composite density was decreased with the increment in PAC content because of the porosity increment of the composites. The BET specific surface areas of Fiber/polyester, Fiber/PAC10/polyester, Fiber/PAC20/polyester, and Fiber/PAC30/polyester were 0.1, 0.4, 5.0, and 5.5 m^2/g, respectively, suggesting the increment of the porosity of the composites.

Table 6.2 Contents of the composites.

Composite	Density ($Kg \cdot m^{-3}$)	Thickness (mm)	Content (%)		
			Fiber	PAC [b]	Resin [c]
Fiber/polyester	1159.4 (44.5) [a]	2.6 (0.2)	66.7	0.0	33.3
Fiber/PAC10/polyester	1157.3 (15.1)	3.5 (0.1)	64.2	10.0	25.8
Fiber/PAC20/polyester	1064.7 (20.4)	4.2 (0.1)	57.9	20.5	21.7
Fiber/PAC30/polyester	1036.2 (18.8)	4.8 (0.2)	47.1	28.9	24.1

[a] mean (standard deviation);

[b] PAC = powdered activated carbon;

[c] polyester was used here.

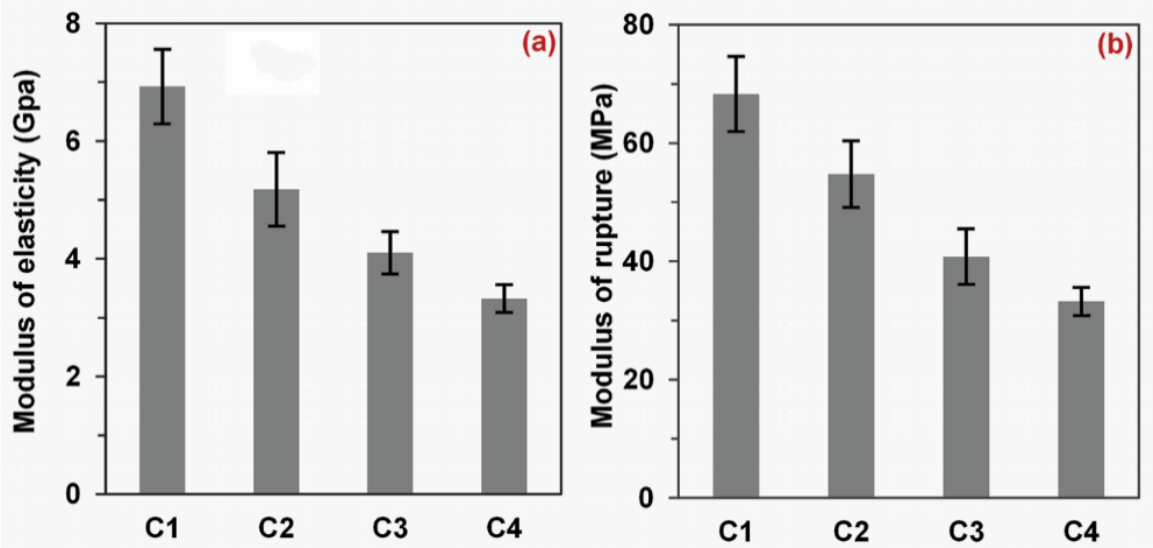

Figure 6.4 Modulus of elasticity (a) and rupture (b) of Fiber/polyester (C1), Fiber/PAC10/polyester (C2), Fiber/PAC20/polyester (C3), and Fiber/PAC30/polyester (C4) composites.

From the 3-point bending test results shown in Figure 6.4, the mechanical properties (MOE and MOR) of the composites decreased with the increase in PAC content, showing the same variation trend as the composite density results. MOE (3.3 GPa) and MOR (33.2 MPa) of the Fiber/PAC30/polyester decreased by 52.0% and 51.4%, as compared with Fiber/polyester (6.9 GPa MOE and 68.3 MPa MOR). The

main reason could be that the increment in porosity reduced the mechanical property (Chen et al., 2013).

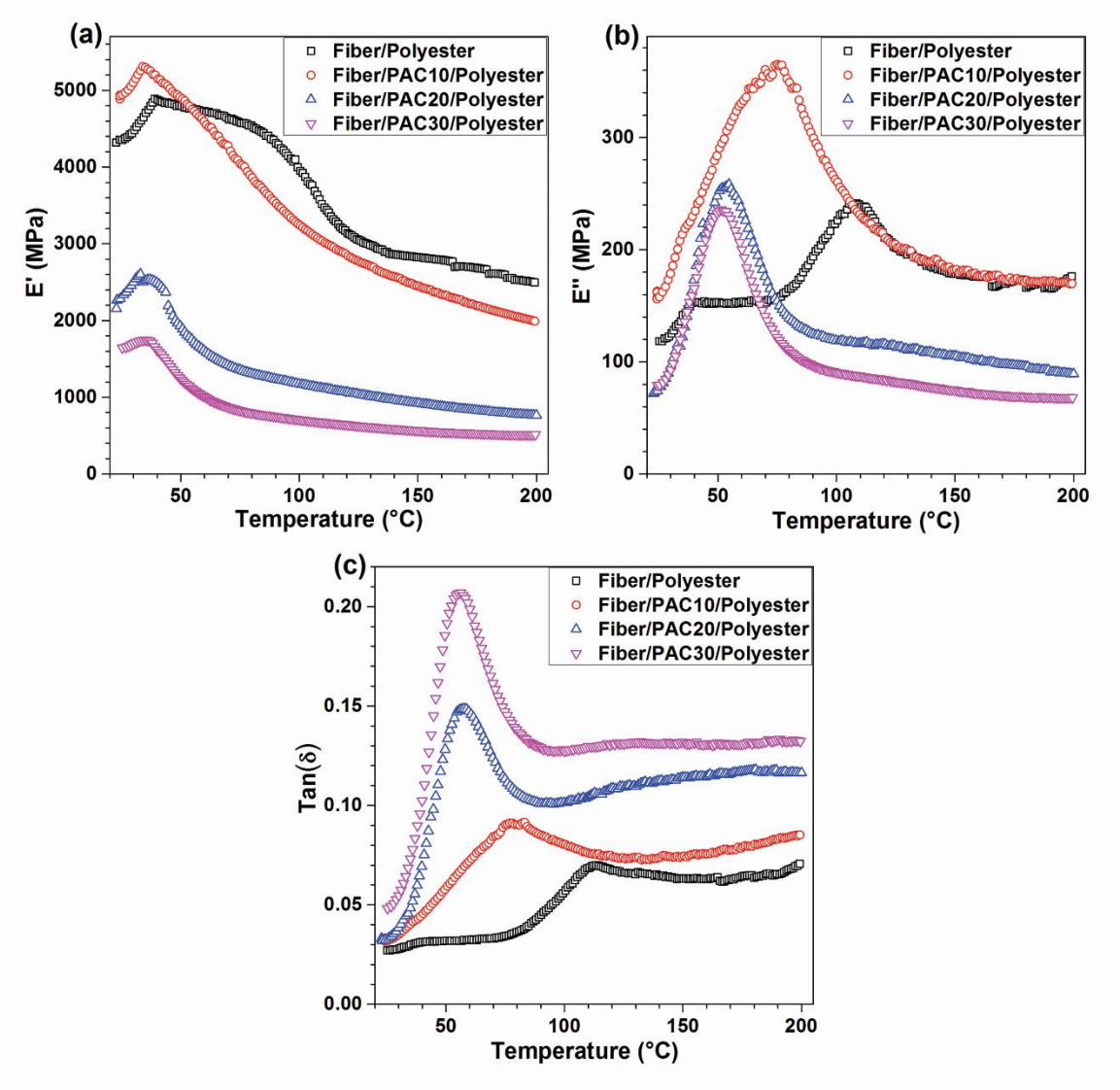

Figure 6.5 DMA results of the four composites, including storage modulus (a); loss modulus (b); and damping parameter (c).

Storage modulus is a crucial index for measuring the energy storage capability of material after elastic deformation, which was an index of resilience. Figure 6.5a shows

the *E′* of the four composites. In general, the *E′* of the four composites showed the maximum values around 32–39 °C, and then decreased as the temperature increased because of the chain mobility increasing of the polymer matrix (Islam et al., 2012). Similar to the mechanical properties (MOE and MOR), after adding PAC, *E′* decreased considerably compared with Fiber/polyester, indicating that additional PAC reduced the elastic properties of the composites. Figure 6.5b represents the loss modulus of the four composites. The *E″* of Fiber/PAC10/polyester, Fiber/PAC20/polyester, and Fiber/PAC30/polyester composites followed the same trend as that of *E′*. However, the *E″* of Fiber/polyester showed a lower value as compared with that of Fiber/PAC10/polyester composite because of the additional high-porous PAC. Figure 6.5c shows the loss factor of the four composites, reflecting the damping of molecular movement within the material. As the tan(δ) increased, the flow of the viscous molecules became harder, and the energy increasingly dissipated. With the increase of additional PAC, the tan(δ) increased gradually, indicating that PAC was able to restrict the movement of the chains and thus increase the damping effect. Additionally, as shown in Figure 6.5c, the glass transition temperatures of the Fiber/polyester, Fiber/PAC10/polyester, Fiber/PAC20/polyester, and Fiber/PAC30/polyester composites were obtained to be 113.4 °C, 83.2 °C, 57.6 °C, and 56.3 °C, respectively, which showed a increment with the amount of added PAC.

6.3.3 EMI Shielding

Figure 6.6 shows the EMI shielding and absorption of the four types of composites. The averaged EMI properties at the range of 8–12 GHz are summarized in

Table 6.3. The EMI shielding of Fiber/PAC30/polyester was 93.0%, which was increased by 124.6% compared with the Fiber/polyester composite. Since PAC is different from the common EMI shielding mechanism of reflection, it prefers the absorption of the EMI signals. The EMI absorptions of Fiber/polyester, Fiber/PAC10/polyester, Fiber/PAC20/polyester, and Fiber/PAC30/polyester were 21.2%, 31.7%, 44.7%, and 64.0%, respectively. The EMI absorption of Fiber/PAC30/polyester was increased by 201.7%, as compared with that of Fiber/polyester. The percentages of absorption in the EMI shielding and ratios of EMI absorption/shielding are presented in Table 6.3. The ratios of EMI absorption/shielding increased from 41.8% to 50.9% and 68.7% for the Fiber/PAC10/polyester to Fiber/PAC20/polyester and Fiber/PAC30/polyester, which indicated that the absorption percentage in EMI shielding increased with the increment of the PAC content. The EMI absorption/shielding of Fiber/PAC30/polyester (68.7%) was significantly increased by 37.1% (ANOVA test, $\alpha = 0.001$, p-value = 9.07×10^{-79}), compared with that of Fiber/polyester (50.1%), which indicated that the percentage of reflection in EMI shielding was significantly reduced. The increase of absorption resulted in the decrease of the secondary electromagnetic pollution.

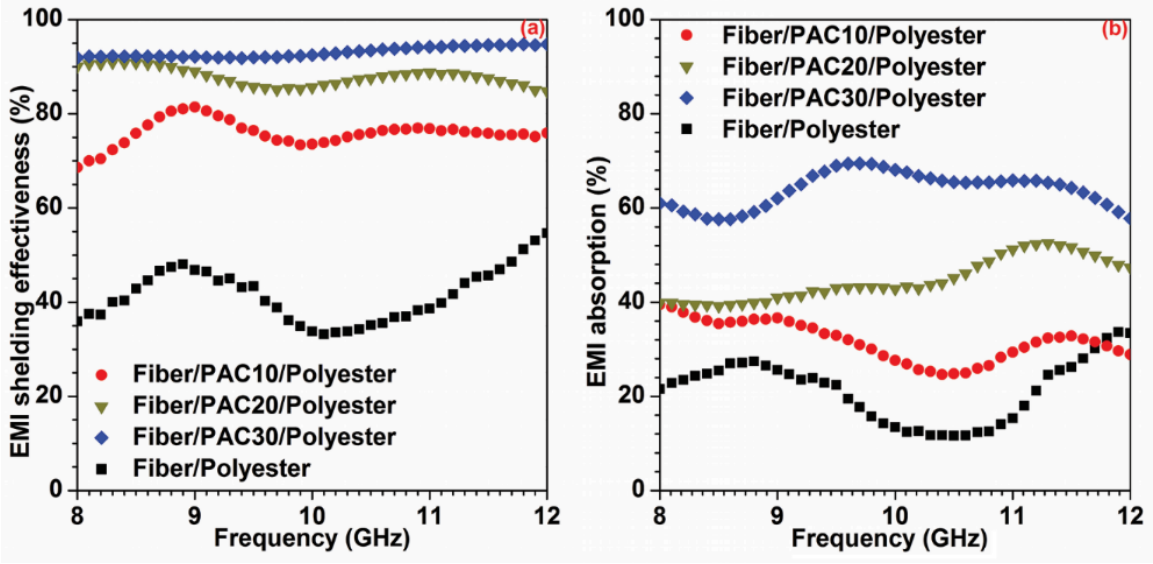

Figure 6.6 EMI shielding effectiveness (a) and absorption (b) of the four composites.

Table 6.3 EMI shielding and absorption of the four composites.

Composite	EMI Shielding (%)	EMI Absorption [a] (%)	EMI Absorption/Shielding (%)
Fiber/PAC10/polyester	76.0 (2.6) [b]	31.7 (4.2)	41.8 (5.7)
Fiber/PAC20/polyester	87.9 (1.8)	44.7 (4.4)	50.9 (5.4)
Fiber/PAC30/polyester	93.0 (1.1)	64.0 (3.7)	68.7 (4.1)
Fiber/polyester	41.4 (5.5)	21.2 (6.5)	50.1 (10.3)
Increment (%) [c]	124.6	201.7	37.1

[a] EMI = electromagnetic interference;

[b] mean (standard deviation) which were calculated from the data in 8–12 GHz;

[c] increments were calculated from the data of Fiber/PAC30/polyester and Fiber/polyester.

6.4 Conclusions

The composites were manufactured from kenaf fibers, PAC and polyester using the VARTM technology. The PAC loading effectiveness was determined using the BET specific surface area analysis, which showed an increase with the increase in PAC

loading. EMI shielding tests were carried out with a variable frequency ranging from 8 GHz to 12 GHz. As the PAC content increased from 0% to 28.9%, the EMI shielding and absorption increased from 41.4% to 93.0%, and 21.2% to 64.0%, respectively, and the ratio of EMI absorption/shielding significantly increased by 37.1%. The results showed that PAC was more effective at EMI signal absorption rather than reflection, which benefited the decrease of secondary electromagnetic pollution. However, the mechanical and dynamic mechanical properties decreased after the addition of PAC. Further work is planned to improve these properties of the composites.

6.5 References

Chen, X., Wu, S., Zhou, J., 2013. Influence of porosity on compressive and tensile strength of cement mortar, *Construction and Building Materials*, 40, 869-874.

Chen, Y., Li, Y., Chu, B.T.T., Kuo, I., Yip, M., Tai, N., 2015. Porous composites coated with hybrid nano carbon materials perform excellent electromagnetic interference shielding, *Composites Part B: Engineering*, 70, 231-237.

Chiang, W., Ao, J., 1995. Effect of surface treatment of carbon fiber on the electrical and mechanical properties of high-Impact polystyrene composite, *Journal of Polymer Research*, 2(2), 83-89.

Chung, D.D.L., 2001. Electromagnetic interference shielding effectiveness of carbon materials, Carbon, 39(2), 279-285.

Das, A., Hayvaci, H.T., Tiwari, M.K., Bayer, I.S., Erricolo, D., Megaridis, C.M., 2011. Superhydrophobic and conductive carbon nanofiber/PTFE composite coatings for EMI shielding, *Journal of Colloid and Interface* Science, 353(1), 311-315.

Hamerlinck, Y., Mertens, D., Vansant, E., 1994. Activated Carbon Principles in Separation Technology. Elsevier, New York.

Hu, Q., Kim, M., 2008. Electromagnetic interference shielding properties of CO_2 activated carbon black filled polymer coating materials, *Carbon Letters*, 9(4), 298-302.

Huynen, I., Quievy, N., Bailly, C., Bollen, P., Detrembleur, C., Eggermont, S., Molenberg, I., Thomassin, J.M., Urbanczyk, L., Pardoen, T., 2011. Multifunctional hybrids for electromagnetic absorption, *Acta Materialia*, 59(8), 3255-3266.

Islam, M.S., Hamdan, S., Talib, Z.A., Ahmed, A.S., Rahman, M.R., 2012. Tropical wood polymer nanocomposite (WPNC): The impact of nanoclay on dynamic mechanical thermal properties, *Composites Science and Technology*, 72(16), 1995-2001.

Jalali, M., Dauterstedt, S., Michaud, A., Wuthrich, R., 2011. Electromagnetic shielding of polymer-matrix composites with metallic nanoparticles, *Composites Part B: Engineering*, 42(6), 1420-1426.

Joshi, A., Bajaj, A., Singh, R., Anand, A., Alegaonkar, P.S., Datar, S., 2015. Processing of graphene nanoribbon based hybrid composite for electromagnetic shielding, *Composites Part B: Engineering*, 69, 472-477.

Lee, B.O., Woo, W.J., Park, H.S., Hahm, H.S., Wu, J.P., Kim, M.S., 2002. Influence of aspect ratio and skin effect on EMI shielding of coating materials fabricated with carbon nanofiber/PVDF, *Journal of Materials Science*, 37(9), 37, 1839-1843.

Liang, J., Wang, Y., Huang, Y., Ma, Y., Liu, Z., Cai, F., Zhang, C., Gao, H., Chen, Y., 2009. Electromagnetic interference shielding of graphene/epoxy composites, *Carbon*, 47(3), 922-925.

Luo, X.C., Chung, D.D.L., 1999. Electromagnetic interference shielding using continuous carbon-fiber carbon-matrix and polymer-matrix composites, *Composites Part B: Engineering*, 30(3), 227-231.

Mihut, D.M., Lozano, K., Tidrow, S.C., Garcia, H., 2012. Electromagnetic interference shielding effectiveness of nanoreinforced polymer composites deposited with conductive metallic thin films, *Thin Solid Films*, 520(21), 6547-6550.

Mohan, D., Pittman Jr, C.U., 2006. Activated carbons and low cost adsorbents for remediation of tri-and hexavalent chromium from water, *Journal of Hazardous Materials*, 137(2), 762-811.

Mohanraj, G.T., Chaki, T.K., Chakraborty, A., Khastgir, D., 2006. AC impedance analysis and EMI shielding effectiveness of conductive SBR composites, *Polymer Engineering and Science*, 46(10), 1342-1349.

Sun, L., Li, J., Wang, L., 2012. Electromagnetic interference shielding material from electroless copper plating on birch veneer, *Wood Science and Technology*, 46(6), 1061-1071.

Thomassin, J., Jerome, C., Pardoen, T., Bailly, C., Huynen, I., Detrembleur, C., 2013. Polymer/carbon based composites as electromagnetic interference (EMI) shielding materials, *Materials Science & Engineering R: Reports*, 74(7), 211-232.

Wang, L., Li, J., Liu, Y., 2005. Surface characteristics of electroless nickel plated electromagnetic shielding wood veneer, *Journal of Forestry Research*, 16(3), 233-236.

Xia, C., Ren, H., Shi, S.Q., Zhang, H., Cheng, J., Cai, L., Chen, K., Tan, H., 2016a. Natural fiber composites with EMI shielding function fabricated using VARTM and Cu film magnetron sputtering, *Applied Surface Science*, 362, 335-340.

Xia, C., Shi, S.Q., 2016. Self-activation for activated carbon from biomass: theory and parameters, *Green Chemistry*, Accepted Manuscript, In Press, doi: 10.1039/C5GC02152A.

Xia, C., Shi, S.Q., Cai, L., Hua, J., 2015a. Property enhancement of kenaf fiber composites by means of vacuum-assisted resin transfer molding (VARTM), *Holzforschung*, 69(3), 307-312.

Xia, C., Shi, S.Q., Cai, L., Nasrazadani, S., 2015b. Increasing inorganic nanoparticle impregnation efficiency by external pressure for natural fibers, *Industrial Crops and Products*, 69, 395-399.

Xia, C., Shi, S.Q., Cai, L., 2015c. Vacuum-assisted resin infusion (VARI) and hot pressing for CaCO3 nanoparticle treated kenaf fiber reinforced composites, *Composites Part B: Engineering*, 78, 138-143.

Xia, C., Shi, S.Q., Cai, L., 2014. Vacuum assisted resin transfer molding process for kenaf fiber based composites, *Proceedings of the 57th International Convention of Society of Wood Science and Technology (SWST)*, 2014, 459-465.

Xia, C., Zhang, S., Shi, S.Q., Cai, L., Huang, J., 2016b. Property enhancement of kenaf fiber reinforced composites by in situ aluminum hydroxide impregnation, *Industrial Crops and Products*, 79, 131-136.

Xu, X., Li, Z., Shi, L., Bian, X., Xiang, Z., 2007. Ultralight conductive carbon-nanotube-polymer composite, *Small*, 3(3), 408-411.

Yu, X., Shen, Z., Cai, C., 2009. Millimeter wave electromagnetic interference shielding by coating expanded polystyrene particles with a copper film using magnetron sputtering, *Vacuum*, 83(12), 1438-1441.

CHAPTER 7

SUMMARY AND FUTURE WORK

7.1 Self-Activation of Biomass

In this work, a novel activation process, namely self-activation, for activated carbon was developed. Taking advantage of that the gases emitted from the pyrolysis process of biomass to activate the converted carbon, self-activation saves the cost of activating agents and decreases the environmental impact. In the traditional activation process, physical activation using CO_2 and chemical activation using $ZnCl_2$ are two common methods. Both methods introduce additional gas (CO_2) or a chemical ($ZnCl_2$), in which the CO_2 emission from the activation process or the zinc compound removal by acid from the follow-up process will cause environmental concerns. In comparison with the conventional activation, the cost of activating agents is saved using the self-activation technology, since no activating gas or chemical is used. In addition, the self-activation process is more environmentally friendly, since the exhaust gases (CO and H_2) can be used as fuel or as feedstock for methanol production with further synthesis.

In order to understand the mechanism of the self-activation process, a novel model is developed. Gas activation is an oxidation process on the carbon surface to increase the specific surface area (SSA). It is assumed that the oxidations happen uniformly on the entire surface of the carbon. In the model, two scenarios may happen during the activation process (Figure 2.8), i.e. pore expansion and pore combination. During the pore expansion process, SSA and pore volume (SPV) of the carbon particle are increased (Figure 2.8 A to B). During the pore combination, SPV is still increased,

however, SSA is decreased owing to the wall disappearance between the pores (Figure 2.8, B to C).

Self-activation of biomass, including kenaf core, kenaf fiber, sugarcane bagasse, sugarcane leaf, coconut fiber, peanut shell, sawdust, and pine wood, were investigated. Compared to non-activation, the specific surface areas of the resulted carbons were dramatically increased to over 500 m^2 g^{-1} (the minimum requirement of activated carbon) after self-activation. The self-activations of kenaf core, kenaf fiber and pine wood were discussed in-depth.

In the study of the self-activation of kenaf core, the suggested pyrolysis temperature for the self-activation process is between 970 – 1,090°C, and the most effective pyrolysis temperature is expected to be around 1,090°C. The highest SSA and SPV reached 2432 m^2 g^{-1}, and 1.876 cm^3 g^{-1}, respectively. The relationships between yields and SSA, SPV of micropore, meso-macropore and the total, were investigated. These relationships were well explained by the activation model. In addition, the study of the effectiveness of kenaf core for producing highest total surface area showed that the yield of 9.0% received a maximum surface area per using gram kenaf core, and the yields between 5.5% and 13.8% were recommended for more than 90% effectiveness.

In Chapter 3, the self-activation of kenaf fiber was investigated. It was found that the relationships between yield and nature log of SSA had lineal fittings. The highest SSA could be 1742 m^2 g^{-1}. The study of the kenaf fiber's effectiveness for producing highest total surface area showed that the yield of 10.2% received a maximum surface area per using gram kenaf fiber, and the yields between 7.2% and 13.8% were recommended to obtain an effectiveness of more than 95% of the maximum.

7.2 Applications

The studies of activated carbon applications include lithium-ion battery (LIB) manufacturing, water cleaning, and electromagnetic interference (EMI) shielding. In Chapter 4, the pine wood-based activated carbon was used to perform the study of LIB anode. The SSA and SPV of pine wood-based activated carbon through self-activation process were as high as 2738 m^2 g^{-1} and 2.209 cm^3 g^{-1}, respectively, which are superior to other activated carbons synthesized by conventional physical/thermal and chemical activation processes. Because of the excellent physico-chemical properties offering a large number of electroactive sites, the outstanding electrochemical performances were achieved, including the cycling stability up to 200 cycles and high C-rate capability (till 3C) with a specific capacity of 646 mAh g^{-1} at 0.1C. These appealing results are much higher than those of commercially available graphite and lab-produced carbon nanotube anode materials. The results showed that the activated carbon from self-activation process, integrated with good LIB performance, might offer a feasible way toward the advanced, large-scale and highly efficient synthesis for activated carbon-based anodes in the LIB production.

In Chapter 5, kenaf core-based activated carbons from self-activation were employed for the studies of the water cleaning and oil absorptions. In general, kenaf core-based activated carbons presented better capacities, compared with the commercial activated carbon. It was found that the micropore of the activated carbon more prefers to absorb small-molecular impurities (e.g. iodine, copper ion), and the meso-macropore is good at absorbing big-molecular impurities (e.g. tannic acid,

rhodamine 6G). Moreover, the oil-absorption capacity was increased by 4.6 times after the kenaf core being converted into activated carbon.

Activated carbon also can be used as electromagnetic interference (EMI) shielding materials. In Chapter 6, the composites of kenaf fibers, powdered activated carbon and polyester were fabricated by vacuum-assisted resin transfer molding (VARTM) technology. The EMI shielding effectiveness of the composites can be 93.0% at the frequency from 8 GHz to 12 GHz, and the EMI absorption can be as high as 64.0%. It was showed that the activated carbon was more effective at EMI signal absorption rather than reflection, which benefited the decrease of secondary electromagnetic pollution.

7.3 Future Work

The main product from self-activation of biomass is activated carbon, which has been investigated in details in this study. The by-product is syngas, which was simply described, but not investigated. The analysis and application of the syngas will be our next focus of the self-activation process. The preliminary results of syngas in Chapter 2 showed that it mainly contained H_2, CO, and CO_2, which were possibly used in methanol production. In addition, more applications of the high-performance activated carbon from self-activation process will be further researched.